Nonlinear Frequency Conversion of Photons for Quantum Networks

Wright, Thomas

Award date:
2020

Awarding institution:
University of Bath

Nonlinear Frequency Conversion of Photons for Quantum Networks

Thomas A. Wright

A thesis submitted for the degree of Doctor of Philosophy

University of Bath
Department of Physics
October 2019

Supervised by
Dr. Peter J. Mosley

Centre for Photonics and Photonic Materials
Department of Physics
University of Bath

In dedication to my parents,
Rosemary and Chris.

Abstract

Quantum networks provide a realistic framework through which large-scale quantum-information processing may be achieved. Underpinning the network approach is the establishment of quantum interconnects between nodes which facilitate the distribution of entanglement. To this end, recent and ongoing advances in the generation and manipulation of quantum states of light are of particular benefit. By employing existing optical-fibre infrastructure, light may be harnessed to transmit high-bandwidth quantum signals over vast distances. This is possible as photons will not ordinarily interact with each other and transmission at telecommunication wavelengths in the infrared minimises loss in fibre. However, many candidate quantum nodes operate at optical frequencies which are inherently lossy in optical fibre. Frequency conversion of single photon states to low-loss telecommunication wavelengths is therefore key to the successful development of information-processing networks with dependable quantum interconnects.

The research described within this thesis concerns the frequency conversion of light between emission wavelengths of Sr^+ ions and the telecommunication C band, addressing frequency conversion requirements of a planned quantum network under development by the UK's Networked Quantum Information Technology Hub. Two conversion schemes are presented, each addressing emission lines located within different spectral regions. The first interface is based on second-order nonlinear processes in a bespoke custom-poled crystal and is used to demonstrate bi-directional single-photon-level conversion between 422 nm and the telecommunication C band. This frequency shift is unusually large and demonstrates a step forward in the capability to establish direct connections between the blue and UV, and telecommunication wavelengths. The second interface is enacted through a resource-efficient FWM scheme which permits the use of a single pulsed laser system. We demonstrate bi-directional frequency conversion between 1092 nm and the C band.

Contents

Acronyms

BBO	Beta-Barium Borate.
BFA	Bare-Fibre Adaptor.
BPF	Band-Pass Filter.
BS	Beam Splitter.
Ca	Calcium.
CCD	Charge-Coupled Device.
CW	Continuous Wave.
DBR	Distributed Bragg Reflector.
DFG	Difference-Frequency Generation.
DM	Dichroic Mirror.
ECDL	External-Cavity Diode Laser.
FC	Frequency Conversion.
HWP	Half-Wave Plate.
InGaAs	Indium Gallium Arsenide.
IR	Infrared.
JSA	Joint Spectral Amplitude.
JSI	Joint Spectral Intensity.
KTP	Potassium titanyl phosphate.

$LiNbO_3$	Lithium Niobate.
$MgO:LiNbO_3$	Magnesium-Doped Lithium Niobate.
MgO:PPLN	Magnesium-Doped Periodically Poled Lithium Niobate.
MMF	Multi-Mode Fibre.
NDF	Neutral-Density Filter.
NIR	Near-Infrared.
NQIT	The Networked Quantum Information Technologies Hub.
OD	Outer Diameter.
OPD	Optical-Path Difference.
OPL	Optical-Path Length.
OR	Optical Rectification.
OSA	Optical-Spectrum Analyser.
PBS	Polarising Beam Splitter.
PEF	Pump-Envelope Function.
PLL	Pase-Locked Loop.
PM	Polarisation Maintaining.
PMC	Phase-Matching Contour.
PMF	Phase-Matching Function.
QFC	Quantum Frequency Conversion.
QPM	Quasi-Phase-Matching.
SC	Supercontinuum.
SD	Standard Deviation.
SFG	Sum-Frequency Generation.
SHG	Second-Harmonic Generation.
Si	Silicon.
SM400	Single-Mode Fibre at 400 nm.

SMF	Single-Mode Fibre.
SMF-28	Single-Mode Fibre at 1550 nm.
SNR	Signal-to-Noise.
SPAD	Single-Photon Avalanche Diode.
SPDC	Spontaneous Parametric Down Conversion.
SPF	Short-Pass Filter.
Sr	Strontium.
TEC	Thermoelectric cooler.
TTM	Time-Tagging Module.
TWM	Three-Wave Mixing.
UV	Ultraviolet.

Chapter 1

Introduction

1.1 Overview

In this thesis I consider the development of technologies often described as being part of a *second quantum revolution*. The work presented herein is but a single contribution to an ever increasing volume of scientific research and technological innovation concerned with the observation, simulation and control of non-classical phenomena.

1.1.1 Viva la quantum revolution

It is useful here to provide some context. The continued evolution of quantum theory which occurred throughout the 20^{th} century heralded the arrival of many inventions exploiting newly understood phenomena: transistors, semi-conductor devices and lasers to name but a few. These devices all belong to the *first quantum revolution* and exploit mechanisms revealed to us through the study of naturally occurring phenomena. Many of these first-wave inventions unlocked new areas of scientific discovery and even form the basis of many technologies on which modern society has become perilously reliant. In the last two decades however, a number of new areas of research have emerged, focussed on developing

quantum-enhanced technologies. The *second quantum revolution* is now. Systems have been specifically engineered to exhibit quantum properties not observed in nature such as quantum coherence and entanglement, leading to many new applications in metrology, sensing, imaging, cryptography and computing. It is hoped the scientific and societal impacts of the *second quantum revolution* will be similarly profound to those of the first.

1.1.2 The importance of photons

Observations of light have ever proved instrumental in the probing of physical phenomena. Whilst investigating the photoelectric effect in 1905, Albert Einstein developed the theory that atoms absorb energy from a light beam in discrete packets [1]. The energy packets identified by Einstein were the so-called *quanta* described by Max Planck's theory of black-body radiation set out four years prior [2]. The experimental and theoretical appraisals of the role played by light in quantised systems proved crucial in the development of early quantum theory, but provided no direct evidence of the quantum nature of light itself - only that *something* was quantised. The field of quantum optics only became truly realised with Paul Dirac's formalism of the quantum theory of radiation and the quantisation of light during the 1920s [3]. The term 'photon', used to describe the smallest unit of radiant energy, was later coined by a physical chemist named Gilbert Lewis in 1926.

We have already intimated the importance of light as a tool for exploring the quantised nature of atoms, molecules and ions, but the use of photons as a solitary platform for both *Gedankenexperimente* and laboratory experiments is deserving of further discussion. In 1963, Roy Glauber laid out a coherent description how quantum states of light innately exhibit different statistical properties [4]. The ideas he set out provided the necessary indications as to how quantised light might be explored; the decades to follow proved fruitful in achieving this end.

> *"That a photon is not split in two by a beam splitter is certainly "old hat," and it may seem surprising that we have gone to the effort to test this prediction experimentally."* – John F. Clauser, 1974 [5].

John F. Clauser was the first to demonstrate a source of single-photon emission [5]; his experiment validated the longstanding theoretical conjecture that single photons incident on a half-silvered mirror would never yield simultaneous detection signals between detectors placed in the transmitted and reflected beams. Clauser's experiment used single photons emitted from a cascade transition in calcium atoms, although subsequently this photon-antibunching effect was also observed, using fluorescence from a sodium atomic beam, by Kimble et al. [6] and Walls [7]. The arrival of the laser in 1960 [8] had stimulated the growing interest in experimental quantum optics. Endowed with coherent, high-power light beams, physicists developed a range of techniques to generate nonclassical states of light with emission rates far exceeding those previously available. Sources which exploited spontaneous nonlinear-optical processes facilitated the generation of correlated photon pairs [9], from which heralded one-photon states could be realised [10]. Experiments exploiting such innovative methods helped to explore concepts conceived while quantum mechanics was in its infancy — most famous amongst these was perhaps the refutation of local hidden variable theories as expressed in the Einstein-Podolsky-Rosen paradox [11] through the violation of the Bell inequalities with entangled pairs of photons [12–14].

1.1.3 The properties of photons

In the previous subsection we have reviewed the significance of some experiments using photons as a mechanism for probing the laws of quantum mechanics. The number of developing quantum technologies, as alluded to in Section 1.1.1, which are reliant on these laws continues to expand. We have not yet, however, defined either what a photon actually is, nor any of the properties which it exhibits.

Simply put, a photon is a single quantised excitation of the electromagnetic field. The properties possessed by a photon include: energy, polarisation, spatial and temporal modes, and spectral distribution.

A commonplace formalism used to describe the quantised electromagnetic field begins with the consideration of a cavity [15,16]. The cavity length will determine a number of longitudinal modes where solutions take the form equivalent to the quantum harmonic oscillator, with the energy, E_n, quantised in in units of $\hbar\omega$:

$$E_n = \left(n + \frac{1}{2}\right)\hbar\omega. \tag{1.1}$$

The principal excitation is given by the number of photons, n, although the ground-state energy, $\frac{1}{2}\hbar\omega$, means that no mode is ever truly empty. Physically, this zero-point energy is associated with fluctuations in the vacuum field. We will see later that these vacuum fluctuations are essential in allowing for spontaneous optical processes to occur.

We may define two operators, $\hat{a}_i^\dagger$ and $\hat{a}_i$, that raise and lower the number of field excitations, i.e. photons, in a mode. These operators are referred to as the creation and annihilation operators, and act accordingly on a mode i:

$$\hat{a}_i^\dagger|0\rangle = |1\rangle \tag{1.2}$$

$$\hat{a}_i|1\rangle = |0\rangle. \tag{1.3}$$

The terms $|0\rangle$ and $|1\rangle$ are state vectors describing a mode containing zero and one photons, and it should be apparent from Eq.1.1 that these states would have energies $\frac{1}{2}\hbar\omega$ and $\frac{3}{2}\hbar\omega$, respectively. We have already stated that a fully representative description of a photon will include properties such as optical frequency and the creation and annihilation operators can

indeed be adjusted to represent the spectral mode which the photon occupies:

$$\hat{a}_i^\dagger(\omega_i)|0\rangle = |1_{\omega_i}\rangle. \tag{1.4}$$

Equation 1.4 describes a photon with a single well-defined optical frequency, ω_i, and assumes that the photon exists only in a single frequency mode. This description is clearly unsatisfactory if we wish to begin considering photons outside the cavity we've built. Furthermore, a single-frequency photon would have zero bandwidth and hence infinite duration, making it by definition no longer a wave-packet. We incorparate a description of the frequency structure of the photon by making a wighted sum over all spectral modes of the quantised field, with the weighting given by the particular frequency distribution of the photon, $f(\omega_i)$:

$$|\Psi_i(\omega_i)\rangle = \int d\omega_i f(\omega_i)\hat{a}_i^\dagger(\omega_i)|0\rangle. \tag{1.5}$$

The resulting wave function, $\Psi_i(\omega_i)$, describes the photon in the most complete mathematical way if we are to consider only the frequency degree of freedom. Further degrees of freedom such as polarisation, momentum and spatial distribution might also be described, although when such properties are composed of sets of orthogonal modes then a description based on a superposition of states is necessitated. Photons which are identical in all degrees of freedom are completely indistinguishable.

Photons are bosonic, with one additional characteristic worth discussing here. The interference of two photons at a beam splitter (BS) is a non-classical effect which is useful in determining the indistinguishability of photons, but also in optical quantum computing. We start by thinking about an ideal lossless beam splitter, with reflection coefficient R^2 and transmission coefficient T^2. For convenience we shall refer to the the two input ports as i_1 and i_2, and the two output ports as o_1 and o_2. Our beam splitter is lossless and so we may write down the following two expressions relating creation operators for both the input and

output modes:

$$R\hat{o}_1^\dagger + T\hat{o}_2^\dagger = \hat{i}_1^\dagger, \tag{1.6}$$

$$T\hat{o}_1^\dagger - R\hat{o}_2^\dagger = \hat{i}_2^\dagger, \tag{1.7}$$

where the negative term in Eq.1.7 arises due to the π phase shift accrued by reflection and the need for conservation of energy ($R^2 + T^2 = 1$). Were we to send a single photon in to input i_1 of our beamsplitter we would obtain

$$|\Psi\rangle = \hat{i}_1^\dagger|0\rangle = \left(R\hat{o}_1^\dagger + T\hat{o}_2^\dagger\right)|0\rangle. \tag{1.8}$$

However, if we at the same time introduce a second photon in to input i_2 at the same instance we will obtain the following:

$$|\Psi\rangle = \hat{i}_1^\dagger\hat{i}_2^\dagger|0\rangle = \left(R\hat{o}_1^\dagger + T\hat{o}_2^\dagger\right)\left(T\hat{o}_1^\dagger - R\hat{o}_2^\dagger\right)|0\rangle, \tag{1.9}$$

$$|\Psi\rangle = \left(TR\hat{o}_1^\dagger\hat{o}_1^\dagger - R^2\hat{o}_1^\dagger\hat{o}_2^\dagger + T^2\hat{o}_1^\dagger\hat{o}_2^\dagger - RT\hat{o}_2^\dagger\hat{o}_2^\dagger\right)|0\rangle. \tag{1.10}$$

Here we see that there are four potential outcomes when two photons are incident on separate input ports of a beam splitter, which are visualised in Fig. 1.1.

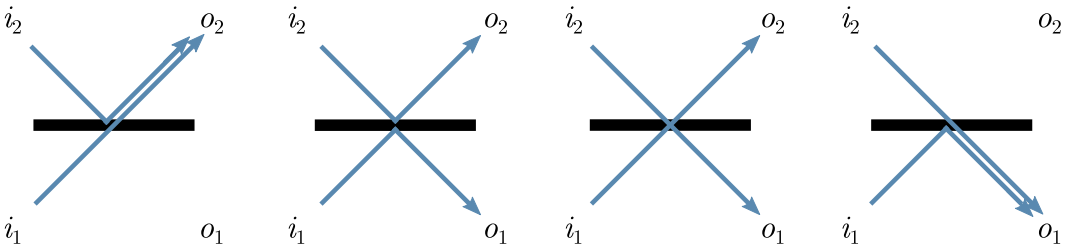

Figure 1.1 The four potential outcomes of one photon impinging on each input port of a beam splitter. If the photons do not interfere then all cases are of equal probability. However, if input photons are indistinguishable then the amplitudes which correspond to the middle two cases deconstructively interfere and both photons will exit the beam splitter together.

Assuming our beam splitter is perfectly balanced, i.e. $R = T = \frac{1}{\sqrt{2}}$, the cross terms will cancel and the output state becomes:

$$|\Psi\rangle = \frac{1}{\sqrt{2}}\Big(\hat{o}_1^\dagger \hat{o}_1^\dagger - \hat{o}_2^\dagger \hat{o}_2^\dagger\Big)|0\rangle = \frac{1}{\sqrt{2}}\Big(|2\rangle_{o_1}|0\rangle_{o_2} - |0\rangle_{o_1}|2\rangle_{o_2}\Big). \tag{1.11}$$

What remains is a linear superposition of the two cases in which both photons exit from the same output port. This so-called 'bunching' behaviour is widely known as the Hong-Ou-Mandel interference and occurs perfectly only if the two input photons are in pure states (as oppose to an incoherent mixture of different modes) and that these pure states are indistinguishable[17].

The Hong-Ou-Mandel effect provides a means by which two photons may be readily entangled, i.e. initiating a phenomenon in which the quantum state of each photon cannot be described independently of the state of the other. Accordingly, Hong-Ou-Mandel interference is fundamental to the operation of many optical quantum logic gates. To demonstrate, let us suppose the two photons impinging on our beam splitter originate from two distinct emitters, that are indistinguishable, but which emit photons existing in a balanced superposition of two orthogonal linearly-polarised states, $|\mathrm{H}\rangle$ and $|\mathrm{V}\rangle$:

$$|\Psi_{i_1}\rangle = \hat{i}_1^\dagger|0\rangle = \frac{1}{\sqrt{2}}\Big(\hat{i}_{1,\mathrm{H}}^\dagger + \hat{i}_{1,\mathrm{V}}^\dagger\Big)|0\rangle, \tag{1.12}$$

$$|\Psi_{i_2}\rangle = \hat{i}_2^\dagger|0\rangle = \frac{1}{\sqrt{2}}\Big(\hat{i}_{2,\mathrm{H}}^\dagger + \hat{i}_{2,\mathrm{V}}^\dagger\Big)|0\rangle. \tag{1.13}$$

Figure 1.2 shows a schematic which illustrates this scenario, depicting two ion trap emitters with their photon emissions routed towards a beam splitter and two single-photon detectors. We know from the outcome of Eq. 1.11 that if the two input photons, one from each ion trap, both occupy the same polarisation mode then we will not observe coincident counts from the pair of detectors placed at the output ports of the beamsplitter. In the real world, where we would expect some loss in our experiment, we would be left to assume either that the

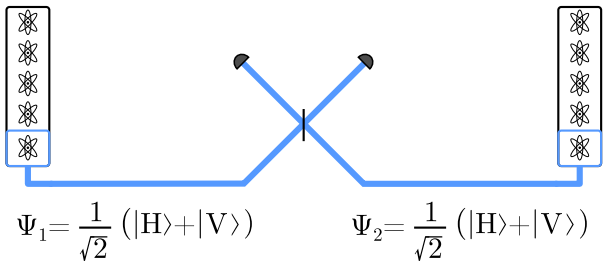

Figure 1.2 Two ion trap emitters, that generate indistinguishable photons in a superposition of orthogonal polarisation modes, with their emissions routed towards the input ports of a beam splitter. If the output ports of the beam splitter are monitored with single-photon detectors, entanglement of the the two ion traps may be observed by establishing two-photon interference at the beam splitter and looking for coincident counts from the two detectors.

two photons were in a superposition of the states $|H_1, H_2\rangle$ and $|V_1, V_2\rangle$, or that one of our photons was lost. However, were we to record coincidental clicks on both of the detectors we would have achieved entanglement by post-selecting on a superposition of $|H_1, V_2\rangle$ and $|V_1, H_2\rangle$. In this manner, entanglement distribution may be achieved between remote nodes that each emit photons in a superposition of two states, simply by impinging these photons on beam splitters and observing the outcome.

The significance of the indistinguishability requirement in the Hong-Ou-Mandel effect cannot be understated when considering both the motivation for, and challenges incurred when implementing quantum frequency conversion.

1.1.4 Quantum supremacy

The classical computers underpinning modern society operate using data encoded on binary states of a transistor, their computational power scaling linearly with the available number of bits. In contrast, computers that exploit the control of superpositions of quantum states to form quantum bits (qubits), will grow exponentially in power with the addition of extra qubits. This scaling advantage will allow quantum computers to address a class of problems previously considered unfeasible. However, the development of a universal quan-

tum computer is a monstrously ambitious scientific and engineering challenge. Far closer to realisation are specialised quantum systems performing specific tasks [18]. Such quantum simulators are designed to be representative of particular physical systems, and may be applied to transform our capabilities, for example, in the design of new materials and pharmaceuticals or in enhancing logistics and specific industrial processes [19–22].

In the linear-optical paradigm of quantum information processing, data may be encoded on the polarisation state of the photon, or indeed any other degree of freedom such as photon number or arrival time. Operations on these photonic qubits are achieved using logic gates reliant on the the Bose-Einstein coalescence of single photons incident on a beamsplitter — the so-called Hong-Ou-Mandel interference discussed in section 1.1.3. Even where implementations of quantum computing do not make use of photons for information processing, the photonic qubit is regarded as unparalleled in its ability to transfer information over long distances [15].

1.2 Quantum networks

1.2.1 How to build a quantum machine

A network is a set of nodes, which may contain some processing capability, interconnected by channels through which information or energy flows. Examples which fit this description include power grids, financial markets and the human nervous system — all indicating a crucial role that networks play in society, technology or nature. Networks are important also within the context of quantum information science, both for the formal analysis and the physical implementation of quantum computing, communication and metrology.

In particular, network architectures have a number of features that benefit the handling of quantum information: quantum computers are technologically challenging to develop, and therefore it is evidently preferential to construct multiple simple processors, physical

systems encoding just a few qubits, than to exhaust manufacturing efforts producing a single more complex system. A networked scheme further allows for improved computational performance to be obtained via scaling up the number of nodes without implementing a radical change in architecture. Finally, networks are intrinsically robust to imperfections as poorly operating elements can be circumvented or replaced and the network itself may be dynamically reconfigured. The manufacturability, scalability and robustness of network architectures provide an ideal platform on which to develop universal quantum communications, simulators and computers.

1.2.2 The importance of interconnects: quantum channels

A network comprised of quantum processing nodes will have an enhanced performance when using quantum connections, instead of classical connections, between those nodes. A network of k quantum nodes, each with n qubits, and linked by classical channels has a state space of dimension $k2^n$, whereas a fully quantum network has an exponentially larger state space of 2^{kn} [23]. With this being the case, it is worth expending considerable effort in the development of efficient quantum information interconnects between nodes of a quantum network in order to efficiently maximise the dimensions of the state space that may be exploited.

1.2.3 Hybrid light-matter networks

A large-scale quantum network will require not only that quantum information may be manipulated reliably, but also that it be communicated successfully between remote nodes. Amongst existing quantum information processing frameworks, such as ion trapping and linear optical quantum computing, no individual platform is able to fulfil both of these requirements. Photons are regarded as highly suitable for the distribution quantum information either through fibre networks [24] or via satellite [25] but are unsuited for complex manipulation whilst multi-photon gates remain challenging. Conversely, trapped ion processors have

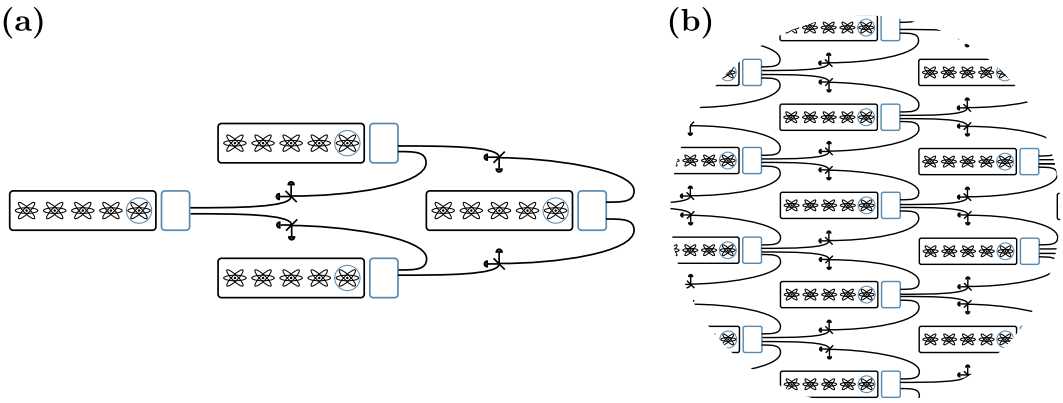

Figure 1.3 Notional quantum networks composed of trapped-ion nodes for processing and storing quantum states, and photonic quantum interconnects for distributing quantum information. (a) A small-scale network with a state space of dimension 2^{10}, which is usable for communication and simulation. (b) A larger-scale network will be applicable to machine learning and solving optimisation problems.

been shown to achieve high-fidelity two-qubit operations [26] but are intrinsically unsuitable for sharing entanglement beyond the bounds of a single laboratory. The desirable qualities of each of these architectures may be harnessed to form a capable hybrid light-matter network, by making use of single photon qubits to achieve entanglement distribution between a large number of remote trapped ion processor nodes [27,28]. Two notional schematics for such a hybrid network architecture are shown in Fig. 1.3. The first schematised network, presented in Fig. 1.3(a), consists of four ion traps each containing five ions in a linear arrangement. These ion-trap nodes are interfaced by optical interconnects which allow entanglement to be distributed between the traps. The second network, shown in Fig. 1.3(b), expands on this same architecture to include any arbitrary number of traps.

1.3 Quantum frequency conversion

The optical-communication bus running between nodes of a hybrid quantum network will be innately complex as it must serve to overcome two technical challenges: ensuring compatibility when establishing entanglement between devices operating at different optical frequencies

and the low loss transmission of single photons across large distances. Quantum frequency conversion (QFC) is a process whereby photons may be coherently shifted to a different optical frequency, and can be used to address both of these challenges. In principle QFC may be engineered to link any wavelength, even as short as the ultraviolet (UV) where many convenient ion transitions are located, to any other, including the infrared (IR) telecommunication bands which enable long-distance low-loss transmission in optical fibre [29] (see Fig. 1.4). The technical flexibility permitted by QFC on the design of a hybrid quantum network marks it as a keystone technology. We, alongside many researchers, are therefore impelled to study QFC techniques and mature the technology surrounding it.

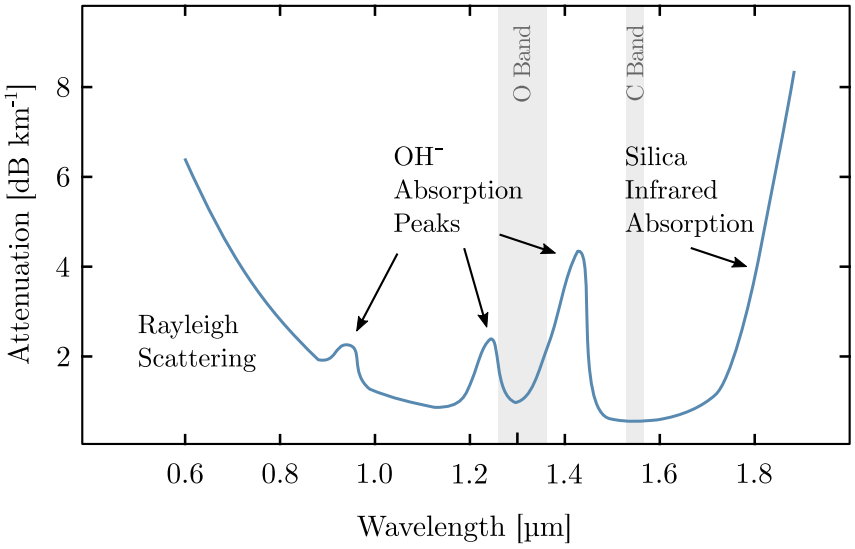

Figure 1.4 Example loss spectrum of a silica fibre designed for single-mode transmission at 1550 nm. Low-loss transmission telecommunication bands are a primary target for many QFC experiments. Details regarding loss mechanisms in optical fibres are presented in Ref. [30] and Ref. [31].

Prem Kumar initially proposed QFC as a process to obtain frequency-tuneable squeezed light for applications in spectroscopy [29]. Following the publication of this monograph, a demonstration was given showing that two daughter fields of a degenerate parametric down conversion process maintain nonclassical intensity correlations even after one of the fields was frequency doubled [32]. Initial experiments which followed focused on enhancing the

detection of IR photons in experiments by mapping them to the visible and near-infrared (NIR), where efficient silicon (Si) photon detectors existed [33,34]. A quantum-information interface was then realised in 2005, enabling the quantum state transfer of a photon at 1310 nm to a 712-nm photon. The 712-nm photon was then shown to exhibit strong two-photon interference with a separate 1555-nm photon, which had originally been entangled with the photon at 1310 nm [35]. Such experiments showed that QFC enables the transfer of entanglement from one photon of a given frequency to another, but did not provably confirm the single-photon nature of the fields involved. In 2010 an experimental verification was given of this capability, whereby a photon emitted from a quantum dot at 1310 nm was up-converted to 710 nm and a second-order intensity correlation measurement showed that the field was indeed composed of single photons [36]. The reverse process, i.e. down-conversion of photons from 710 nm to 1310 nm, was also shown the same year [37].

Frequency conversion, by either three- or four-wave mixing, has been realised in numerous platforms: nonlinear crystals [33,38], planar waveguides [35,39], microresonators [40,41], optical fibers [42,43], and atomic systems [44,45]. As we have seen already, QFC is provably capable of translating quantum states of light, with there now being many examples in the literature to reaffirm this; from frequency remapping of squeezed light [46,47], as initially proposed, to demonstrations using entangled states [35,36,48].

In sections 1.2.2 and 1.2.3 an argument is built for the potential enhancement offered by single-photon interconnects within a quantum network. However, we have also outlined how optical quantum-logic gates are dependant on the indistinguishability of the input states and that many quantum nodes operate at frequencies that are inherently lossy in optical fibre. As a consequence, numerous frequency-converison experiments have been conducted which translate node-compatible photons both from [35,36,46,49–54] and to [37,48,55–59,59–63] telecommunication wavelengths. As particular techniques have matured direct connections between dissimilar short-wavelength (606 and 780 nm) nodes have also been established by means of

conversion to, and then back from, the C band [64].

Significant effort has been made in existing frequency-conversion experiments to maximise conversion efficiency and overcome limitations arising from photon bandwidth, pump-induced noise and difficulties in implementing adequate phase-matching control. Near-unit translation efficiency has been demonstrated in fibre [43], although this is far from commonplace in the literature, with the stated example was only being achieved across a spectral shift of 12 nm within the telecommunication C band.

Implementing QFC using three-wave mixing necessitates that the optical-nonlinearity-induced coupling be derived from a single strong pump field, which additionally must account for the energy (frequency) difference between the input and target wavelength. For this reason the use of three-wave mixing (TWM) is not appropriate for very small frequency shifts as this would require a pump laser operating in the infrared and suitable transmission for all the spectral fields in the nonlinear medium. Similarly, medium to large frequency shifts will only be permitted where suitable laser systems allow, and in mediums in which these processes may be phase matched. The large frequency separations between many ion transitions in the blue and ultraviolet, and the telecommunication bands in the near infrared (NIR) pose a particular difficulty in the development of quantum networks, leading to the proposition of a multiple-step approach [65] or the capitulation of network designs to use state transitions at more favourable wavelengths [61,62]. Even the classical generation of light at UV wavelengths by means of parametric TWM is challenging, although has nonetheless been achieved using both sum-frequency generation (SFG) [66] and second-harmonic generation (SHG) [67]. Accordingly, demonstrations of QFC involving blue and UV wavelengths are uncommon, although recently the unidirectional translation of quantum states between the UV and telecommunication O band has been demonstrated [68,69]. Furthermore, the majority of QFC experiments in the literature are unidirectional in operation with limited exception [70], whereas creating a functional fibre-connected quantum network will make the critical trans-

lation of states to the telecommunication wavelengths highly desirable to implement using two-way converters.

1.4 The UK's Networked Quantum Information Technologies Hub

Realising a quantum network is a daunting challenge to undertake. Intrinsic to the nature of the task is the requirement to integrate a range of disparate and cutting-edge technologies. The Networked Quantum Information Technologies Hub (NQIT)[1], established in 2014, was formed under the UK National Quantum Technologies Programme to meet this challenge. The hub, consisting of nine academic institutions and over thirty industrial partners, was established with the goal of developing the first truly scalable universal quantum computing machine.

The proposed system, designated the Q20:20 quantum engine, will be an optically-linked network of 20 quantum processors, each consisting of up to 20 matter qubits. Each processor node will take the form of an ion trap containing two species of ions positioned in a linear arrangement, with the qubits implemented within the hyperfine states of each ion. In the proposed design the two ion species are collectively sufficient for all entanglement generation, processing, storage and cooling operations. These trapped-ion qubits will be addressed optically and the traps interconnected by single-photon emissions which are combined and made measurable by an optical network of fibres, beam splitters, detectors and switches.

Specifically, the quantum information will be processed and stored on calcium ($^{43}Ca^{+}$) *memory* ions, with singly-ionised strontium ($^{88}Sr^{+}$) ions used as the *interface* qubits from which the ion-photon entanglement will be established [28]. This two-species arrangement is schematised in Fig. 1.5(b). The $^{88}Sr^{+}$ interface ions have an alkali-like electronic structure,

[1] https://nqit.ox.ac.uk

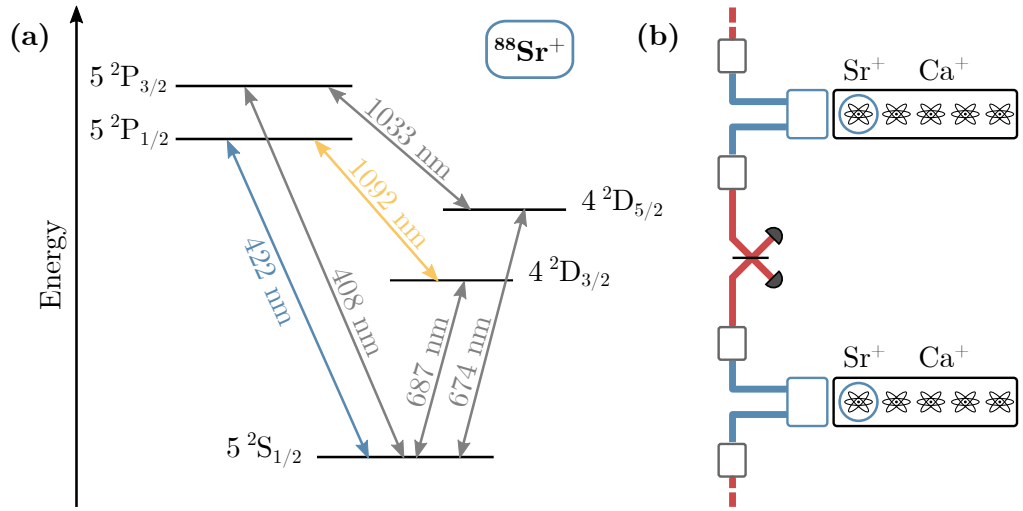

Figure 1.5 (a) The lowest lying energy levels of an $^{88}Sr^+$ ion, with the emission wavelengths denoted for the associated transitions. (b) The layout of the proposed ion trap quantum network nodes. Each processor node contains two species of ion confined in separate potential wells. The Sr^+ ion is used to generate ion-photon entanglement. The Ca^+ ions are used for storing and processing quantum information.

each possessing a single valence electron; the optical transition which is incipiently addressable in this regime is the $S_{1/2} \rightarrow P_{1/2}$ line of the Sr^+ ions at 422 nm (see Fig.1.5(a)). In addition to being spectrally remote from other potential nodes of the network, this wavelength falls outside the range from which previous QFC experiments have been able to successfully establish a direct link to the telecommunications C band. It is nevertheless the most straitforward emission line to exploit and a realistic selection for use in early network demonstrators. However, once an Sr^+ ion is in the excited $P_{1/2}$ state, it will not necessarily decay back to the ground state, but instead decay to the metastable $D_{3/2}$ state, which it does with a branching ratio of 1:13. Under a different mode of operation, this alternative transition may be resonantly enhanced by introducing an optical cavity about the Sr^+ ion to facilitate a regime whereby photons emitted from the ion trap have a wavelength of 1092 nm instead of 422 nm. Such a regime has the potential to alleviate some of the complexities in engineering the optical interconnects of a future quantum network.

In the time since the consortium was established, much progress has been made in developing the constituent technologies. Electronics, control software and verification systems have been developed, with work also implemented in the use of alternative qubits such as colour-centre defects in diamond [71] and superconducting qubits [72]. In relation to the Q20:20 demonstrator's hardware, recent progress includes the advancement of the control systems for the ion-trap processors [73], and the demonstration of direct free-space interconnects between two processors [74]. Furthermore, single photons from a $^{40}Ca^{+}$ ion have been coupled to an optical cavity and transmitted through 10 km of optical fibre by means of frequency conversion from 866 nm to 1530 nm [62]. This particular work provides the first demonstration of the relevant hardware necessary to optically interface the Q20:20 ion-trap qubits, although does so using a different ion species and optical frequencies to that of the planned network. The photonic-network-engineering work package has also developed modular optical circuits [75], integrated optical waveguide couplers [76] and provided a demonstration of frequency conversion between the Sr^{+} transition at 422 nm and the telecommunication C band [77], with the latter elaborated on within the body of this thesis.

Le roi est mort, vive le roi! The Networked Quantum Information Technologies Hub ran from 2014 to 2019 and has since been succeeded by the Quantum Computing and Simulation Hub. The new *'phase two'* hub, aims to build on the successes of the *'phase one'* NQIT programme, retaining many of the original long-term objectives set out in 2014.

1.5 Thesis outline

This thesis is presented in five principle chapters. Following the introduction given here, in Chapter 2, a two-way photonic interface for linking the Sr^{+} transition at 422 nm to the telecommunication C band is presented. The interface is based on second-order nonlinear optical effects and so the relevant theory is also covered to facilitate discussion. In Chapter 3 third-order nonlinear processes are examined; frequency conversion via four-wave mix-

ing is investigated using numerical simulations and a resource-efficient frequency conversion scheme between the Sr^+ transition at 1092 nm and the telecommunication C band is presented. Chapter 4 details the experimental realisation of the four-wave-mixing conversion. Finally, in Chapter 5, the conclusions of this thesis are laid out and an outlook on future work is given.

1.6 Personal contribution statement

The introduction to this thesis has already outlined the context of the presented work within a large collaborative project. Chapter 2, in particular, contains work in which a number of researchers were connected and so a breakdown of the contributions of those most heavily involved is necessary.

For the work outlined in Chapter 2, I was responsible for designing and building the experiment. Corin B.E. Gawith fabricated the periodically-poled crystals. In the collection of data, I was assisted by Robert J.A. Francis-Jones and Benjamin Brecht. I then completed the analysis of the data. Peter J. Mosley and Benjamin Brecht supervised the project.

Chapter 3 presents a frequency-conversion scheme and numerical simulations which I developed under the supervision of Peter J. Mosley.

Chapter 4 discusses the experimentally-realised frequency-conversion scheme. I fabricated the optical fibres with some assistance from Robert J.A. Francis-Jones, Oliver R. Gibson and Charlotte Parry. I designed and built the experiment, and collected and analysed the data. Peter J. Mosley provided supervision and guidance.

Chapter 2

Second-Order Nonlinear Frequency Conversion

The frequency conversion of photons is achieved by exploiting nonlinear optical phenomena. A short discussion of the relevant theory is made in Section 2.1 to facilitate the required understanding used to engineer the efficient translation of single photon states. In Section 2.2 a photonic interface for linking the Sr^+ transition at 422 nm to the telecommunication C band is presented.

2.1 Light matter interaction

Consider a dielectric under the application of an electric field: bound electrons are shifted from their equilibrium positions forming electric dipoles aligned with the field, polarising the material. For low light intensities the polarisation $\mathbf{P}(\bar{r}, t)$ of a dielectric material, is assumed to depend linearly on the strength of an applied optical field $\mathbf{E}(\bar{r}, t)$:

$$\mathbf{P} = \epsilon_0 \chi \mathbf{E}, \tag{2.1}$$

where χ is the susceptibility of the dielectric and ϵ_0 is the permittivity of free space. A low intensity light wave propagating through a dielectric medium will induce harmonically oscillating dipole moments which, in turn will radiate their own field at the same frequency with a phase delay. All such contributions from the material interfere with the original light wave resulting in a wave with the same frequency but a shorter wavelength, slowing the phase velocity. Herein we have recovered dispersion which, along with absorption, forms the linear material response.

For intense electromagnetic fields, widely achievable using high power lasers, a linear approximation of the polarisation response is no longer valid. In generalising Eq.2.1 the polarisation can be better described by a Taylor expansion [78],

$$\mathbf{P} = \epsilon_0(\underbrace{\chi^{(1)} \cdot \mathbf{E}}_{\text{linear}} + \underbrace{\chi^{(2)} : \mathbf{EE} + \chi^{(3)} \vdots \mathbf{EEE} + ...}_{\text{nonlinear}}), \tag{2.2}$$

where $\chi^{(1)}$ is the linear susceptibility, $\chi^{(2)}$ is the second-order susceptibility and $\chi^{(3)}$ is the third-order susceptibility. Separating the polarisation into the linear first-order response $\mathbf{P^{(1)}}$, and a series of nonlinear higher-order contributions we may rewrite Eq.2.2 as:

$$\mathbf{P^{(1)}} = \epsilon_0 \chi^{(1)} \cdot \mathbf{E} \tag{2.3}$$

$$\mathbf{P^{(2)}} = \epsilon_0 \chi^{(2)} : \mathbf{EE} \tag{2.4}$$

$$\mathbf{P^{(3)}} = \epsilon_0 \chi^{(3)} \vdots \mathbf{EEE} \tag{2.5}$$

$$\vdots \quad .$$

The well defined crystalline axes of many optical materials make it essential to consider how the response of a medium may depend on the directions in which a field is applied. The prevalent term responsible for the nonlinear effects discussed within this chapter is $\chi^{(2)}$ as we consider the use of media with noncentrosymmetric crystal structures. In generalising

Eq.2.4 to express the anisotropic response of a $\chi^{(2)}$ medium we express the components of $\mathbf{P^{(2)}}$ as:

$$P_i^{(2)} = \epsilon_0 \sum_{j,k} \chi_{ijk}^{(2)} E_j E_k. \tag{2.6}$$

The second-order susceptibility $\chi_{ijk}^{(2)}$ we see here is a rank 3 tensor, where the subscripts i, j and k correspond to the field components that may be in any cartesian axes x, y and z. Although Eq.2.6 implies there are nine different contributions for each orthogonal component of $\mathbf{P^{(2)}}$, high degrees of symmetry in most structures ensure that many of these terms are zero. Furthermore, in this thesis we will consider only cases in which all of the optical fields are co-polarised. It is therefore convenient to regard all components of the second-order susceptibility other than $\chi_{xxx}^{(2)}$, $\chi_{yyy}^{(2)}$ and $\chi_{zzz}^{(2)}$ as zero.

It is important to note that the second-order polarisation of a dielectric, $\mathbf{P^{(2)}}$, leads to the radiation of new fields in response to the presence of two original fields. The induced coupling between three-electric fields leads to the designation of $\chi^{(2)}$ processes as three-wave mixing.

2.1.1 Three-wave mixing

We consider now the second-order nonlinear polarisation response of a $\chi^{(2)}$ crystal to monochromatic high-intensity optical plane waves of the form

$$\mathbf{E}(t,z) = \frac{1}{2}\hat{x}\big\{E_0 \exp i\big[\omega_0 t - k(\omega_0)z\big]\big\} + c.c., \tag{2.7}$$

where $k(\omega_0)$ is the frequency-dependant propagation constant, E_0 is the slowly varying field amplitude and $\hat{x}$ is the polarisation unit vector. When we use Eq.2.4 to calculate the polarisation response along $\hat{x}$ to the field described by Eq.2.7 we obtain

$$\mathbf{P}^{(2)}(t,z) = \frac{1}{4}\hat{x}\Big(\epsilon_0 \chi_{xxx}^{(2)}\big\{E_0^2 \exp i\big[2\omega_0 t - 2k(\omega_0)z\big] + c.c.\big\} + \epsilon_0 \chi^{(2)}|E_0|^2\Big). \tag{2.8}$$

Herein we have recovered a term oscillating at twice the original frequency, referred to as the second harmonic. Equation 2.8 tells us that radiation will be emitted by second harmonic generation with a space dependant phase of $2k(\omega_j)z$. The emitted light will then accrue a phase of $k(2\omega_j)z$ during its continued propagation. All similarly generated fields at further points along the path of the original wave will typically deconstructively interfere unless the phases of the generated and propagating radiation are matched in the medium such that $2k(\omega_j)z = k(2\omega_j)z$. This is a particular phase-matching criteria for SHG, although we will need to consider a whole range of phase-matching relations for different processes discussed in this thesis. The constant term in Eq.2.8 describes optical rectification (OR) whereupon a static electric field is created across the the nonlinear crystal.

In order to build up a more general case we will now explore the second-order polarisation response in the presence of two fields with non-degenerate frequencies ω_1 and ω_2, and amplitudes E_1 and E_2:

$$\mathbf{E}(t,z) = \frac{1}{2}\hat{x}\big\{E_1 \exp i\big[\omega_1 t - k(\omega_1)z\big] + E_2 \exp i\big[\omega_2 t - k(\omega_2)z\big]\big\} + c.c., \tag{2.9}$$

Substituting the field described by Eq.2.9 into Eq.2.6 yields the polarisation response

$$\begin{aligned}\mathbf{P}^{(2)}(t,z) = \frac{1}{4}\hat{x}\,\epsilon_0\chi^{(2)}_{xxx}\Big[&\underbrace{\big(E_1^2 \exp i\{2\omega_1 t - 2k(\omega_1)z\} + c.c.\big)}_{\text{SHG}} \\ &+ \underbrace{\big(E_2^2 \exp i\{2\omega_2 t - 2k(\omega_2)z\} + c.c.\big)}_{\text{SHG}} \\ &+ \underbrace{2\big(E_1 E_2 \exp i\{[\omega_1+\omega_2]t - [k(\omega_1)+k(\omega_2)]z\} + c.c.\big)}_{\text{SFG}} \\ &+ \underbrace{2\big(E_1 E_2^* \exp i\{[\omega_1-\omega_2]t - [k(\omega_1)-k(\omega_2)]z\} + c.c.\big)}_{\text{DFG}} \\ &+ \underbrace{2\big(E_1 E_1^* + E_2 E_2^*\big)}_{\text{OR}}\Big].\end{aligned} \tag{2.10}$$

We have once again obtained the second harmonic of both E_1 and E_2 as well as the optical

rectification term. Additionally however, we have two further contributions oscillating at both $\omega_1 + \omega_2$ and $\omega_1 - \omega_2$ which are referred to as sum- and difference-frequency generation (SFG/DFG). For these processes a coherent buildup of generated light at a frequency $\omega_3 = \omega_1 \pm \omega_2$ occurs when the phase-matching condition $\Delta k_{\mathrm{SFG/DFG}} = k(\omega_1) \pm k(\omega_2) - k(\omega_3) = 0$, is satisfied.

If we continue to scrutinise the SFG and DFG terms in Eq.2.10, it is worth noting that we have only examined the situation when field one has the frequency ω_1 and field two has ω_2. As the opposite might also be true, a degeneracy factor of 2 is also included as requisite.

2.1.2 Engineering the efficiency of $\chi^{(2)}$ processes

As previously mentioned, daughter fields of frequency ω_3 generated either in SFG or DFG require that the phase-matching condition, $\Delta k = 0$, is satisfied in order that they constructively interfere and produce a non-zero output. Material selection alone would severely constrain the potential to engineer any frequency mixing schemes. However, there exists a commonly used approach to obtain control over phase-matching constraints in $\chi^{(2)}$ crystals called quasi-phase-matching (QPM) [79]. QPM is achieved by periodically inverting the sign of the $\chi^{(2)}$ nonlinearity of a crystal by application of a high voltage to the regions where the nonlinearity needs to be reversed. The periodic poling transforms the constant second-order susceptibility in to a form best described by the Fourier expansion:

$$\chi^{(2)} \rightarrow \chi^{(2)} \sum_{m=-\infty}^{\infty} G_m \exp i \left[m \left(\frac{2\pi}{\Lambda} \right) z \right], \tag{2.11}$$

where Λ is the period of the domain poling and the Fourier coefficient G_m describes the shape of the $\chi^{(2)}$ modulation. The motivation for applying domain inversions to the crystal becomes apparent by looking at the modification to the phase matching criteria of both SFG and DFG when the second-order susceptibility given by Eq. 2.11 is substituted in to

Eq. 2.10. The modified phase-matching conditions are now

$$\Delta k_{\mathrm{SFG}} + \frac{2\pi}{\Lambda} = k(\omega_1) + k(\omega_2) - k(\omega_3) + \frac{2\pi}{\Lambda} = 0, \tag{2.12}$$

$$\Delta k_{\mathrm{DFG}} - \frac{2\pi}{\Lambda} = k(\omega_1) - k(\omega_2) - k(\omega_3) - \frac{2\pi}{\Lambda} = 0. \tag{2.13}$$

Equations 2.12 and 2.13 demonstrate that careful implementation of domain poling allows for tailored crystals to be fabricated to enable efficient conversion in any desired three-wave mixing process. This effect is visualised in Fig. 2.1, which depicts the amplitudes of fields

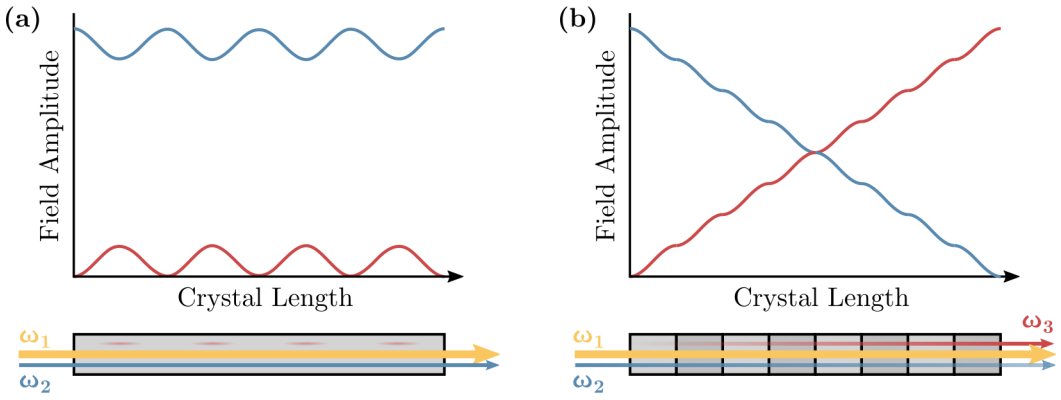

Figure 2.1 Illustration of field amplitude gain in (a) a non phase-matched bulk crystal and (b) a periodically-poled quasi-phase-matched crystal. The blue line denotes the input field and the red is the target field.

interacting through DFG in both an unpoled (a) and a poled (b) $\chi^{(2)}$ crystal. Further tuning of the phase mismatch may be achieved by exploiting the temperature dependant refractive index of the nonlinear material used, typical examples of which are lithium niobate ($LiNbO_3$) and potassium titanyl phosphate (KTP).

2.1.3 Quantum three-wave mixing

We have seen in section 2.1.1 that decomposing the polarisation response under a classical treatment, given a single monochromatic field, yields an expression for SHG and OR (Eq.2.8). We then saw that in order for SFG/DFG terms to be recovered a second input

field is required (Eq.2.10). With a classical treatment SFG and DFG cannot be predicted to occur without the presence of a second field.

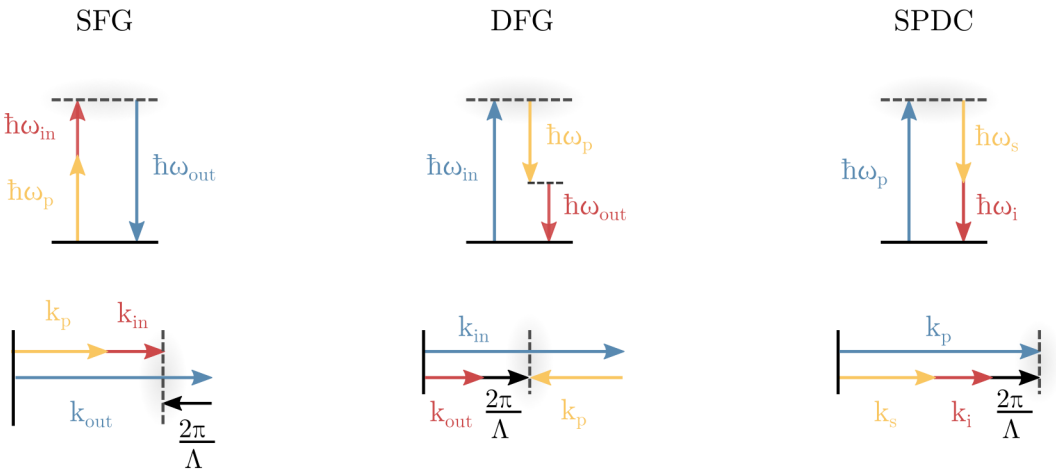

Figure 2.2 Energy and phase matching conditions for SFG, DFG and SPDC. Physical pump fields possess finite spectral bandwidths, meaning that the strict energy correlations are relaxed in reality. This relaxation is illustrated by the blurred regions in the energy level diagrams. Similarly, in real experiments phase matching conditions will also relax due to the finite crystal lengths. In addition, note that the -1st and +1st QPM orders are used for SFG and DFG, respectively, as indicated by the different directions of the grating vectors.

In the quantum mechanical description we need to include the possibility that fluctuations in the vacuum field will seed a DFG process, to which the usual energy conservation and phase matching restrictions apply. This process in which light is generated by vacuum fluctuations is referred to as spontaneous parametric down conversion (SPDC). Photon sources based on SPDC are ubiquitous in quantum optics labs as they are essential tools for a wide range of experiments. However, in the context of frequency conversion experiments, photons generated by SPDC serve only as a source of potential noise. Energy and phase matching conditions for SFG, DFG and SPDC in QPM crystals are illustrated in Fig. 2.2.

2.1.4 Phase matching in $\chi^{(2)}$: spectral engineering

In this section a theoretical two-photon state description is introduced. This description is frequently used to gain insight into $\chi^{(2)}$ interactions and evaluate the output state of photon sources, but yields great insight also for QFC by three-wave mixing. We adopt a convenient labelling for the two processes, denoting the SPDC daughter photons as signal (s) and idler (i), and the input and output fields of frequency conversion (FC) by SFG/DFG as 'in' and 'out', respectively. The photon states of both SPDC and frequency-conversion processes are given by:

$$|\psi_{\mathrm{SPDC}}(\omega_\mathrm{i},\omega_\mathrm{s})\rangle = \int_0^\infty \mathrm{d}\omega_\mathrm{i} \int_0^\infty \mathrm{d}\omega_\mathrm{s} f(\omega_\mathrm{i},\omega_\mathrm{s}) \hat{a}_\mathrm{i}^\dagger(\omega_i) \hat{a}_\mathrm{s}^\dagger(\omega_\mathrm{s}) |0_\mathrm{s}, 0_\mathrm{i}\rangle, \tag{2.14}$$

$$|\psi_{\mathrm{FC}}(\omega_\mathrm{in},\omega_\mathrm{out})\rangle = \int_0^\infty \mathrm{d}\omega_\mathrm{in} \int_0^\infty \mathrm{d}\omega_\mathrm{out}\, g(\omega_\mathrm{in},\omega_\mathrm{out}) \hat{a}_\mathrm{in}(\omega_\mathrm{in}) \hat{a}_\mathrm{out}^\dagger(\omega_\mathrm{out}) |n_\mathrm{out}, n_\mathrm{in}\rangle. \tag{2.15}$$

The functions $f(\omega_\mathrm{i},\omega_\mathrm{s})$ and $g(\omega_\mathrm{in},\omega_\mathrm{out})$ are the joint spectral amplitude (JSA) functions of SPDC and FC, from which the joint spectral intensities (JSIs) are calculated as $|f(\omega_\mathrm{i},\omega_\mathrm{s})|^2$ and $|g(\omega_\mathrm{in},\omega_\mathrm{out})|^2$. In the case of PDC the JSI dictates with what probability a signal photon with frequency ω_s is created with a corresponding idler photon with frequency ω_i. In the case of frequency conversion the JSI represents the probability of the input photon with frequency ω_in being spectrally remapped to a an output photon with ω_out. The joint spectral amplitude functions are themselves composed of two parts,

$$f(\omega_\mathrm{i},\omega_\mathrm{s}) = \alpha(\omega_\mathrm{i}+\omega_\mathrm{s})\Phi_{\mathrm{SPDC}}(\omega_\mathrm{i},\omega_\mathrm{s}), \tag{2.16}$$

$$g(\omega_\mathrm{in},\omega_\mathrm{out}) = \alpha(\pm\omega_\mathrm{out} \mp \omega_\mathrm{in})\Phi_{\mathrm{FC}}(\omega_\mathrm{in},\omega_\mathrm{out}). \tag{2.17}$$

The α terms are pump-envelope functions (PEFs), which in this thesis we describe with Gaussian spectral distributions. These terms reflect the energy conservation requirements,

and are dependent on the pump spectral bandwidth:

$$\alpha(\omega_{\mathrm{i}}+\omega_{\mathrm{s}}) = \exp\Big(-\frac{[\,(\omega_{\mathrm{i}}-\omega_{\mathrm{i},0})+(\omega_{\mathrm{s}}-\omega_{\mathrm{s},0})\,]^2}{2\sigma_{\mathrm{p}}^2}\Big), \tag{2.18}$$

$$\alpha(\pm\omega_{\mathrm{in}}\mp\omega_{\mathrm{out}}) = \exp\Big(-\frac{[\pm(\omega_{\mathrm{in}}-\omega_{\mathrm{in},0})\mp(\omega_{\mathrm{out}}-\omega_{\mathrm{out},0})\,]^2}{2\sigma_{\mathrm{p}}^2}\Big). \tag{2.19}$$

Here, the 1/e bandwidth of the pump is given as σ_{p}, and is related to the FWHM by $\sigma_{\mathrm{p}} = \Delta\omega_{\mathrm{FWHM}}/2\sqrt{4ln2}$. The phase-matching functions (PMFs) in Eq.2.16 and Eq.2.17, Φ_{SPDC} and Φ_{FC}, are derived from considering the phase mismatch of each process and evaluating a z-integration across the crystal length L:

$$\int_0^L \mathrm{d}z\exp\big(i\Delta k_{\mathrm{SPDC}}z\big) = L\underbrace{\mathrm{sinc}(\frac{\Delta k_{\mathrm{SPDC}}L}{2})\exp\big(i\frac{\Delta k_{\mathrm{SPDC}}L}{2}\big)}_{\Phi_{\mathrm{SPDC}}}, \tag{2.20}$$

$$\int_0^L \mathrm{d}z\exp\big(i\Delta k_{\mathrm{FC}}z\big) = L\underbrace{\mathrm{sinc}\,(\frac{\Delta k_{\mathrm{FC}}L}{2})\exp\big(i\frac{\Delta k_{\mathrm{FC}}L}{2}\big)}_{\Phi_{\mathrm{FC}}}. \tag{2.21}$$

The phase mismatch terms are $\Delta k_{\mathrm{SPDC}} = k_{\mathrm{pump}} - k_{\mathrm{s}} - k_{\mathrm{i}} + \frac{2\pi}{\Lambda}$ and $\Delta k_{\mathrm{FC}} = k_{\mathrm{pump}} \pm k_{\mathrm{in}} \mp k_{\mathrm{out}} + \frac{2\pi}{\Lambda}$. We note that these are entirely related to the SFG and DFG phase-matching terms that were introduced in equations 2.12 and 2.13. However, here we have folded the QPM wave vector in to the Δk terms for convenience of notation, but also generalised both SFG and DFG in to a singular FC form as with the entire discussion of the two-photon state. Recall also that SPDC is but a special case of DFG and it is clear that the theoretical treatment outlined in this section is equally applicable to all the forms of three-wave mixing we have discussed.

In Fig. 2.3 we show example phase-matching and pump-envelope functions, as well as the joint-spectral amplitude and intensity, for a DFG conversion from ∼710 nm to ∼1310 nm. For this example we selected a 0.5-nm bandwidth pump which is tuned to 1550 nm. A broader or narrower bandwidth selection would increase or decrease the width of the PEF,

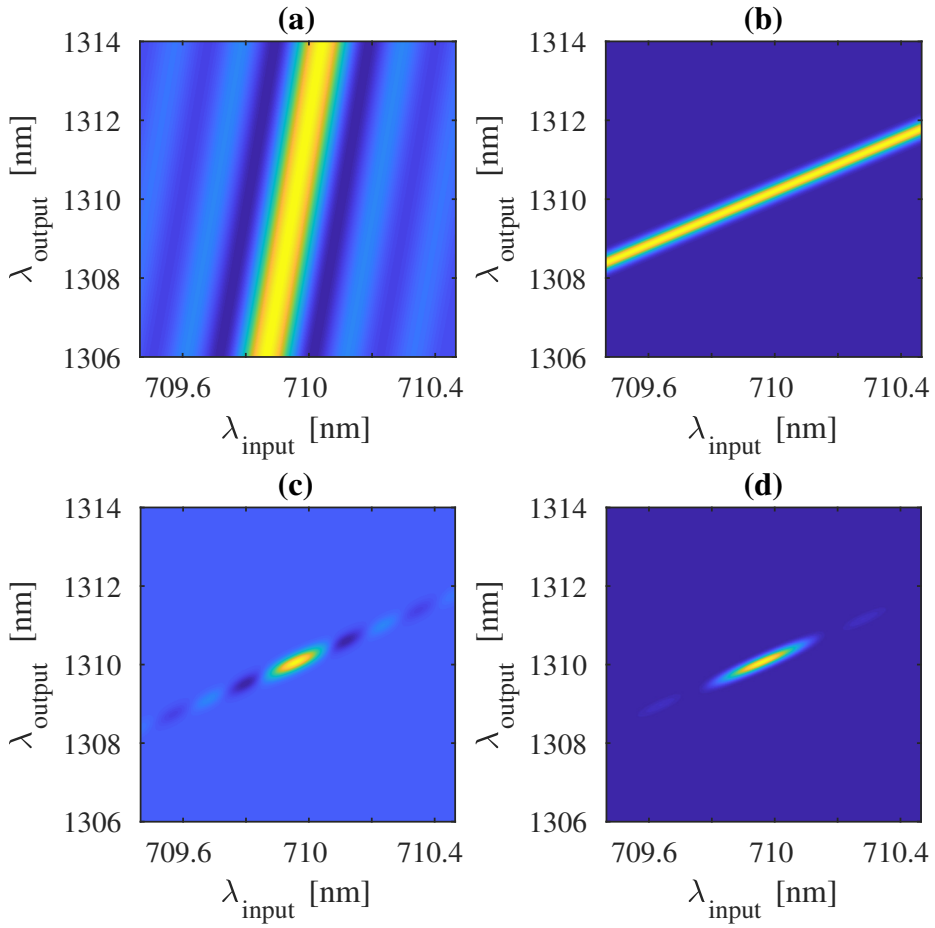

Figure 2.3 Numerical simulated results for DFG conversion from 710 nm to 1310 nm in a 15.25-µm pitch PPLN crystal. (a) Phase-matching function. (b) Pump-envelope function. (c) The real component of the joint-spectral amplitude. (d) Joint-spectral distribution.

respectively. The 2-cm long crystal is phase matched by selecting a poling period of 15.25µm and a temperature of 190 °C. Increasing the length of the crystal will reduce the width of the sinc-profile phase matching function. Adjusting either the pump-envelope or phase-matching function will enable the joint spectra to be modified as a result. In application of quantum frequency conversion it is advantageous to have a narrow pump envelope and hence a highly correlated joint spectra, as this ensures the remapping of photons from a single spectral mode to another single-frequency mode.

2.2 Experimental discussion

2.2.1 Frequency conversion requirements and design

To realise a functioning fibre-linked quantum network, translation of photons from node wavelengths to the telecoms C band is critical and having a two-way link is preferential. The majority of frequency conversion experiments have been uni-directional, with limited exception [70]. Furthermore, existing QFC experiments have mostly targeted transitions in the red and NIR. Recent progress has resulted in demonstrations translating quantum states between ultraviolet and the O band [68,69]. However, assembling an ion trap based network, like the Q20:20 engine envisioned by NQIT, will require direct links between blue ion transitions and the telecoms C band.

We target the conversion of light between the telecommunication C band (1530-1565 nm) and the $S_{1/2} \rightarrow P_{1/2}$ transition wavelength of trapped Sr^+ ions at 422 nm. Due to the large wavelength separation between 422 nm and the telecoms C band, the phase matching criteria given in Eq.2.12 and Eq.2.13 requires a crystal poling period far smaller than what is commercially produced. For our experiment we use a magnesium-doped periodically-poled lithium niobate (MgO:PPLN) crystal, which is custom-designed and fabricated in collaboration with Covesion Ltd [1].

To fabricate each of the bespoke MgO:PPLN crystals, photoresist patterns are written on to the (-z) surface of a 0.5-mm-thick, 76-mm-diameter, z-cut MgO:$LiNbO_3$ wafer. Liquid electrodes are applied to both the patterned -z and unpatterned +z surfaces to enable electrical contact. Domain inversions along the z axis are performed by voltage-controlled application of an electric field predicated on a first stage, domain nucleation, exceeding the coercive field of the crystal, and a second stage, domain spreading, close to the coercive field ($\sim$4.5 kV mm^{-1}). This proprietary technique results in domains that bridge the entire 0.5-mm-thickness of the crystal. The MgO:PPLN wafer is then diced and polished into multiple

[1] https://www.covesion.com

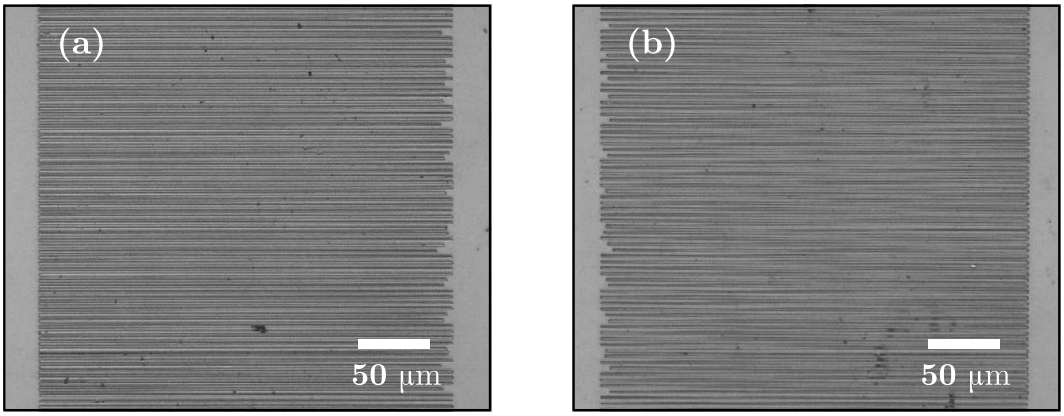

Figure 2.4 Optical micrographs of the (a) +z and (b) -z surface of a 3.75-µm pitch MgO:PPLN crystal.

chips, each possessing five 300 µm-wide gratings with poling periods 3.75, 3.85, 3.95, 4.05, and 4.15 µm respectively. Figure 2.5 shows calculated DFG phase matching contours for MgO:PPLN with a temperature of 150 °C for the set of poling periods fabricated in the crystal. It is apparent that converting light at 422 nm to the target wavelength in telecoms C band requires the smallest of the gratings available (3.75 µm) be used, and that a pump laser tuneable to around ∼580 nm is required.

The temperature dependant refractive index of the crystal allows for fine tuning of the phase matching provided by a given grating. In Fig. 2.6, phase-matching contours (PMCs) are shown for three temperatures of a 3.75-µm pitch grating at three set temperatures. Of course, the temperature range over which a crystal should be tuned is finite. Operating PPLN crystals in a temperature range between 100 and 200 °C is a standard procedure used to limit the photorefractive effect [80]; in areas of high optical intensity electrons are photoexcited and released as free carriers, which will redistribute to regions of the crystal of lower optical intensity. The result of this redistribution is a spatially varying refractive index of the crystal, which causes both beam distortions and increased phase mismatch. Heating of the crystal is necessary therefore to ensure that free electrons are diffused more evenly throughout the PPLN crystal.

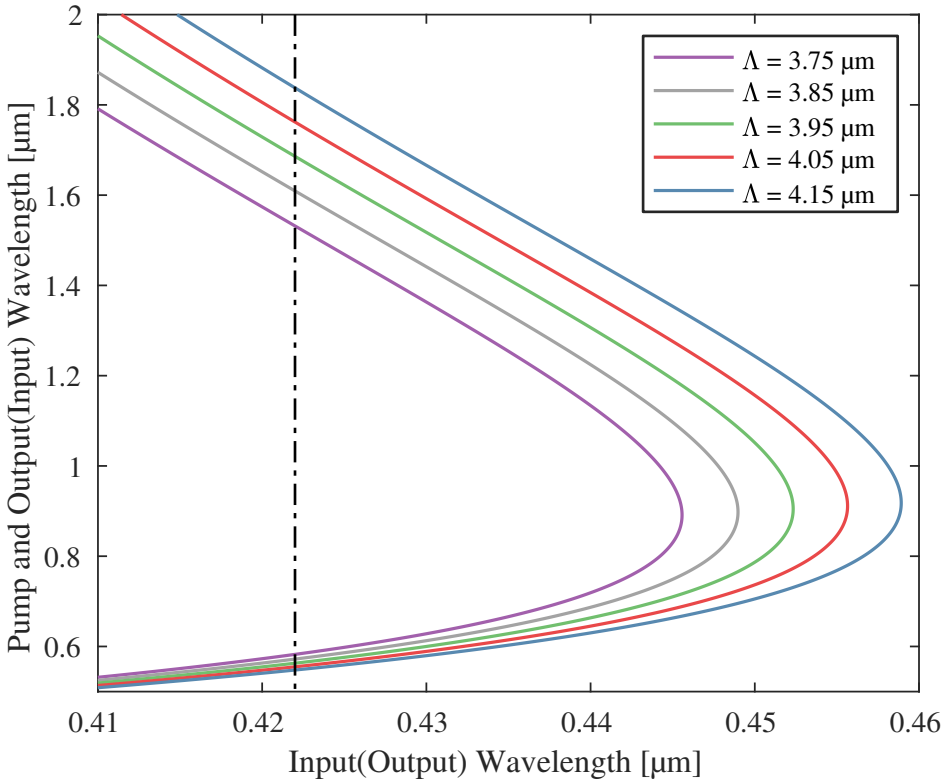

Figure 2.5 DFG(SFG) phase-matching contours for different poling periods in a MgO:PPLN crystal at 150 °C. A poling period of 3.75 µm provides the capability to frequency convert between 422 nm and the C band. The dashed line at 422 nm indicates the $S_{1/2} \rightarrow P_{1/2}$ transition wavelength of trapped Sr^+ ions.

The 5 % MgO doping of the lithium niobate crystal in this experiment increases the interface's photorefractive resistance. MgO:PPLN is better suited for high power applications, but also for use with visible wavelengths where photon energy is higher and the photorefractive effect more severe. It can also be operated from room temperature up to > 200 °C, significantly increasing the wavelength tuneability of the device.

2.2.2 Phase-matching characterisation

In order to verify the suitability of the fabricated MgO:PPLN crystals for achieving efficient conversion we characterise the phase matching capability of the 3.75-µm grating. The experimental setup for characterising the phase matching by SFG is shown in Fig. 2.7. An

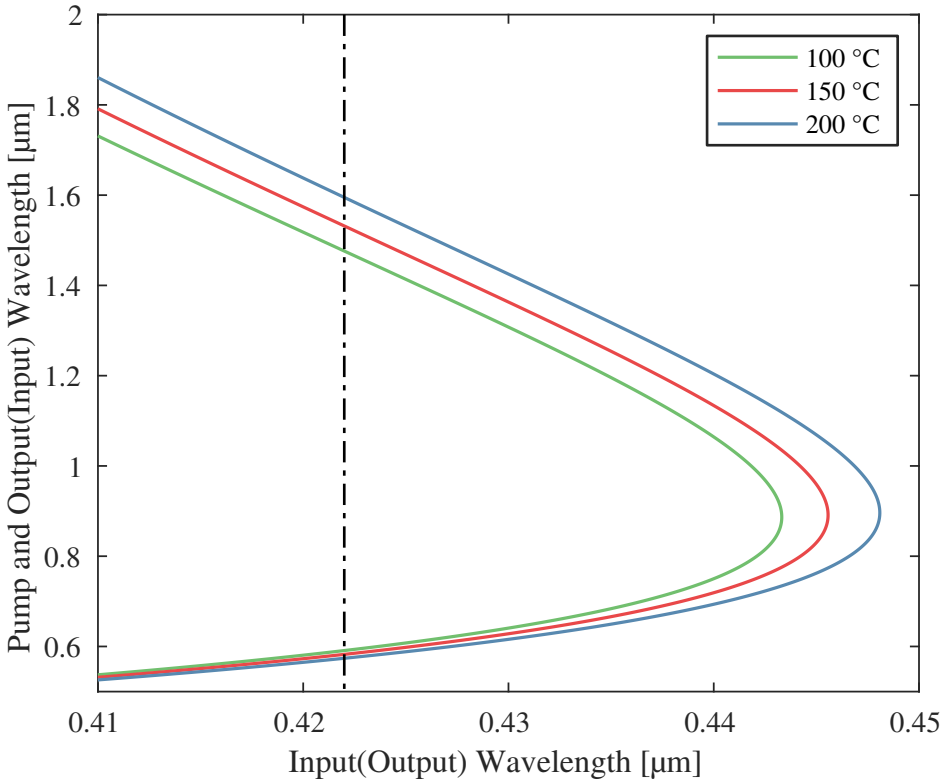

Figure 2.6 The DFG(SFG) phase matching contours for 3.75-µm pitch MgO:PPLN change with the temperature of the crystal allowing for fine tuning of the phase matching. The dashed line at 422 nm indicates the $S_{1/2} \rightarrow P_{1/2}$ transition wavelength of trapped Sr^+ ions.

80-MHz synchronously pumped dye laser (Sirah Gropius), wavelength-tuned to 580 nm and operating at 30-ps pulse duration, provides the strong optical pump field for the conversion. The coherent source for the IR input is obtained from a tuneable continuous-wave (CW) laser with a 40-MHz linewidth (Santec TSL 510-C), which is attenuated down to low mean photon numbers using neutral-density filters (NDFs). The input and pump beam size and polarisation are set using Keplerian telescopes, polarising beam splitters (PBSs) and half-wave plates (HWPs) before the beams are combined at a dichroic mirror (DM) and directed towards the oven-mounted MgO:PPLN crystal. A pair of identical fused silica lenses are then used to focus the overlapped beams in to the crystal and re-collimate the emerging fields.

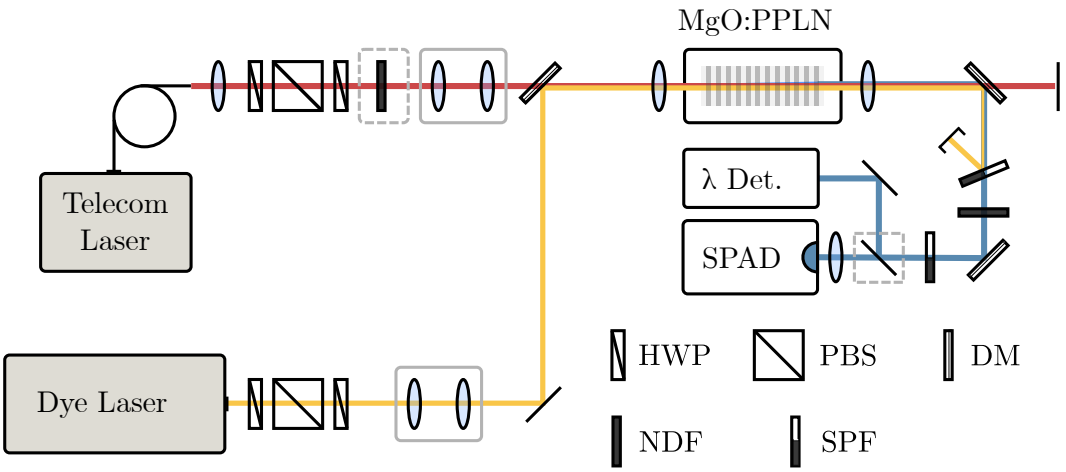

Figure 2.7 Schematic of the experimental setup for characterising the phase matching of 3.75-µm MgO:PPLN grating. The pump beam (yellow) and IR field (red) are initialised by setting the beam size and polarisation using telescopes, polarising beam splitters and half-wave plates. The 580-nm pump beam from the dye laser is overlapped with the wavelength-tuneable IR input field at a dichroic mirror, and directed towards the MgO:PPLN crystal through a focusing lens. After the crystal, the pump, unconverted IR input light and successfully converted violet output are re-collimated and then separated using dichroic mirrors and a short-pass filter, with the converted light being directed to either a SPAD or a spectrometer. The MgO:PPLN crystal is temperature-controlled using an oven.

To maximise spatial overlap of the fields along the crystal length, conscious effort is needed to both closely match the Rayleigh length of each beam to half of the 19.97-mm crystal length, whilst also minimising the difference between the cross sections of the two beam waists within the crystal. The selected values for these spatial parameters are displayed in Table 2.1.

Wavelength [nm]	Rayleigh Length [mm]	Min. Beam Radius [µm]
1550	8.11	63.3
580	10.1	43.2

Table 2.1 Spatial properties of the beams in the MgO:PPLN crystal.

Following the crystal, the pump, unconverted IR input light and successfully converted violet output are separated with a dichroic mirror, with the converted light being directed to a single-photon avalanche diode (SPAD). To further isolate the violet wavelength, the pump

light is filtered out using short-pass filters (SPFs) at 500 nm and 440 nm as well as a dichroic mirror with an edge at 500 nm. The remaining signal is measured using a blue-enhanced Si SPAD with a detection efficiency and dark count rate of 86 % and 6 Hz. The wavelength of the converted light is monitored using an electron-multiplying CCD spectroscopy detector.

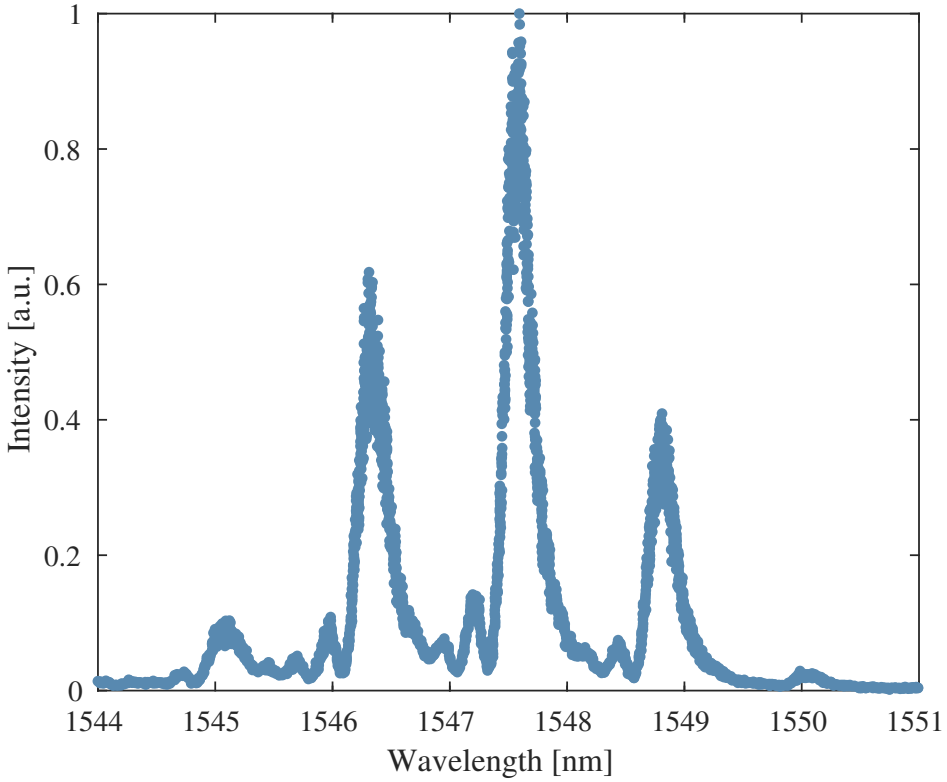

Figure 2.8 SFG phase-matching contour for 3.75-µm pitch MgO:PPLN, i.e., violet output power as a function of the input telecom wavelength.

With the temperature of the crystal stabilised at 160°C, the input IR beam is swept in wavelength whilst the intensity of the converted violet light is measured, mapping out the phase matching curve for a pump wavelength of 579.6 nm. We observe several distinct peaks in the phase matching, shown in Fig. 2.8. The presence of multiple peaks is indicative of either multiple frequency modes within the pump beam or inhomogeneous poling across the length of the crystal. It is possible that this has detrimental consequences on the potential

conversion efficiency achievable in our interface, and will be discussed further in Section 2.2.3.

To assess the tuning range of the 3.75-µm grating we measure the change in position of the the central phase-matching peak as a function of temperature. For eight distinct crystal temperatures we sweep the input IR wavelength whilst measuring the output violet power using a SPAD. For the input IR light we measure a temperature response of $\Delta\lambda_{\text{in}}/\Delta T = 0.4\,\text{nm/K}$, corresponding to the a change in the output wavelength of $\Delta\lambda_{\text{out}}/\Delta T = 0.0297\,\text{nm/K}$.

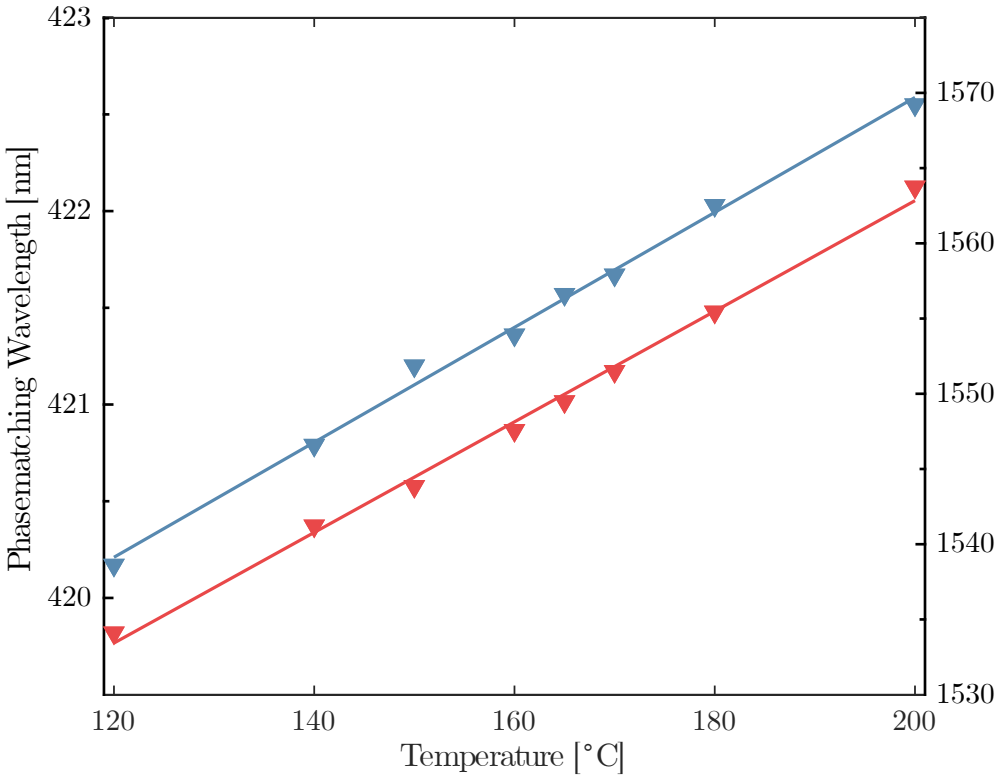

Figure 2.9 Experimental measure of the change in position of the SFG central phase matching peak as a function of MgO:PPLN temperature.

2.2.3 Analysis of phase matching characteristics

As previously mentioned, the several distinct peaks in the phase matching Fig. 2.8 are indicative of either multiple frequency modes within the pump beam or inhomogeneous poling

across the length of the crystal. We can use the numerical spectral analysis established in section 2.1.4 to assess the possibility of inhomogeneity in the crystal poling. It is necessary however to calculate the phase-matching function by explicitly considering the contribution from each domain. Rather than taking the form expressed in Eq.2.21, a sum of sinc like contributions to the phase-matching function is used [81]:

$$\Phi_{\mathrm{INHM}} = \sum_{j} (-1)^{j+1} \left[\exp(-ikz_j) - \exp(-i\Delta k z_{j-1})\right], \tag{2.22}$$

where $z_{j-1} - z_j$ is the width of each domain. If then for this form we introduce a random error associated with each poling width and calculate a joint spectrum, we will be able to produce a marginal distribution representative of an inhomogeneously poled crystal that may be compared to the experimental phase matching peaks shown in Fig. 2.8. We perform the numerical simulation, evaluating the joint spectra for SFG in a crystal with the same design properties and temperature as the experimental device. Domain widths are randomly assigned from a normal distribution with a standard deviation corresponding to a 1% error in the poling width.

Figure 2.10 contains the numerically simulated phase matching functions for both (a) a perfectly poled crystal and (b) a crystal with a 1% standard deviation error in domain widths. The resulting joint spectra for the perfect and imperfect MgO:PPLN crystals are shown in (c) and (d), respectively. We see from these results that even a 1 % distribution in the individual poling domain widths will drastically change the appearance of the joint spectrum of the device, with many high intensity lobes distributed along the intersection between the pump-envelope function and the multiple overlapping sinc contributions of the modified phase-matching function.

The experimental characterisation of the MgO:PPLN crystal phase matching constructs the marginal distribution at the input wavelength summed over all energy matched pump

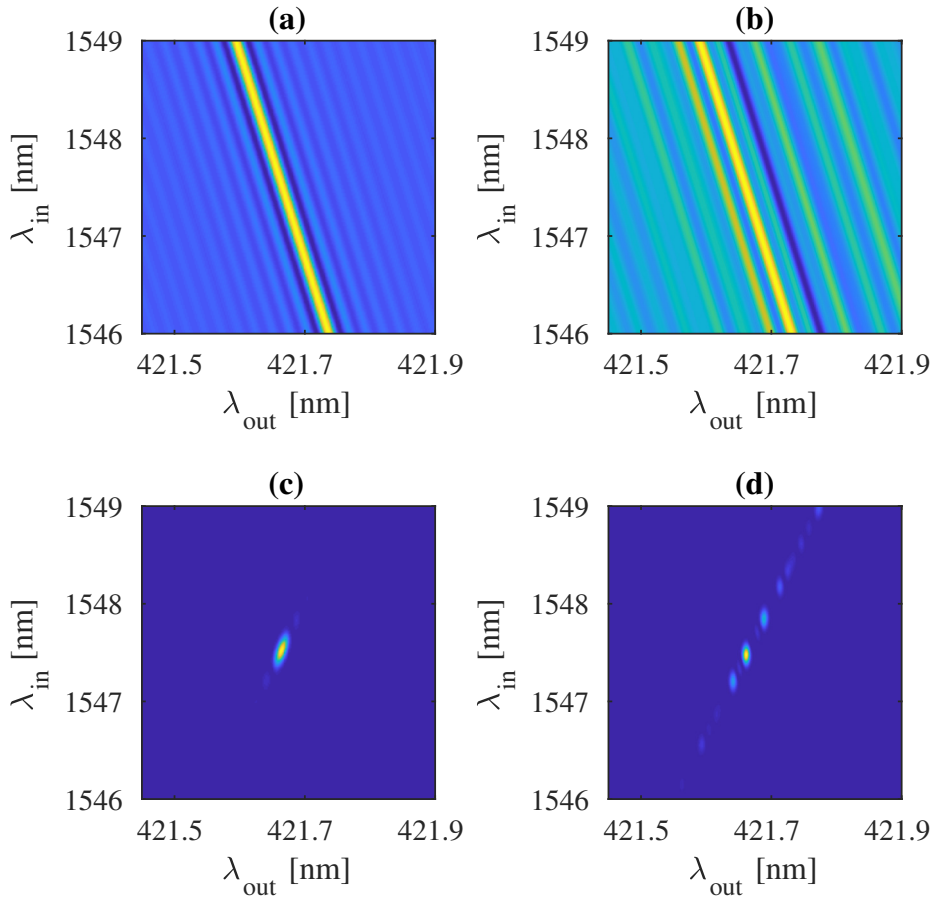

Figure 2.10 Simulated SFG conversion from ∼ 1547.5 nm to ∼ 421.7 nm in 3.75-µm pitch MgO:PPLN. PMFs for (a) perfectly and (b) imperfectly poled crystal. JSIs for (c) perfectly and (d) imperfectly poled crystal.

and output wavelengths, which allows for a direct comparison with the simulated result's joint spectra. In Fig. 2.11 we show the marginal distribution of input wavelength for the perfect and imperfect crystal simulations as well as the experimental measurement of output intensity as a function of input wavelength.

The existence of multiple peaks within both the measured phase-matching contour and the simulated inhomogeneous equivalent does indicate that small variances in the fabricated domain widths may be present. If this is the case we will expect a reduced conversion efficiency from our device when compared to a perfectly poled MgO:PPLN crystal. However,

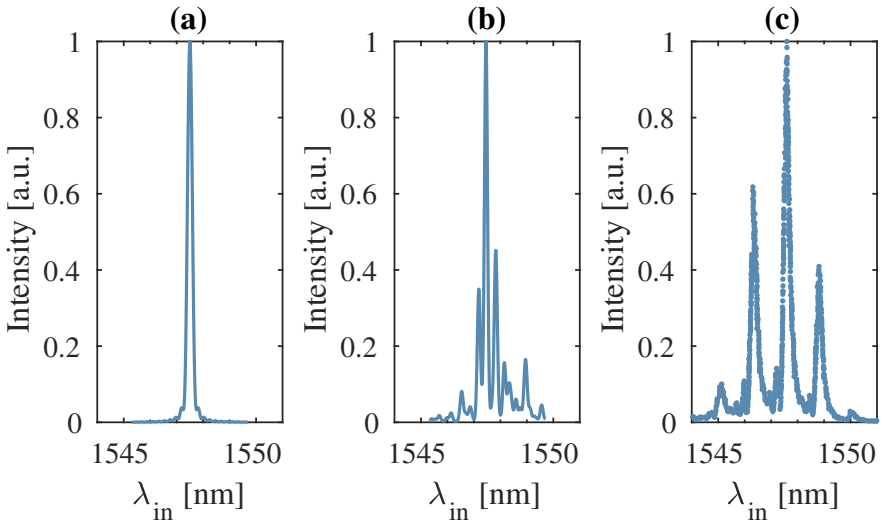

Figure 2.11 Simulated marginal distribution of input wavelength for the (a) perfect and (b) imperfect crystal, as well as (c) the experimental measurement of output intensity as a function of input wavelength.

there is an important difference between the results in Fig. 2.11 (b) and (c), which is that the simulated case, being the result of a random distribution of domain widths, will not always produce evenly distributed peaks comparable to the experimental result. While a random distribution of >10,000 domain widths may result in the accumulation of phase leading to such a contour, it would be more reasonable to assume that the experimental phase-matching contour may have been shaped by the presence of multiple spectral modes in the pump beam. However, if there is a slow periodic variation in the domain widths across the length of the crystal then such regularly-spaced sidebands might be expected.

Note that introducing multiple frequency modes in the pump would mean that the power of the pump field we measure passing through the crystal would be higher than that present within the frequency mode which contributes to the conversion process. The presence of additional frequency modes would serve only to introduce noise into the experiment and over inflate the pump power requirements we record. Whether the result of inhomogeneous poling or additional pump frequency modes, the experimentally obtained phase-matching contour

shows an existing limitation on the performance of the frequency conversion interface.

2.2.4 Frequency up-conversion

With considerations of the crystal phase matching response taken in to account, we explore the attainable efficiency of up-conversion using the MgO:PPLN device. The experimental setup for characterising SFG up-conversion expands upon that which is used to interrogate the phase matching, and is shown in Fig. 2.12.

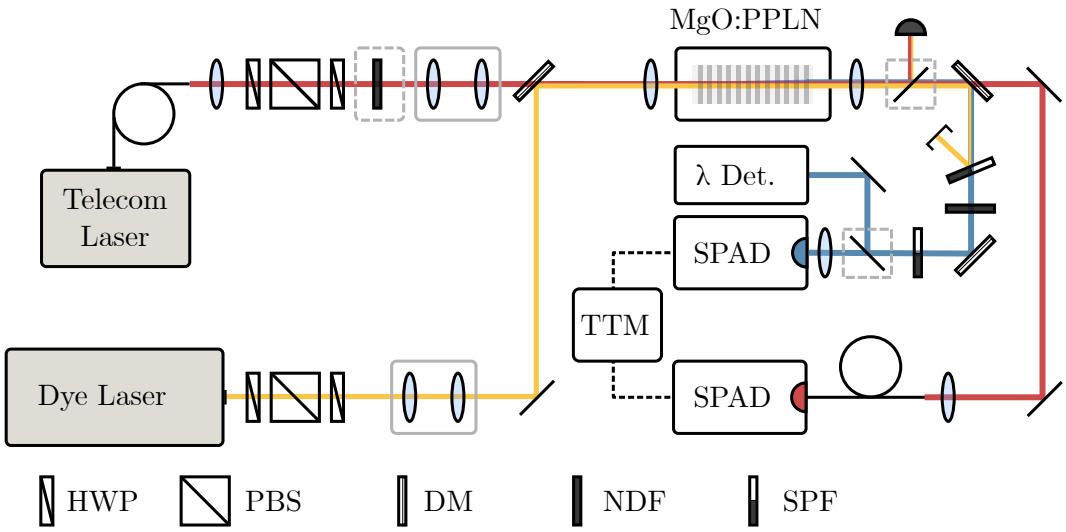

Figure 2.12 Schematic of the experimental setup for characterising frequency up-conversion of an attenuated coherent state from 1547.6 nm to 421.7 nm. The pump beam (yellow) and IR field (red) are initialised by setting the beam size and polarisation using telescopes, polarising beam splitters and half-wave plates. The IR input intensity is attenuated to low mean photon numbers using an ND filter. The two beams are then overlapped at a dichroic mirror and directed towards the MgO:PPLN crystal through a focusing lens. After the crystal, the pump, unconverted IR input light and successfully converted violet output are re-collimated and then separated using dichroic mirrors and a short-pass filter, with the converted light being directed to either a SPAD or a spectrometer. The intensity of the residual IR field is monitored on a second SPAD. TTM denotes the time-tagging module.

The 80-MHz synchronously pumped dye laser is wavelength-tuned to 579.6 nm and operated at 30-ps pulse duration. We tune the 40-MHz-linewidth CW input to 1547.6 nm and maintain the same spatial and polarisation overlap with the pump beam in the crystal. The

MgO:PPLN crystal temperature is set at 160 °C.

Following the crystal, we introduce a flipper mirror which allows for the input and pump powers transmitted through the crystal to be measured. After this a dichroic mirror separates the unconverted IR input light, which is monitored using a single-mode-fibre (SMF) coupled InGaAs SPAD with 9.5 % detection efficiency. The pump light is removed from the successfully up-converted beam using the same filtering as before: short pass filters at 500 nm and 440 nm and a dichroic mirror with an edge at 500 nm. We continue to use the Si SPAD with a detection efficiency and dark count rate of 86 % and 6 Hz to monitor the remaining signal. We verify the wavelength of the converted light using the electron-multiplying CCD camera.

An important metric to assess is the external efficiency, η_{ext}, of the SFG conversion. We define the external efficiency as a ratio between the mean number of converted photons leaving the crystal and the number of input photons incident and temporally overlapped with the pump. The duty cycle, D, representing the difference in temporal properties between the two, is the ratio between pump pulse duration, τ_{p}, and the inverse of the repetition rate: $D = \tau_{\text{p}} R_{\text{p}}$. We accordingly define the mean number of input photons, $\langle n \rangle_{\text{in}}$, as

$$\langle n \rangle_{\text{in}} = \frac{P_{\text{in}} D}{\hbar \omega_{\text{in}}}, \tag{2.23}$$

where P_{in} is the IR power transmitted through the crystal with the pump blocked. Observed drift in the IR input power requires us to measure this both before and after each integration over which we record detector counts in order to calibrate the variations in the IR counts at the InGaAs SPAD. The external conversion is efficiency given by

$$\eta_{\text{ext}} = \frac{S - N}{\langle n \rangle_{\text{in}} \eta_{\text{loss}}}, \tag{2.24}$$

where S and N are the signal and noise counts per second. The term η_{loss} accounts for

the Si detector efficiency ($\sim 86\,\%$), transmission through optical components ($\sim 96\,\%$) and, where appropriate, ND filter transmission ($\sim 20\,\%$).

SPAD detectors output a single click per detection event, with any additional photon arriving within the associated dead time going unregistered. The dead time of the Si SPAD is such that $T_\mathrm{d} \gg 1/R_\mathrm{p}$, meaning that it is important to apply the corrected count rates, S and N, instead of the raw values, S_raw and N_raw:

$$S = \frac{S_\mathrm{raw}}{1 - S_\mathrm{raw} T_\mathrm{d}}; \quad N = \frac{N_\mathrm{raw}}{1 - N_\mathrm{raw} T_\mathrm{d}}. \tag{2.25}$$

Background noise counts are recorded by blocking the IR input beam and recording counts at the Si SPAD, with the pump beam unblocked.

We attenuate the IR coherent source to overlap an average of two input photons with every pump pulse ($\langle n \rangle_\mathrm{in} = 2$), allowing us to demonstrate the capability of the device operating at low photon numbers.

The pump-power-dependent conversion efficiencies are shown in Fig. 2.13. We measure an external efficiency of $\eta_\mathrm{ext} = 9.4 \pm 0.86\,\%$, the highest recorded, with an average pump power of 180 mW. The measured conversion efficiencies are constrained by the available pump power in the experiment, which is apparent from the linear slope of the efficiency vs pump power curve.

All measurements recorded in Fig. 2.13 consisted of a 5 to 10 s integration (4×10^8 to 8×10^8 input photons). Beyond this integration time we observe a drop in the conversion efficiency caused by pump-light absorption, which heats localised areas in the crystal and modifies the phase matching. Pump-power-induced change in Δk is a phenomenon which has been discussed previously [69,82], with additional contributions from the photorefractive effect also considered. However, as discussed in Section 2.2.1, MgO:$LiNbO_3$ has a high degree of resistance to the photorefractive effect and so it is unlikely to be the dominant source of

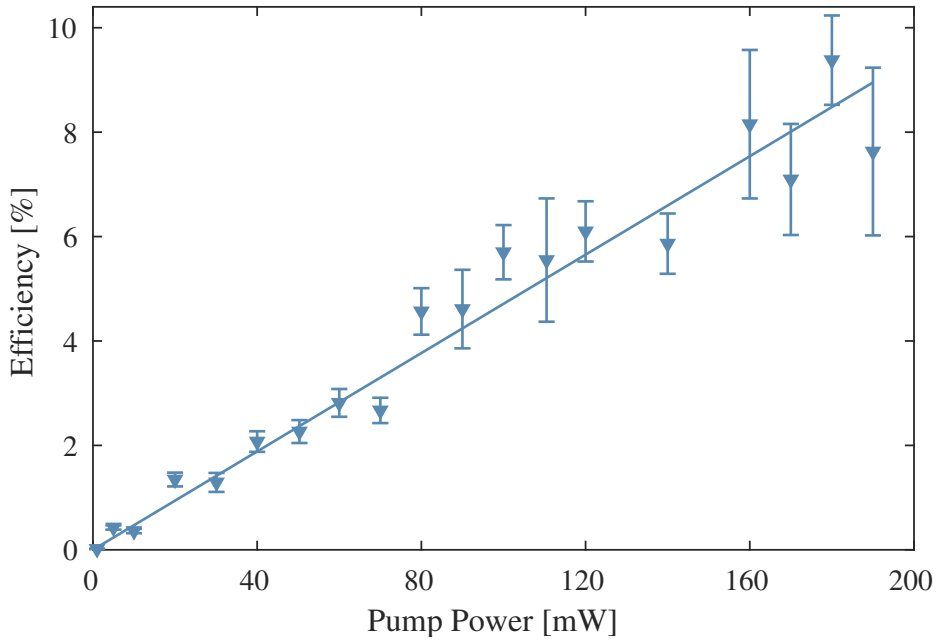

Figure 2.13 The pump-power-dependant conversion efficiency of SFG up-conversion from 1547.6 nm to 421.7 nm.

phase matching degradation here. In operating conditions the MgO:PPLN converter would be used with a constant pump power, with the temperature-tuned phase matching optimised for the selected power.

Figure 2.14 shows the pump-power-dependant signal-to-noise ratio (SNR), which is calculated SNR = S/N. With a pump power of 180 mW, the power at which η_{ext} is highest, the SNR = 39.4 ± 0.69.

2.2.5 Frequency down-conversion

The bidirectional operation of our frequency conversion device is explored by characterising the DFG conversion of weak-coherent violet light to the IR. The modified experimental arrangement is shown in Fig. 2.15.

The weak-coherent input at 425.5 nm is produced via SHG of light from an 80-MHz repetition rate Ti:sapphire laser (Spectra Physics Tsunami), which has a 300-ps pulse duration,

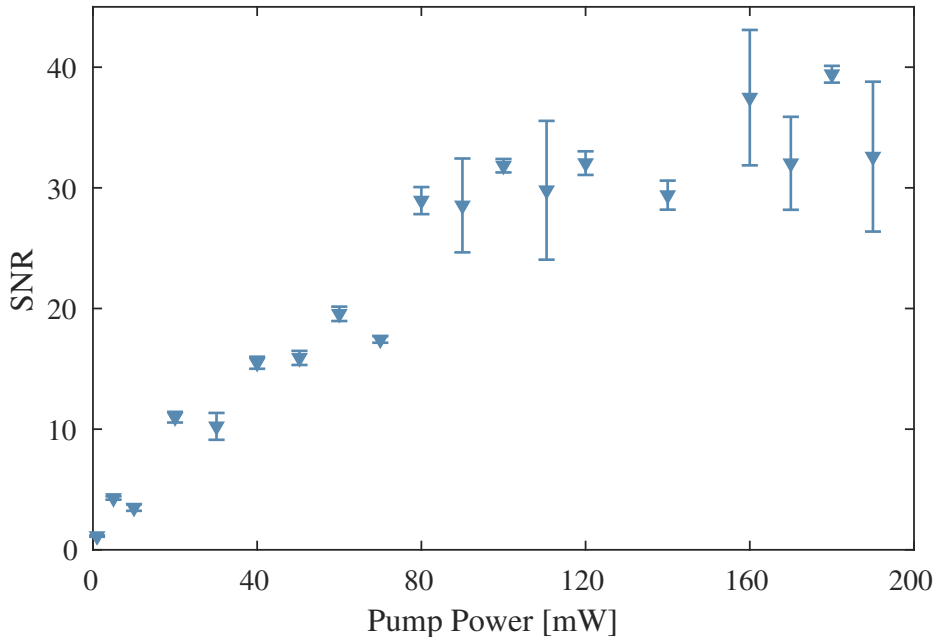

Figure 2.14 The signal-to-noise ratio of SFG up-conversion from 1547.6 nm to 421.7 nm as a function of pump power.

and is wavelength-tuned to 851 nm. The Ti:sapphire laser is synchronised to the clock signal of the dye laser system via active cavity-length control in order to optimise the overlap of the pump and input pulses.

In order to compensate for the change in the violet wavelength, the dye laser wavelength is tuned to 585 nm and the MgO:PPLN crystal temperature is set to 226.4°C. These changes result in an IR output wavelength of 1560.6 nm being phase matched. Achieving the exact reverse process of the SFG interface between 421.7 nm and 1557.6 nm is not possible due to the phase matching restriction of the beta-barium-borate (BBO) SHG crystal. In the down-conversion experiment we mitigate the pump-induced change in Δk by optimising the oven temperature whilst pumping the conversion process with an average pump power of 60 mW, which is at half of the available limit.

Differences also exist in the detection side of the experiment. The long-wavelength detection arm contains two long-pass filters with cut-off wavelengths at 950 and 650 nm.

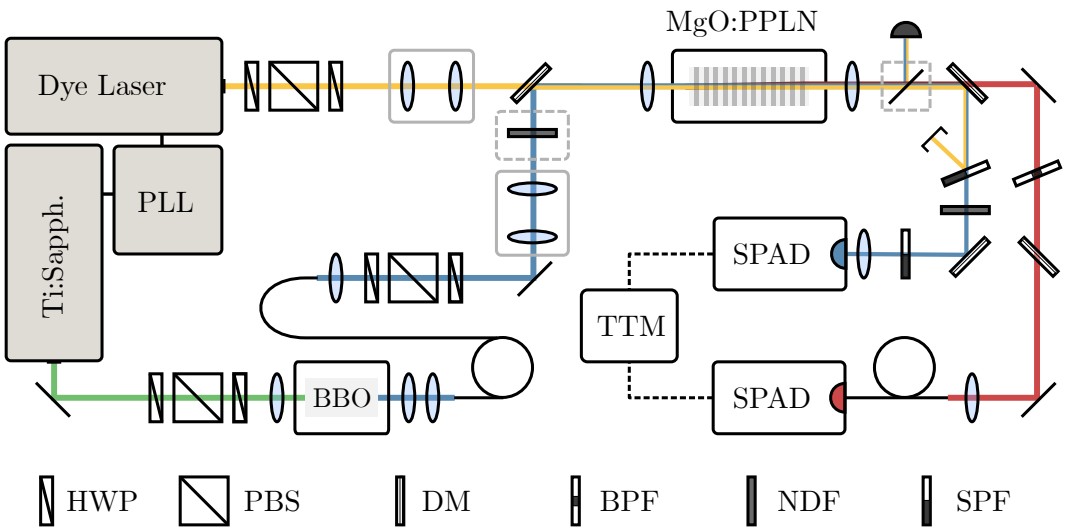

Figure 2.15 Schematic of the experimental setup for characterising frequency down-conversion from 425.5 nm to 1560.6 nm. A Ti:Sapphire laser is locked to the repetition rate of dye laser pump using a phase-locked loop (PLL). The pulses from the 851-nm Ti:Saphhire laser are frequency doubled in a BBO crystal, providing an input field at a wavelength of 425.5 nm. The pump beam (yellow) and input field (blue) are initialised by setting the beam size and polarisation using telescopes, polarising beam splitters and half-wave plates. The input field intensity is attenuated to low mean photon numbers using a ND filters. The two beams are then overlapped at a dichroic mirror and directed towards the MgO:PPLN crystal through a focusing lens. After the crystal, the pump, unconverted violet input light and successfully converted IR output are re-collimated and then separated using dichroic mirrors, a short-pass filter and a band-pass filter. Light intensities at both the violet and IR wavelengths are monitored using SPADs.

A band-pass filter is also used, which has a central wavelength of 1570 nm and a FWHM of 8.9 nm. The band-pass filter is rotated in order to shift the transmission window to accommodate the converted light at 1560.6 nm.

Figure 2.16 depicts the pump-power-dependant conversion efficiency of the DFG conversion. The external efficiency is determined using Eq. 2.24, in which the η_{loss} term accounts for losses due to the efficiency of the detector ($\sim 9.5\,\%$), transmission through optical components ($\sim 73\,\%$) and fibre coupling efficiency ($\sim 65\,\%$). The duty cycle is the ratio of the pump and input pulse durations: $D = \tau_{\text{p}}/\,\tau_{\text{in}}$. An average of two input photons are overlapped with every pump pulse, i.e. $\langle n \rangle_{\text{in}} = 2$, to ensure that comparable conditions to the SFG conversion are imposed. Detector counts are measured for integration times >15 s,

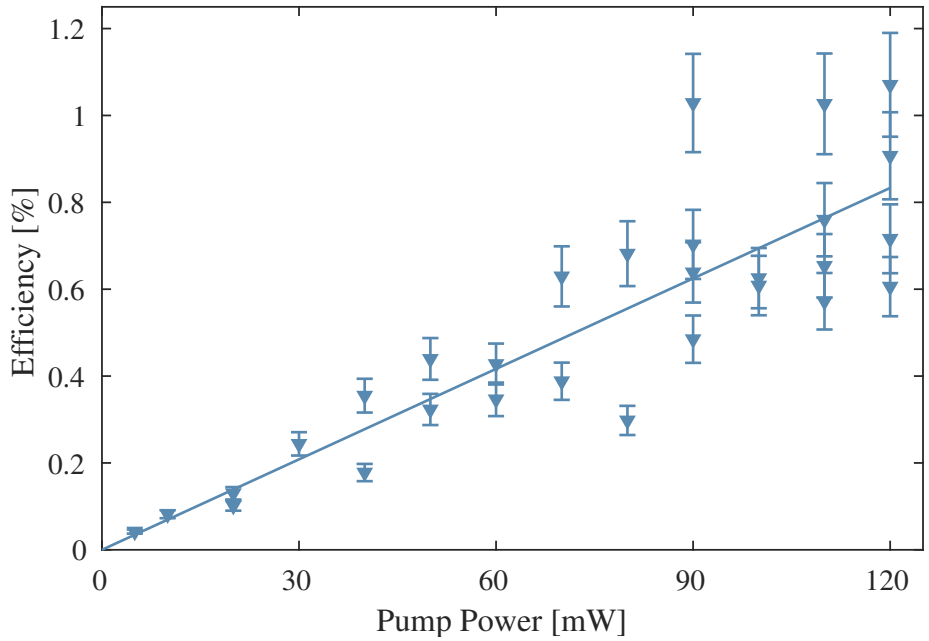

Figure 2.16 Conversion efficiency of DFG down-conversion from 425.5 nm to 1560.6 nm

such that the total input photon number is $> 2.4 \times 10^9$.

During the collection of data we observe large drifts in the optical alignment caused by environmental conditions in the laboratory. We continuously compensate for this misalignment by steering the pump and input beam using mirrors ahead of the crystal to the optimise beam overlap; as Fig. 2.16 shows, this causes a distribution of observed conversion efficiencies for select pump powers. The error bars for this figure are calculated from uncertainties associated with the input and pump pulse durations, optical losses, detector efficiencies and by applying Poissonian statistics to the total numbers of detector counts. The spatial overlap of the beams in the crystal are not accounted for in the presented uncertainties, leading to the unusual distribution in points outside the range of the error bars. The maximum recorded conversion efficiency is $1.1 \pm 0.12\,\%$, with a pump power of 120 mW. For the same pump power we achieve a significantly higher $\sim 6\,\%$ external efficiency in SFG up-conversion. It is likely that this large discrepancy in the measured conversion efficiencies

arises due to differences in the beam waist of the input between the two experiments. The pump beam has a beam waist of $\sim 43.2\,\mu m$ in both experimental configurations, while the input light beam waist is $\sim 112\,\mu m$ in the DFG down conversion and $\sim 63.3\,\mu m$ in the SFG up-conversion setup. We therefore know that the maximum proportion of the input beams overlapped by the pump for DFG and SFG are $\sim 14.9\,\%$ and $\sim 46.6\,\%$, respectively. This is clearly a limiting factor in the performance of the device, but it is reasonable to assume that a more optimised lens configuration will allow for an improvement to the external conversion efficiencies for both experiments, although in particular for the down-conversion arrangement.

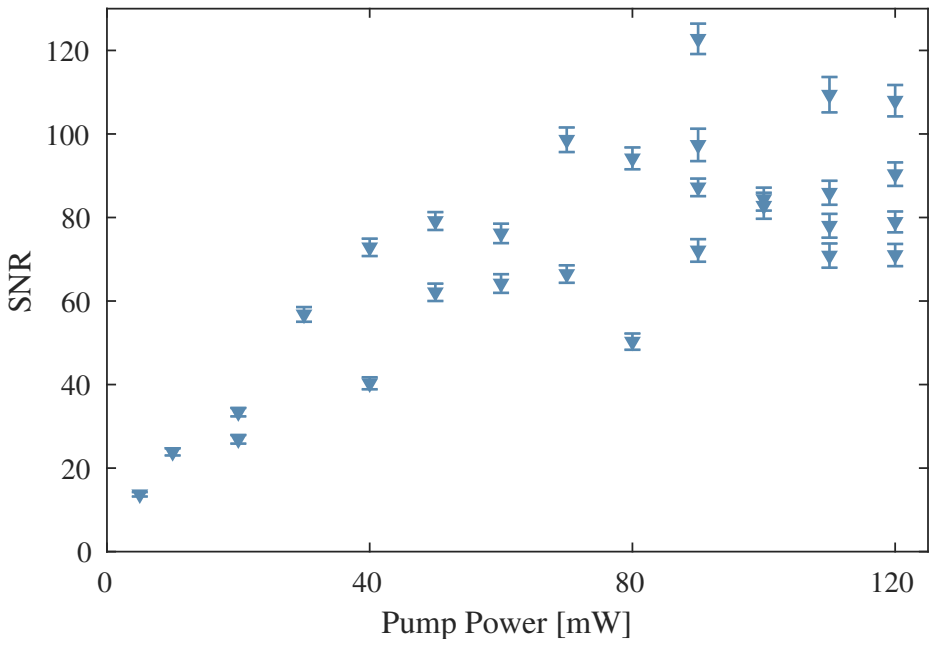

Figure 2.17 Signal-to-noise ratio of DFG down-conversion from 425.5 nm to 1560.6 nm as a function of average pump power.

The high signal-to-noise values of the down-conversion experiment are shown in Fig. 2.17; a value of 108±3.8 is achieved at the point of highest conversion. The dominating factor which results in an improved SNR is the insensitivity of the InGaAs detector to the pump wavelength, eliminating the pump-leakage contribution to the noise. Non-phase-matched

SPDC is likely the largest remaining source of noise at the detection wavelength, which would be possible to reduce further by making use of narrower bandwidth spectral filtering.

2.2.6 Noise analysis

In the context of quantum networks it is essential that single-photon-level operation of frequency-converter modules may be achieved with sufficiently low noise to avoid degrading the effective exchange quantum of information caused by quantum decoherence. To provide some indication of how suitable our interface would be for operation in a fully realised quantum network, we evaluate the performance of our device for both up- and down-conversion by calculating the lowest number of photons per pulse which would achieve SNR = 1, a metric of quantum devices referred to as μ_1 [83]. The calculated values of μ_1 are displayed in Fig. 2.18.

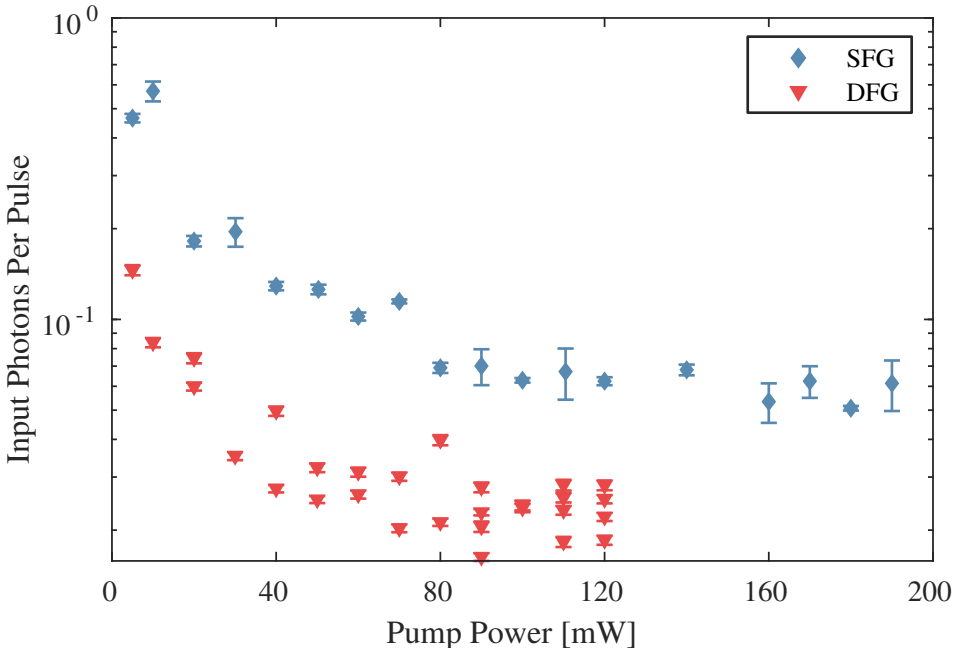

Figure 2.18 The lowest possible number of input photons per pulse to achieve a SNR≥1 as a function of pump power.

At the points of maximum recorded conversion efficiency the values of μ_1 obtained for up-

and down-conversion are 0.0507±0.0009, with a pump power of 180 mW, and 0.0185±0.0006 with a pump power of 120 mW, respectively. These numbers are far better than might have been expected — previous work [69,84–86] indicates noise processes such as SPDC of the pump field, or Raman scattering, inhibit periodically-poled-crystal frequency converters to a far greater extent than the level which we observe.

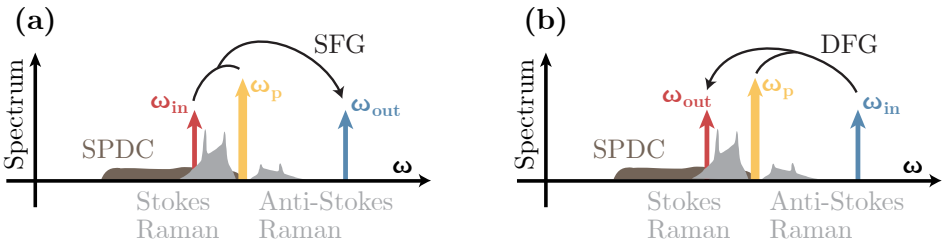

Figure 2.19 Illustration of nonlinear noise processes in the (a) sum- and (b) difference-frequency generation conversions.

Figure 2.19 illustrates the expected noise spectra for $\chi^{(2)}$ frequency converters. For down converters, it is expected that SPDC (shown in brown) will generate noise photons spectrally overlapped with the newly converted long-wavelength photons. These noise photons, which are spectrally close to the long-wavelength field, will also cascade to shorter wavelengths via SFG, meaning that detection noise will also increase for up-converters. However, in comparison to previous works in the literature [55,69,84], we observe only limited amount of noise in the IR despite using broad-band spectral filtering. In addition, because of the large frequency separation between all of our fields, light generated through Raman scattering (shown in grey) is not strongly overlapped with either input or output wavelengths. For both of these reasons, we are able to avoid the use of intrinsically high loss filtering such as narrow-band etalons, whilst still achieving low noise operation; this indicates that our device, as far as nonlinear optical noise is concerned, can be regarded as suitable for integration in to a real world quantum network.

2.2.7 Projected network enhancement

The losses of single mode fibres at 422 nm (SM400) and 1550 nm (SMF-28) are $\leq 50\,\mathrm{dB\,km^{-1}}$ and $\leq 0.18\,\mathrm{dB\,km^{-1}}$, respectively. Let us consider the end-to-end efficiency of three scenarios in which entanglement is established between remote fibre-connected processing nodes of a quantum network.

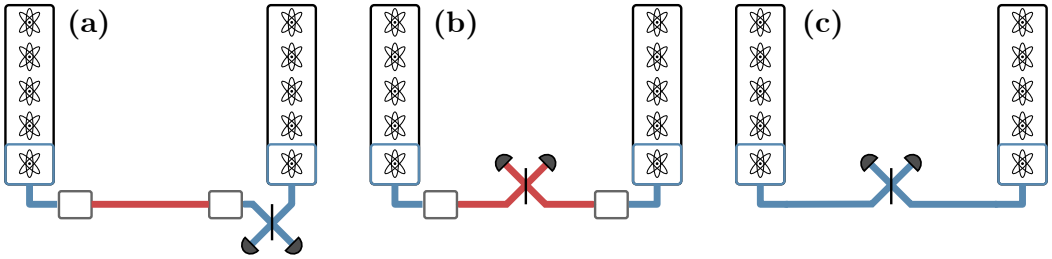

Figure 2.20 Three schemes in which entanglement is established between remote processing nodes. Schemes (a) and (b) use frequency converters, whereas (c) does not.

The three scenarios in which entanglement is established between remote fibre-connected processor nodes are depicted in Fig. 2.20. In case (a), violet photons emitted from the first node are down-converted via our interface and transmitted through a length of optical fibre towards the second node, where, upon arrival, they are up-converted and interfered with photons from the second node. In case (b), photons emitted by both ion traps are down-converted and transmitted through optical fibre to a midway position to interfere. In the final case, (c), a frequency converter is not used and violet photons from either, or both nodes, are sent through fibre to a point of entanglement at a beam splitter.

Figure 2.21 shows the probability of the photons successfully reaching their destination under each of the entanglement schemes outlined, assuming no fibre-coupling losses. It is possible to see that the implementations which make use of our frequency conversion interface will drastically increase the probability of successful end-to-end transmission for remote nodes linked by single mode fibre, even for intracity-scale distances of just a few

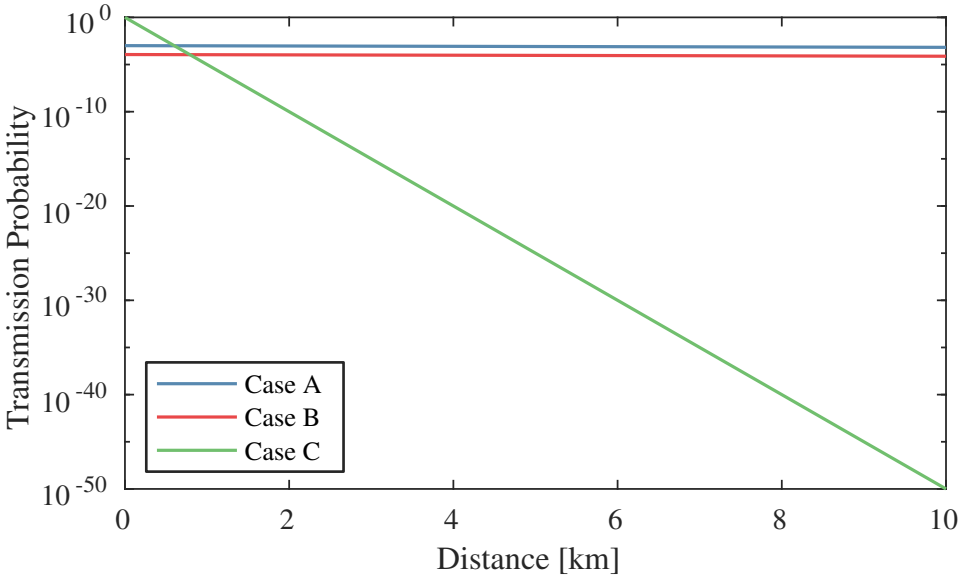

Figure 2.21 Probability of successful transmission of two photons from remote trapped Sr+ ion processing nodes to an entangler along an optical fibre network with and without our interface.

kilometres. We note also that, due to pump power limitations in the current measurements, as well as the expectation that the DFG process efficiency should mirror that of the SFG, the transmission probabilities shown for cases A and B should only increase.

2.3 Summary and outlook

In the development of hybrid light-matter quantum networks, frequency converters are essential to the development of photonic interconnects between nodes operating in the blue and UV wavelengths. The demands of these networks are severe: low-noise conversion to allow for efficient distribution of entanglement and high-visibility two-photon coalescence, state preserving translation across large frequency separations, and high efficiency conversion in both up- and down-conversion. We have implemented a frequency conversion interface capable of low-noise up- and down-conversion of single-photon-level light between a Sr^+ emission wavelength and the telecommunication C band. The stringent phase-matching requirements

were overcome using a bespoke custom-poled MgO:PPLN crystal, which enabled the input to be spectrally remapped in a single stage. Our device has so far been shown to operate with conversion efficiencies of 9.4% and 1.1%, respectively, with potential routes identified to secure increased performance. Even at present, when considering the transmission loss of a single-mode fibre at the Sr^+ emission wavelength of 422 nm relative to that at 1550 nm, our interface would increase the probability of establishing entanglement between remote ion traps by 47 orders of magnitude over a distance of 10 km.

It is probable however, that future work may be able to achieve even greater performance in bridging the blue ion-transition wavelengths and the telecommunication bands. One immediate avenue to explore is in applying newly-developed short-domain-poling capabilities, applied here to a bulk $LiNbO_3$ crystal, to a $LiNbO_3$ waveguide. While the waveguide-induced modification to the dispersion at each wavelength is such that an even shorter pitch may be required, the poling would still be possible using the technique outlined in Section 2.2.1. By making use of a waveguide it could be expected a significant improvement to the reported conversion efficiency will be achieved, owing to a greater confinement of the light and hence a greater nonlinear response. It is also possible, although some effort will be required, to ensure that all of the fields are confined to the fundamental mode of a waveguide, achieving a greater degree of spatial overlap than that which is presently recorded. With such changes it becomes possible to consider the use of a cavity-enhanced CW pump which will be better far better suited to match the emission bandwidth of photons from an ion trap processor.

Chapter 3

Third-Order Nonlinear Frequency Conversion: Design and Simulation

In this chapter frequency conversion is examined by use of the third-order nonlinear susceptibility. Section 3.1 contains details of the theory relevant to $\chi^{(3)}$ nonlinear optics and the design and use of optical fibres. A resource-efficient frequency conversion scheme between the Sr^+ transition at 1092 nm and the telecommunication C band is is presented in Section 3.2. Finally, in Section 3.3, numerical simulations are used to provide insights in to the conversion process of Bragg-scattering four-wave mixing.

3.1 $\chi^{(3)}$ nonlinear fibre optics

As is discussed in Section 2.1, the differences in the crystalline structures of optical materials make it important to consider the nature of the non-linear response of a medium. When we

consider nonlinearities present in optical fibres we must refer to the structure of the silica glass from which they are composed; silica is a centrosymmetric medium and as a result nonlinear effects associated with the even orders of the susceptibility are not supported. Consequentially, the third-order component, $\chi^{(3)}$, is the dominant term. Here, following Ref. [87], we start by looking at the individual cartesian components of the third-order polarisation, $\mathbf{P}^{(3)}$, which was first introduced in Eq. 2.5:

$$P_i^{(3)} = \epsilon_0 \sum_{j,k,l} \chi_{ijkl}^{(3)} E_j E_k E_l. \tag{3.1}$$

The third-order susceptibility, $\chi_{ijkl}^{(3)}$, is a rank 4 tensor, which makes a full expansion of $\mathbf{P}^{(3)}$ a laborious exercise. Fortunately, the isotropy of silica will ensure that the third-order susceptibility is invariant between orthogonal axes:

$$\chi_{xxxx}^{(3)} = \chi_{yyyy}^{(3)} = \chi_{zzzz}^{(3)}. \tag{3.2}$$

In addition, we only consider the case where all optical fields are co-polarised, and the fields that are incident take the form

$$\mathbf{E}(t,z) = \frac{1}{2}\hat{x} \sum_{n=1}^{3} E_n \exp i\big[\omega_n t - k(\omega_n) z\big] + c.c.\,. \tag{3.3}$$

This allows us to treat $\chi^{(3)}$ as a scalar term, which in turn permits a reduced expansion of Eq. 3.1. Similarly to as with the electric field, the different frequency components of the third-order polarisation, which result from taking this reduced expansion, may be written as

$$\mathbf{P}^{(3)}(t,z) = \frac{1}{2}\hat{x} \sum_{n=1}^{4} P_n^{(3)} \exp i\big[\omega_n t - k(\omega_n) z\big] + c.c.\,. \tag{3.4}$$

We can now interrogate the $n = 4$ component of Eq. 3.4, which will appear as a result of the reduced expansion of Eq. 3.1. The following expression describes the component of

the polarisation response at the frequency ω_4, denoted $P_4^{(3)}$, which includes, among others, terms relating to the generation of a new field at frequency ω_4 as a result of parametric mixing between input fields with frequencies ω_1, ω_2 and ω_3:

$$\begin{aligned} P_4^{(3)}(t,z) = \frac{3}{4}\epsilon_0\chi^{(3)}_{xxxx}\Big[& \underbrace{|E_4|^2E_4}_{\text{SPM}} + \underbrace{2(|E_1|^2+|E_2|^2+|E_3|^2)E_4}_{\text{XPM}} \\ & + \underbrace{2E_1E_2E_3\exp i(\Delta\omega_+ t - \Delta k_+ z)}_{\text{FWM}} \\ & + \underbrace{2E_1E_2E_3^*\exp i(\Delta\omega_- t - \Delta k_- z)}_{\text{FWM}} + ...\Big]. \end{aligned} \tag{3.5}$$

The first two terms relate to self-phase modulation (SPM) and cross-phase modulation (XPM); an expanded discussion of these two effects is given in Section 3.1.4. All the remaining terms shown relate to parametric mixing between all four fields. The frequency- and phase-mismatch arguments, $\Delta\omega_\pm$ and $\Delta k_\pm$, for the included mixing terms are given by:

$$\Delta\omega_\pm = \omega_1 + \omega_2 \pm \omega_3 - \omega_4; \tag{3.6}$$

$$\Delta k_\pm = k(\omega_1) + k(\omega_2) \pm k(\omega_3) - k(\omega_4). \tag{3.7}$$

Energy conservation and phase-matching criteria require that both of these terms are zero in order for efficient generation of the fourth field at $\omega_4 = \omega_1 + \omega_2 - \omega_3$ to occur. Both of the parametric mixing processes described are examples of four-wave mixing (FWM), a process which we will consider in detail in the following section. However, it is worth noting that the sort of process described by the first of these terms, corresponding the transfer of energy from three photons to a fourth, has phase matching conditions which are generally intractable to satisfy in the fundamental mode of an optical fibre.

3.1.1 Four-wave mixing

Four-wave mixing is inherently a nonlinear interaction which allows for a diverse range frequency-mixing processes to occur, depending on which input fields are present. A number of conventions exist when referring to different forms of FWM interactions, which we will briefly review here. Figure 3.1 illustrates four examples of FWM processes which are distinguished from each other through naming conventions. The first, non-degenerate FWM, is pumped at two distinct frequencies, ω_{p} and ω_{q}, generating two fields termed signal at the higher frequency, ω_{s}, and idler at the lower, ω_{i}. If both the signal and idler spectral modes are initially in the vacuum state, then the process is seeded by vacuum fluctuations, similar to SPDC. Phase conjugation is similar to non-degenerate FWM in that two spectrally distinct pumps generate signal and idler fields, but in this case the daughter fields are produced at frequencies enclosed by ω_{p} and ω_{q}. The origin of the name phase conjugation comes from the idler and signal terms being coupled to the conjugate of one another. De-

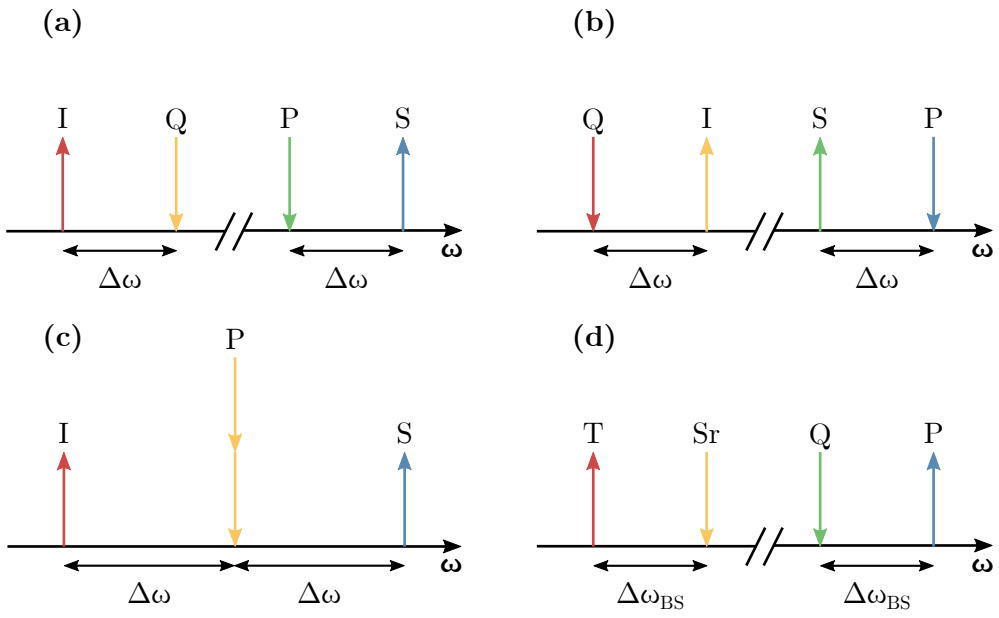

Figure 3.1 Common FWM schemes: (a) Non-degenerate FWM, (b) phase conjugation FWM, (c) degenerate FWM, and (d) Bragg-scattering FWM.

generate FWM is perhaps the most commonly addressed form, as only a single-frequency pump is necessary to generate sidebands; it is used to generate coherent light far from convenient laser transitions and as the basis for wavelength-tunable optical parametric amplifiers (OPAs)[88–90]. When implemented in dispersion-engineered fibres the spontaneous FWM process enables a higher degree of control over the photon states produced than when using SPDC in nonlinear crystals; degenerate-FWM single photon sources are of increasing interest[91–93]. Finally, Bragg-scattering FWM (BS-FWM) enables the frequency difference between two pumps, $\Delta\omega_{\mathrm{BS}} = \omega_{\mathrm{p}} - \omega_{\mathrm{q}}$, to be mapped on to an input photon, enabling the coherent shifting of photons between source (Sr) and target (T) wavelengths. As with SFG and DFG, BS-FWM is a parametric process where the medium does not absorb energy or provide net gain. As a consequence, the final quantum state of the medium is identical to that of the initial state, which is a key requirement for QFC. The name in this instance derives from the presence of intensity-induced index gratings, as viewed by the input photon, which result from the beating of the spectrally-distinct pump fields[94].

In this chapter both degenerate FWM and BS-FWM are used in the development of a frequency conversion scheme to map photons between 1092 nm and 1550 nm. We will engineer each process using dispersion engineering of micro-structured optical fibres.

3.1.2 Light propagation in optical fibres

Conventional optical fibres are cylindrical waveguides, consisting of two silica regions: a higher index core encased by a lower refractive index cladding. Light is confined to the higher-index core, guided in the transverse modes supported by a given geometry. Unless perturbed, each mode propagates without change in group velocity, spatial distribution or polarisation, but will accrue additional phase.

The frequency-dependant propagation constant, $\beta(\omega)$, associated with each mode is anal-

ogous to the component of the wave vector, k, along the direction of propagation:

$$\beta(\omega) = \frac{n_{\text{eff}}(\omega)\,\omega}{c}. \tag{3.8}$$

The value of the effective index, n_{eff}, will fall between that of the higher-index core, n_2, and the cladding that surrounds it, n_1. Fields with multiple spectral components, e.g. from laser beams containing trains of short pulses, are affected by the dispersive nature of fibres. Even below the intensity threshold at which nonlinear effects are important, dispersion-induced pulse broadening will occur. As we have discussed already in Chapter 2 and Section 3.1.1, the balanced combination of optical dispersion and nonlinearity results in remarkably different effects.

The frequency-dependant effects of dispersion may be expressed mathematically as a Taylor expansion about some central frequency, ω_0:

$$\beta(\omega) = \beta_0 + \beta_1(\omega - \omega_0) + \frac{1}{2}\beta_2(\omega - \omega_0)^2 + \dots, \tag{3.9}$$

where,

$$\beta_m = \left.\frac{\mathrm{d}^m\beta}{\mathrm{d}\omega^m}\right|_{\omega_0} \qquad (m = 0, 1, 2, 3, \dots). \tag{3.10}$$

From these expanded terms we obtain a number of useful terms, such as the group velocity, v_{g}, which defines the speed at which the envelope of an optical pulse propagates along the fibre, and the group velocity dispersion (GVD), β_2, which describes the pulse broadening. The group velocity is related to β_1 through the expression

$$\beta_1 = \frac{n_{\text{g}}}{c} = \frac{1}{v_{\text{g}}}, \tag{3.11}$$

where n_{g} is the group index. The dispersion parameter D, often used in place of β_2 to

describe GVD, is given by

$$D = \frac{\mathrm{d}\beta_1}{\mathrm{d}\lambda} = -\frac{2\pi c}{\lambda^2}\beta_2, \tag{3.12}$$

and is typically given with the units $\mathrm{ps\,km^{-1}\,nm^{-1}}$, meaning values given describe the picoseconds of broadening per nanometer wavelength change arising from a kilometre of propagation. For wavelengths where D is negative the fibre exhibits *normal* dispersion, i.e. higher-frequency components of a pulse travel slower than lower-frequency components. Conversely, for wavelengths with positive D a fibre exhibits *anomalous* dispersion and blue-shifted components of a pulse will propagate faster than the red-shifted components. The wavelength at which $D = 0$ is known as the zero-dispersion wavelength (ZDW).

3.1.3 Engineered phase matching in optical fibres

It is useful to describe the propagation constant of a single-mode fibre as being composed of distinct terms relating to contributions from the core material, waveguide geometry and modifications due to nonlinear effects:

$$\beta = \beta_{\mathrm{Material}} + \beta_{\mathrm{Waveguide}} + \beta_{\mathrm{Nonlinear}}\,. \tag{3.13}$$

It is evident then, when using exclusively silica-based fibres, the most convenient mechanism of control over the fibre dispersion, and hence phase matching, should come from modifying the waveguide contribution. In typical step-index optical fibres, such as the one depicted in Fig. 3.2(a), this requires either modifying the dopant, and in turn refractive index contrast between the cladding and the core, or adjusting the core diameter, $\mathrm{d_{core}}$. Photonic-crystal fibres (PCFs) have a lattice of air holes, each permeating the entire fibre length, which forms the cladding structure and a silica core 'defect' at the centre of this lattice. An example PCF geometry is shown in Fig. 3.2(b); varying the diameter of the air holes, d, and the pitch the lattice, Λ, in which they are arranged allows for a high degree of control over the

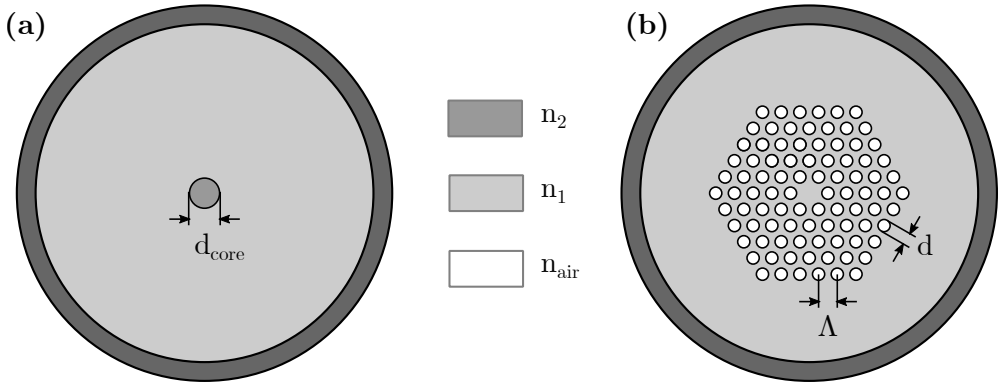

Figure 3.2 (a) Step-index and (b) photonic-crystal fibre structures.

effective index of the cladding and the core size. Consequently, the systematic engineering of the waveguide contribution to fibre dispersion is far easier to achieve in PCFs than in any other fibre platform.

3.1.4 Spurious nonlinear processes in $\chi^{(3)}$ materials.

In Eq. 3.13 we have already drawn explicit attention to the nonlinear component of the propagation constant. Many $\chi^{(3)}$ nonlinear effects which arise as a consequence of this modified refraction can be understood by first considering an expression for the refractive index in the form

$$\tilde{n}(\omega, |E|^2) = n_0 + \tilde{n}_{\mathrm{NL}}|E|^2 = n_0 + n_{\mathrm{NL}}I. \tag{3.14}$$

Here the first term, n_0, is the linear component of the refractive index, while the second term describes the intensity-dependant nonlinear contribution. The intensity dependence is either incorporated directly, or using $|E|^2$, which is linearly related to the field intensity:

$$I = \frac{1}{2}\epsilon_0 \, c \, n_0 \, |E|^2. \tag{3.15}$$

Note that the nonlinear refractive indices, n_{NL} and $\tilde{n}_{\mathrm{NL}}$, are not equivalent, but relate the change in refractive index due to the intensity and the modulus of the electric field squared, respectively. The nonlinear refractive index, $\tilde{n}_{\mathrm{NL}}$, is related to $\chi^{(3)}$ by [87]:

$$\tilde{n}_{\mathrm{NL}} = \frac{3}{8n_0}\mathrm{Re}(\chi^{(3)}_{xxxx}). \tag{3.16}$$

The existence of the nonlinear refractive index leads to a phase modulations of input fields, which we can reveal by considering the phase accrued by a high-intensity travelling wave propagating along z:

$$\phi(t) = \omega_0 t - kz = \omega_0 t - \frac{2\pi(n_0 + \tilde{n}_{\mathrm{NL}}|E|^2)z}{\lambda} = \omega_0 t - \frac{2\pi(n_0 + n_{\mathrm{NL}}I)z}{\lambda}. \tag{3.17}$$

Equation 3.17 shows that a travelling wave of sufficient intensity will induce a phase shift on itself. The phenomenon described is self-phase modulation, which was first referenced in Section 3.1. SPM results in the spectral broadening of a light pulse as it traverses the length of a $\chi^{(3)}$ medium such as silica fibre. We can evaluate this spectral broadening by taking the time differential of the phase:

$$\omega(t) = \frac{\mathrm{d}\phi(t)}{\mathrm{d}t} = \omega_0 - \frac{2\pi z}{\lambda}\frac{\mathrm{d}\tilde{n}(I,t)}{\mathrm{d}t}, \tag{3.18}$$

where the intensity, $I \propto |E|^2$, at a given point in the medium will rise and fall as the optical pulse passes. This produces the time-varying refractive index, $\tilde{n}(I,t)$, which we evaluate here for a gaussian pulse:

$$\tilde{n}(I,t) = n_0 + n_{\mathrm{NL}}I_0 \exp\left(-\frac{t^2}{\tau^2}\right), \tag{3.19}$$

where I_0 is the peak intensity, and τ is half of the pulse duration. We combine Eq. 3.18 and Eq. 3.19 to obtain

$$\omega(t) = \omega_0 + \frac{4\pi\, n_{\mathrm{NL}} I_0 z}{\lambda \tau^2} \cdot t \cdot \exp\left(\frac{-t^2}{\tau^2}\right), \tag{3.20}$$

which is plotted in Fig. 3.3. We see that the leading edge of the pulse shifts to lower frequencies and the tail edge shifts to higher frequencies. These additional frequencies produced through SPM will spectrally broaden the pulse symmetrically, with the time envelope of the pulse unaffected, except due to the resulting effects from dispersion.

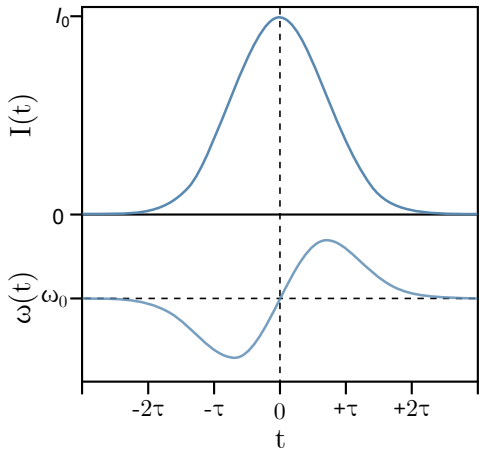

Figure 3.3 The self-frequency shift incurred by an optical pulse due to self-phase modulation.

When multiple optical pulses centred at different frequencies overlap then cross-phase modulation (XPM) may also occur, with the fields inducing phase modulations on each other. SPM and XPM are effects which need only be considered when strong fields with high peak power pulses are present.

While SPM and XPM arise from the real part of $\chi^{(3)}$, the imaginary component also contributes to the phase. So far we have discussed nonlinear effects that are elastic, with no energy from the electromagnetic wave transferred to or from the medium. Effects described by the imaginary component of $\chi^{(3)}$ are inelastic scattering interactions. Raman scattering occurs when photons from the pump field scatter off of the molecules within a dielectric and

excite vibrational states. The photons scattered in this way are left with less energy and are

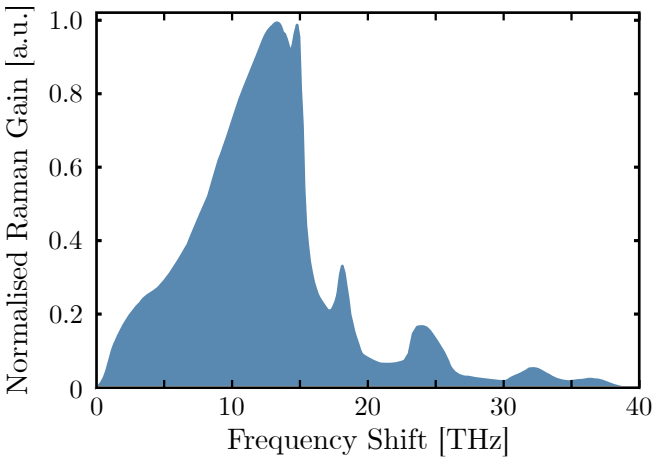

Figure 3.4 Illustration of Raman gain in silica as a function of the frequency offset between the Stokes wave and the pump. The shape of the gain spectra is based on results in Ref. [95].

downshifted to a lower frequency. The down-shifted photons are referred to as the Stokes wave. Up-shifting (anti-Stokes) may also occur as scattered photons absorb energy from a vibrational state of the medium, although this requires the presence of optical phonons and is therefore far less prevalent. The Raman gain in a Stokes wave is exponentially dependant on the existing Stokes intensity, which results in a generated spectrum with a narrow peak at the maximum value of Raman gain, which in silica is at 13.2 THz. The process will begin to cascade as each Raman peak itself undergoes its own Raman shift, leading to spectral noise far from the original pump wavelengths. Raman scattering is a dominating source of noise in both FWM single-photon sources [96] and frequency-conversion schemes [43].

3.2 A resource-efficient FWM scheme

The efficient translation of photons between 1092 nm and the telecommunication C band will allow the Sr^+ $D_{3/2} \rightarrow P_{1/2}$ transition to be reliably linked to disparate and distant nodes of a quantum network. Using a $\chi^{(3)}$ frequency conversion process makes sense here for two reasons: a fully developed fibre-based interface may prove simplest to integrate in to the

network architecture, and the pump wavelength required for the alternative $\chi^{(2)}$ SFG/DFG converter would need to be >3.69 µm to satisfy energy conservation. The flexibility to tailor PCF dispersion and to select any two arbitrary pump wavelengths which satisfy the energy-conservation requirement, i.e. that they are frequency-separated by $\Delta\omega_{\mathrm{BS}} \simeq 510$ THz, means the choice of lasers for a $\chi^{(3)}$ converter will be less heavily constrained. Previous experiments have made use of two independent high-power pulsed lasers, with their repetition rates locked together, in order to excite a nonlinear interaction. However, a quantum network will potentially be comprised of a large number of nodes, between each of which frequency converters will be installed, meaning the use of two distinct pump lasers at each location will be logistically and financially undesirable.

This thesis describes a two-stage FWM frequency converter which requires only a single pulsed laser system to operate, thereby benefitting the scalability of a quantum network in which it is employed. Figure 3.5 shows the protocol we employ; a degenerate FWM

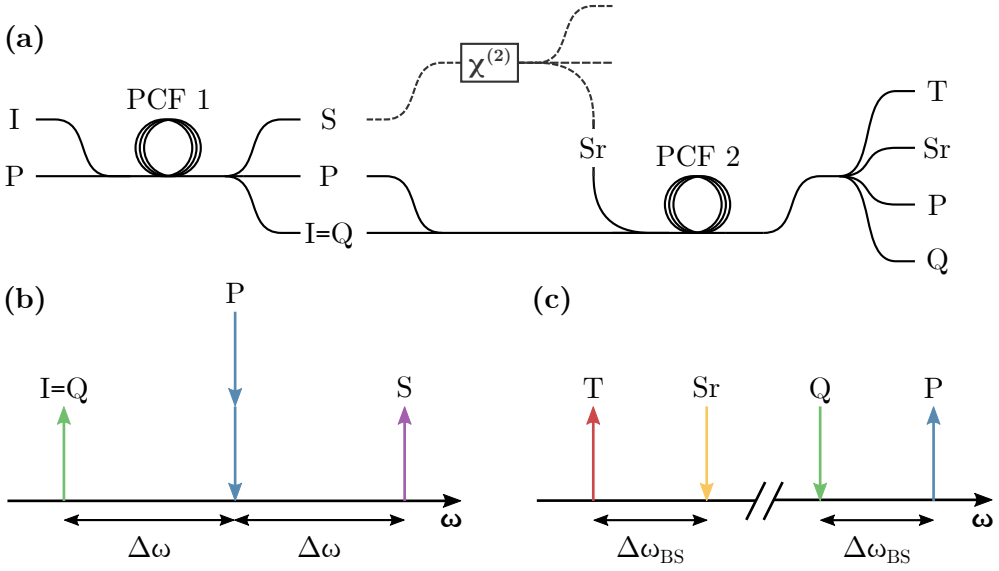

Figure 3.5 (a) A protocol in which a single high-pulse-energy laser drives a BS-FWM frequency converter. An initial FWM interaction (b), in PCF 1 is used to generate a second pump field, Q, which in conjunction with the initial pump field, P, drives the BS-FWM process (c) in PCF 2.

process is engineered in PCF 1, such that the frequency separation between the pump and sidebands, $\Delta\omega$, is equal to that between the source and target fields, $\Delta\omega_{\mathrm{BS}}$, in our desired BS-FWM conversion — the pump and idler from PCF 1 may then be carried forward to pump the conversion in PCF 2. Seeding the FWM process in PCF 1 at either the signal or idler wavelength with the output from a diode laser limits the spectral width of the sidebands and increases the pulse-to-pulse stability, producing sufficiently high quality pulses appropriate for the pumping of BS-FWM. An additional possibility we note, is to use the discarded FWM sideband to pump a PDC single-photon source which may be phase-matched to produce photons at the source wavelength, thereby providing an integrated means to verify the frequency converter's performance. The constraint that is introduced using this scheme is the availability of appropriate diode lasers at a given wavelength considered for the FWM sidebands.

The high-power pulsed laser pump we use is a Ti:Sapphire oscillator (Spectra Tsunami) with an 80-MHz repetition rate and a ∼15-ps pulse duration. Ti:Sapphire lasers are a workhorse piece of equipment in many nonlinear optics labs as a result of their ability to deliver ultrashort pulses with high average powers across a wavelength range from 700 to 1000 nm. The diode laser used to seed our first FWM interaction will define the energy-matching requirements in the BS-FWM process, with the diode laser therefore needing to operate at a wavelength which does not require the high-power pump wavelength to sit outside of the Ti:Sapphire laser tuning range. There is also the need to consider how the wavelength selection is likely to affect the noise levels overlapped with the source and target, as well as the potential risk of spurious FWM processes occurring; the considerations relating to noise and spurious FWM will be expanded upon in Section 3.3. A suitable and widely available diode laser wavelength is ∼980 nm. Therefore, our wavelength conversion scheme is as follows: FWM is PCF 1 is pumped at $\lambda_{\mathrm{P}} = 775$ nm, with signal and idler sidebands at $\lambda_{\mathrm{S}} = 640$ nm and $\lambda_{\mathrm{I}} = 980$ nm. The light at 775 nm and 980 nm (λ_{Q}) is then used to pump the

BS-FWM conversion between 1092 nm (λ_{Sr}) and 1550 nm (λ_{T}). These selections ensure that the diode laser is at a readily available wavelength and that the Ti:Sapphire pump is tuned to a wavelength well within the ideal operating regime. It would be valid also to use the discarded 640 nm signal from the first FWM process, in place of the 980 nm sideband, as a pump for the BS-FWM. Such an arrangement would introduce a larger frequency separation between the pumps and the single-photon-level fields and potentially reduce the noise levels at those wavelengths. However, this thesis presents the configuration which ensures the 640 nm pulsed light remains available for future work in which it will be used to pump a PDC single-photon source with daughter fields at 1092 nm and 1550 nm.

3.3 Numerical modelling of four-wave mixing

3.3.1 Phase matching in photonic crystal fibre

In Section 3.1 we discussed how all fields interacting via FWM are required to maintain a fixed phase relationship, for the process to be efficient. We introduced PCFs as a form of optical waveguide that allow for a high level of control over the dispersion and the resulting phase matching which is possible between different wavelengths. Engineered phase matching in PCFs requires the fibre dispersion to be carefully tailored to the requirements of the desired FWM process. The phase mismatch for the degenerate FWM interaction in optical fibres is given by

$$\Delta\kappa_{\mathrm{FWM}} = \Delta\beta_{\mathrm{FWM}} + 2\gamma P_{\mathrm{P}}, \tag{3.21}$$

where the SPM of the pump is accounted for by the second term, composed of the peak power of the pump, $P_{\mathrm{P}} = |A_{\mathrm{P}}|^2$, and the optical nonlinearity,

$$\gamma = \frac{n_{\mathrm{NL}}(\omega)\omega_{\mathrm{p}}}{cA_{\mathrm{eff}}}. \tag{3.22}$$

The nonlinear refractive index, n_{NL}, and effective mode area A_{eff} govern the strength of this nonlinearity. The mismatch in propagation constant included in Eq. 3.21 is

$$\Delta\beta_{\mathrm{FWM}} = \beta(\omega_{\mathrm{S}}) + \beta(\omega_{\mathrm{I}}) - 2\beta(\omega_{\mathrm{P}}). \tag{3.23}$$

When BS-FWM occurs in a non-birefringent fibre, then the phase mismatch is similarly described as a combination of propagation-constant and nonlinear dispersive mismatch [97]

$$\Delta\kappa_{\mathrm{BS}} = \frac{1}{2}\Delta\beta_{\mathrm{BS}} + \frac{1}{2}\gamma(P_{\mathrm{Q}} - P_{\mathrm{P}}). \tag{3.24}$$

Here, P_{Q} denotes the power of the second pump and the BS-FWM dispersive mismatch term is given by

$$\Delta\beta_{\mathrm{BS}} = \beta(\omega_{\mathrm{T}}) + \beta(\omega_{\mathrm{P}}) - \beta(\omega_{\mathrm{Sr}}) - \beta(\omega_{\mathrm{Q}}). \tag{3.25}$$

In the case of both FWM and BS-FWM the dispersive mismatch is the dominating term which contributes to the overall phase matching in a fibre. We gain additional insight in to the required dispersive properties of our fibres if we expand the dispersive mismatch of both the FWM (Eq. 3.23) and BS-FWM (Eq.3.25) processes around their central frequencies, ω_{A}. As shown in Fig. 3.6(a), the central frequency of degenerate FWM is colocated with the

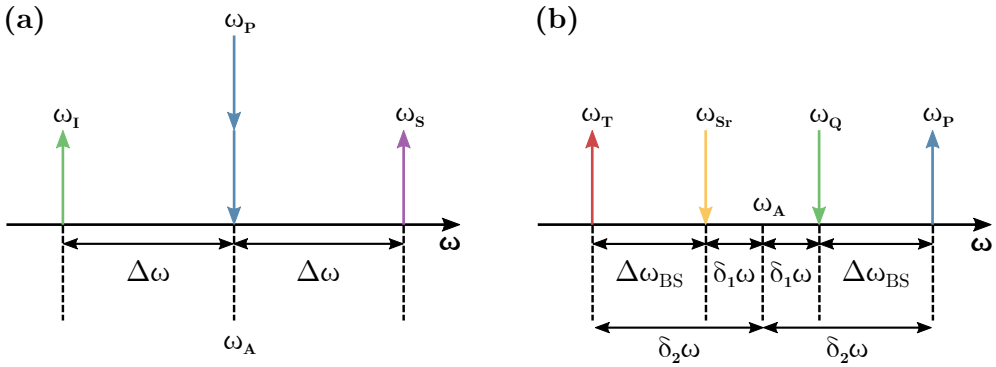

Figure 3.6 The separation of fields from the average frequency, ω_{A}, for (a) degenerate FWM and (b) BS-FWM.

pump frequency, allowing us to express the dispersive mismatch as [98]

$$\Delta\beta_{\mathrm{FWM}} = \sum_{n=1}^{\infty} \frac{\beta_{2n}(\omega_{\mathrm{P}})}{(2n)!}\Delta\omega^{2n}. \tag{3.26}$$

The result of the expansion is a summation of the even orders of β, the terms of which will typically diminish with an increase in the order. If a fibre is pumped in the anomalous regime, where β_2 is negative, the nonlinear term in Eq. 3.23 will act against the dispersive mismatch term; when the dominant β_2 term is small enough sidebands will be generated close in frequency to the pump. Conversely, if the pump wavelength is in the normal dispersion regime, but still close to where $\beta_2 = 0$, the β_4 term will dominate and far larger frequency shifts will occur. PCF 1 must therefore be designed such that the ZDW is slightly larger than specified pump wavelength at 775 nm.

Similarly the BS-FWM dispersive mismatch is given by the expansion [98]

$$\Delta\beta_{\mathrm{BS}} = \sum_{n=1}^{\infty} \frac{\beta_{2n}(\omega_{\mathrm{A}})}{(2n)!}\left(2\delta_1\omega^{2n} - 2\delta_2\omega^{2n}\right). \tag{3.27}$$

The terms of this expansion, $\delta_1\omega$ and $\delta_2\omega$, are the distance from the average frequency of the inner and outer two fields, respectively — these are schematically shown in Fig. 3.6. Similar to the degenerate FWM, the BS-FWM phase matching can be obtained for widely spaced wavelengths when the central frequency is close to the ZDW of the fibre and in the normal-dispersion regime.

The relationship between a PCF's dispersion and the pitch and air hole diameter in the cladding structure is well understood. In 2005, Saitoh and Koshiba presented empirical relations which allow for the quick design of PCFs [99]: decreasing the pitch results in the zero-dispersion wavelength being shifted to shorter wavelengths; reducing the hole size will move the dispersion profile further into the normal dispersion regime. Through iterated small changes we converge on dispersion profiles for PCF 1 and 2, that satisfy the outlined

phase-matching requirements.

We further simulate PCF structures using COMSOL Multiphysics[1], a commercially-available finite element solver. The fibre geometry is divided in to a mesh as depicted in Fig. 3.7, with the symmetry of PCFs allowing for just a single quadrant of each fibre to be modelled. This reduced geometry serves to minimise the computational resources

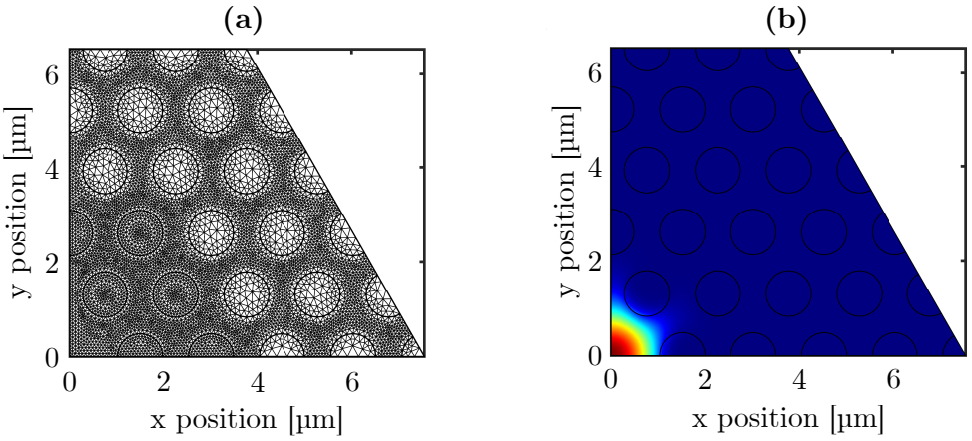

Figure 3.7 (a) The fine meshing used for finite element analysis as applied to the cladding structure of a PCF. (b) A simulated electric field profile of the fundamental mode.

used and allows for the output to be decomposed in to linearly polarised modes. The mesh size is programmed to be smaller around the core, where we expect the majority of electric field to be confined. The software evaluates the electric field at each point in the mesh to find solutions for the total electric field distribution in the structure which satisfy Maxwell's equations. The x=0 boundary is set as a perfect magnetic conductor, constraining solutions to distributions where the magnetic field component parallel to this edge is zero; the remaining boundaries are set as perfect electric conductors, leaving only the vertically polarised modes supported in the simulated structure. We execute a parametric sweep of wavelength and evaluate β at each step, using the obtained values to produce phase-matching contours for the appropriate FWM processes. The simulated dispersion and phase-matching

[1]https://www.comsol.com

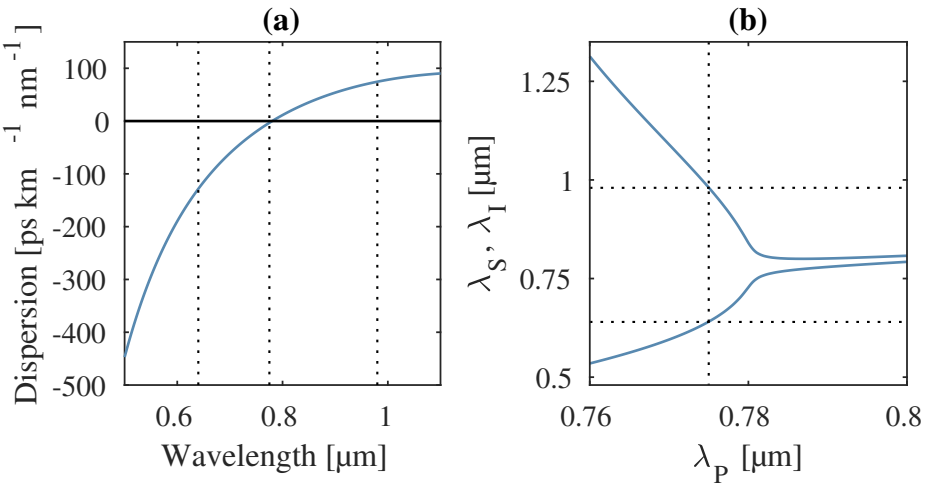

Figure 3.8 Simulated (a) group-velocity dispersion and (b) phase-matching contour at $\Delta\kappa_{\mathrm{FWM}} = 0$ of PCF 1 with a 1.508-µm pitch and a hole-to-pitch ratio of 0.637. The dotted lines correspond to the Pump, Signal and Idler wavelengths.

contours for the first fibre, designed for the seeded FWM process, are shown in Fig. 3.8. The PCF has a 1.508-µm pitch and a hole-to-pitch ratio of 0.637, which produces a ZDW at 780 nm. The simulated results for the second fibre, engineered to facilitate the BS-FWM process, are shown in Fig. 3.9. PCF 2 has a 3.480-µm pitch and a hole-to-pitch ratio of 0.450. The ZDW of PCF 2 is at 1063 nm.

PCFs may be designed to support only a single mode [100], but this is not a universal property to all PCF structures. By allowing COMSOL to solve for additional electric-field distributions and assessing their spatial profiles we are able to verify that both PCF designs are single mode in operation across the wavelength range of interest.

Both fibres were also designed to have broadband phase matching so to increase the permitted fabrication tolerance; neither fibre is designed for a spontaneous FWM process where daughter fields grow from quantum noise, but instead the specific wavelengths are stimulated through our choice of source or seed fields. In essence, this means that there is no specific reason to impose narrow phase matching for either process. For the degenerate seeded FWM, the injected seed laser will ensure the sidebands are narrow and for the BS-

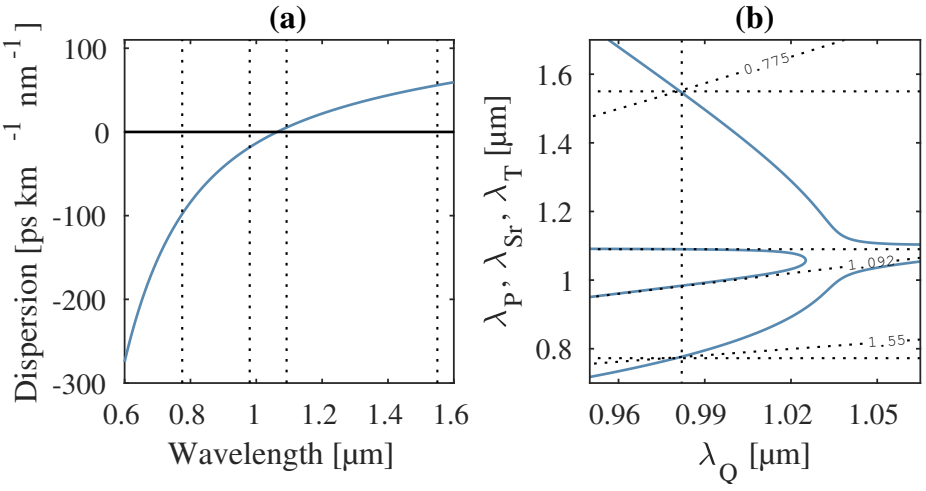

Figure 3.9 Simulated (a) group-velocity dispersion and (b) phase matching contour at at $\Delta\kappa_{\mathrm{BS}} = 0$ of PCF 2 with a 3.480-μm pitch and a hole-to-pitch ratio of 0.450. The value of λ_{Sr} is fixed at 1092 nm. The dotted lines correspond to the two pumps, Source and Target wavelengths. For the phase matching shown in (b), the dotted horizontal lines read off from the y axis, the vertical lines read from the x axis and the diagonal lines indicate contours of a frequency mesh in x and y, which satisfy the energy conservation criterion.

FWM the spectral shifting of the input will be constrained by energy matching. Engineering broadband phase matching allows for some additional fabrication tolerance without affecting the output from either FWM process.

We can see this broad phase matching by looking at the joint spectra for the two processes. Similarly to the approach used for $\chi^{(2)}$ processes in Chapter 2, we can write the JSA for degenerate FWM as

$$f(\omega_{\mathrm{i}}, \omega_{\mathrm{s}}) = \alpha_{\mathrm{FWM}}(\omega_{\mathrm{i}} + \omega_{\mathrm{s}})\Phi_{\mathrm{FWM}}(\omega_{\mathrm{i}}, \omega_{\mathrm{s}}), \tag{3.28}$$

where the PEF and PMF are[101]

$$\alpha_{\mathrm{FWM}}(\omega_{\mathrm{i}} + \omega_{\mathrm{s}}) = \exp\Big(- \frac{[\,(\omega_{\mathrm{i}} - \omega_{\mathrm{i},0}) + (\omega_{\mathrm{s}} - \omega_{\mathrm{s},0})\,]^2}{4\sigma_{\mathrm{p}}^2}\Big), \tag{3.29}$$

and

$$\Phi_{\mathrm{FWM}} = \mathrm{sinc}\left(\frac{\Delta\kappa_{\mathrm{FWM}}L}{2}\right)\exp\left(i\frac{\Delta\kappa_{\mathrm{FWM}}L}{2}\right). \tag{3.30}$$

The joint spectra of BS-FWM processes are not easily constructed when CW pumps are not employed as there is no analytical means to account for the pulse shapes and the relative walk off between the four fields. We can however evaluate the PMF and assume monochromatic pumps to impose a trace along the energy-matched contour. The reduced phase-matching function is [102]

$$\Phi_{\mathrm{BS,CW}} = \left|\mathrm{sinc}\left(\frac{\Delta\kappa_{\mathrm{FWM}}L}{2}\right)\right|^2. \tag{3.31}$$

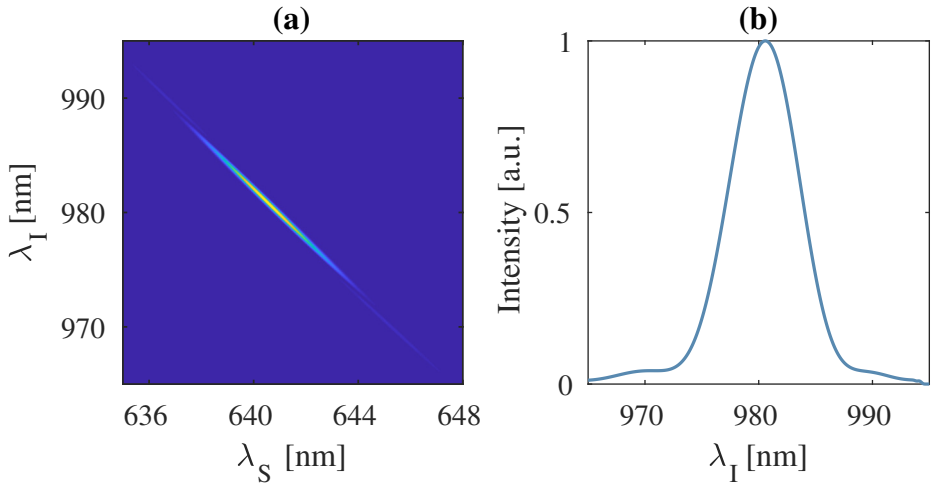

Figure 3.10 (a) The JSI for 45-cm length of PCF 1, pumped at 775 nm; the intensity spans between zero (blue) and one (yellow). (b) The spectrum at the idler wavelength, obtained by projecting the JSI on the λ_{I} axis.

In Fig. 3.10 we show the numerically-simulated JSI produced by optically pumping a 45-cm length of PCF 1 with a laser wavelength-tuned to 775 nm and operating at a pulse duration of 5 ps. The marginal distribution at the idler is also plotted and shows that the sideband produced at 980 nm has a FWHM bandwidth of 7 nm. This is sufficiently broad that fabricating a PCF of a similar geometry within standard fabrication tolerances will at least partially overlap this phase-matched region with seed laser wavelength. Figure 3.11 depicts the PMF, $\Phi_{\mathrm{BS,CW}}$, which is plotted across the entire spectral range of interest for

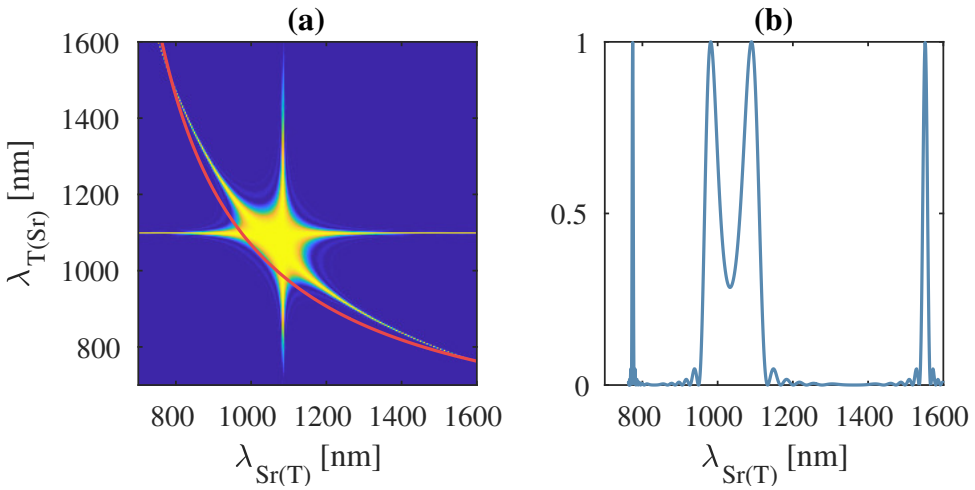

Figure 3.11 (a) The phase matching function for a 20-cm length of PCF 2 with fixed pump wavelengths at 775 nm and 980 nm; the intensity spans between zero (blue) and one (yellow). The energy conservation delta function is plotted in red. (b) The spectrum obtained by taking a trace along the energy conservation delta function.

a 20-cm length of PCF 2. The energy-matched contour is overlaid in red, and is calculated for fixed-wavelength monochromatic pumps at 775 nm and 980 nm. A trace along this contour is also plotted, which produces a four-peaked singles spectrum. The two short-wavelength peaks correspond to the trivial case where source and target wavelengths overlap with the two pump wavelengths and process is self phase matched. The two long-wavelength peaks correspond to the non-trivial solutions where the source(target) wavelength is either 1092 nm(1550 nm) or 1550 nm(1092 nm). The bandwidths of the phase-matched regions at these wavelengths are 13 nm at 1550 nm and 40 nm at 1092 nm. We note that in the experimental case these bandwidths will be enlarged by the use of finite-bandwidth pumps, though similarly will be reduced by the use of longer lengths of fibre; the equivalent bandwidths to those listed above, but for a 1-m length of fibre are 1.6 nm and 5.6 nm at 1550 nm and 1092 nm, respectively.

3.3.2 Pulse evolution study of Bragg-scattering four-wave mixing

The necessary calculations required to ensure particular PCF designs facilitate the desired FWM processes were presented in Section 3.3.1. However, the phase-matching considerations are but one factor governing the BS-FWM interaction. Following the simplified quantum mechanical description set out by McKinstrie *et al.*, the Hamiltonian of the BS-FWM process is

$$\mathcal{H} = \delta\left(\hat{a}_{\mathrm{Sr}}^{\dagger}\hat{a}_{\mathrm{Sr}} - \hat{a}_{\mathrm{T}}^{\dagger}\hat{a}_{\mathrm{T}}\right) + \rho\hat{a}_{\mathrm{Sr}}^{\dagger}\hat{a}_{\mathrm{T}} + \rho^{*}\hat{a}_{\mathrm{Sr}}\hat{a}_{\mathrm{T}}^{\dagger}, \tag{3.32}$$

where δ and ρ are parameters that describe the phase-mismatch and nonlinearity-induced coupling[97]. The evolution is given by the spatial Heisenberg equations of motion

$$\frac{\mathrm{d}}{\mathrm{d}z}\hat{a}_{\mathrm{Sr}} = i\left[\hat{a}_{\mathrm{Sr}}, \mathcal{H}\right], \tag{3.33}$$

$$\frac{\mathrm{d}}{\mathrm{d}z}\hat{a}_{\mathrm{T}} = i\left[\hat{a}_{\mathrm{T}}, \mathcal{H}\right]. \tag{3.34}$$

The creation and annihilation operators satisfy the commutation relations $[\hat{a}_j, \hat{a}_k] = 0$ and $[\hat{a}_j, \hat{a}_k^{\dagger}] = \delta_{jk}$, where j and k are the source or target, and δ_{jk} is the Kronecker delta. Substituting Eq. 3.32 in to these equations of motion, we obtain

$$\frac{\mathrm{d}}{\mathrm{d}z}\hat{a}_{\mathrm{Sr}} = i\delta\hat{a}_{\mathrm{Sr}} + i\rho\hat{a}_{\mathrm{T}}, \tag{3.35}$$

$$\frac{\mathrm{d}}{\mathrm{d}z}\hat{a}_{\mathrm{T}} = i\rho^{*}\hat{a}_{\mathrm{Sr}} - i\delta\hat{a}_{\mathrm{T}}. \tag{3.36}$$

When these equations are solved, the solutions take the form

$$\hat{a}_{\mathrm{Sr}}(z) = \bar{\mu}(z)\hat{a}_{\mathrm{Sr}}(0) + \bar{\nu}(z)\hat{a}_{\mathrm{T}}(0), \tag{3.37}$$

$$\hat{a}_{T}(z) = -\bar{\nu}^{*}(z)\hat{a}_{\mathrm{Sr}}(0) + \bar{\mu}^{*}(z)\hat{a}_{\mathrm{T}}(0), \tag{3.38}$$

where the transfer functions are

$$\bar{\mu}(z) = \cos(kz) + i\delta\frac{\sin(kz)}{k}, \tag{3.39}$$

$$\bar{\nu}(z) = i\rho\frac{\sin(kz)}{k}. \tag{3.40}$$

Here, $k = (|\rho|^2 + \delta^2)^{1/2}$, and the the transfer functions satisfy the relation $|\bar{\mu}|^2 + |\bar{\nu}|^2 = 1$, ensuring the conservation of photon number. Let us consider what happens in the case of an input state consisting of a single source photon, $|1,0\rangle_{\rm in} = \hat{a}^\dagger_{\rm Sr}|0,0\rangle_{\rm in}$, where $|n_{\rm Sr}, n_{\rm T}\rangle$ describes the numbers of photons in the Source and Target modes. We can use the inverse of Eq. 3.37 and express the input operator as

$$|1,0\rangle_{\rm in} = \bar{\mu}|1,0\rangle_{\rm out} - \bar{\nu}^*|0,1\rangle_{\rm out}. \tag{3.41}$$

When $|\bar{\nu}| = 1$ the output state is a perfectly converted replica of the input state. However, in general the length of the fibre may not be such that the the sinusoidally varying transfer functions (Eq. 3.39 and Eq. 3.40) map a perfect conversion of the input. The above analysis is valid also only for CW input and pump fields, whereas the more realistic scenario, when all the fields are pulsed and contain multiple frequencies, is more complicated. In this case each source mode will correspond to many target modes, with the inverse also true. It is possible to represent the transformation over all frequencies using Greens functions [103,104], although such treatments are not possible to solve analytically.

To investigate the response of the BS-FWM interaction to pulse shapes and dispersive effects it is necessary to use numerical methods to compute any well defined input state to a determined output state. The evolution of a field propagating through a dispersive medium is described by the non-linear Schroödinger equation (NLSE). A commonly applied technique for solving the NLSE, the split-step Fourier (SSF) method, may be understood

by taking the simplified form

$$\frac{\partial}{\partial z}A = (\hat{D} + \hat{N})A. \tag{3.42}$$

where the $\hat{D}$ and $\hat{N}$ are differential operators that account for dispersive and nonlinear effects in the optical fibre, and A is the slowly varying pulse envelope. While in reality the optical nonlinearity and dispersion act on evolving fields concurrently, it is possible to make an assumption that over very short distances the two terms may be applied separately [87,105]. By using this assumption, the SSF method evolves fields along a fibre divided in to an integer number of segments of length Δz, according to

$$A(z + \Delta z, T) \approx \exp(\Delta z \hat{D}) \exp(\Delta z \hat{N}) A(z, T). \tag{3.43}$$

The nonlinearity and dispersion are applied in time and frequency domain respectively, with a Fourier transform applied to the field between each step. This algorithm is the simplest implementation of the SSF method, but an improved symmetric-SSF algorithm has been shown to increase the accuracy from $\mathcal{O}(\Delta z^2)$ to $\mathcal{O}(\Delta z^3)$ [106]. The evolution of a field obtained through the symmetric-SSF technique is

$$A(L, T) = \exp\left(-\frac{\Delta z}{2}\hat{N}\right)\left[\prod_{m=1}^{M} \exp(\Delta z \hat{N}) \exp(\Delta z \hat{D})\right] \exp\left(\frac{\Delta z}{2}\hat{N}\right) A(0, T). \tag{3.44}$$

The exponential operator $\exp(\Delta z \hat{D})$ is evaluated in the Fourier domain according to

$$\exp(\Delta z \hat{D}) A(z, T) = \mathcal{F}^{-1}\{ \exp(\Delta z \hat{L}) \mathcal{F}[A(z, T)] \}, \tag{3.45}$$

where $\mathcal{F}$ is the Fourier transform and $\hat{L}$ is the dispersion operator in the frequency domain. Solving Eq. 3.44 for pulses which are both closely spaced in time and frequency necessitates only a single frequency array, which has an associated time array also. However, implementing the SSF method for pulses which are remote in either time or frequency is intractable. To

solve this problem, we create a separate time-frequency window for each of the four fields, which facilitates the computation of the frequency amplitudes around the fields, but not for the intervals between fields. Under this assumption, the total electric field is given by

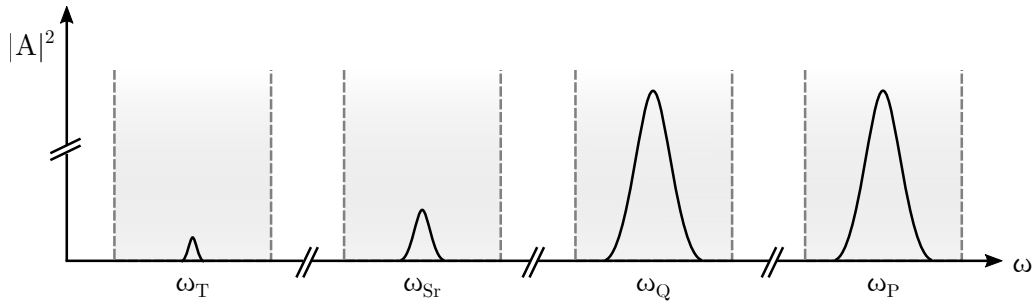

Figure 3.12 Each field envelope evolved under the symmetric-SSF technique has a frequency window which is isolated and remote from the other windows. These fields interact through the coupled equations 3.47 to 3.50.

the sum of these four fields, which are each expressed in terms of their invariant transverse electric field profile, $F_j(x,y)$, and slowly varying pulse envelope, $A_j(z,t)$:

$$\mathbf{E}(\mathbf{r},t) = \frac{1}{2}\hat{x}\sum_j F_j(x,y)A_j(z,t)\exp i\big[\omega_j t - \beta(\omega_j)z\big] + c.c., \tag{3.46}$$

where the index j denotes the fields P, Q, Sr and T. These four fields are evolved concurrently, interacting through the nonlinear terms of the coupled equations

$$\frac{\partial}{\partial z}A_{\mathrm{Q}} = i\beta(\omega_{\mathrm{Q}})A_{\mathrm{Q}} + i\gamma\left[\left(|A_{\mathrm{Q}}|^2 + 2\sum_{j\neq \mathrm{Q}}|A_j|^2\right)A_{\mathrm{Q}} + 2A_{\mathrm{Sr}}^* A_{\mathrm{P}} A_{\mathrm{T}} e^{i\Delta\beta z}\right], \tag{3.47}$$

$$\frac{\partial}{\partial z}A_{\mathrm{Sr}} = i\beta(\omega_{\mathrm{Sr}})A_{\mathrm{Sr}} + i\gamma\left[\left(|A_{\mathrm{Sr}}|^2 + 2\sum_{j\neq \mathrm{Sr}}|A_j|^2\right)A_{\mathrm{Sr}} + 2A_{\mathrm{Q}}^* A_{\mathrm{P}} A_{\mathrm{T}} e^{i\Delta\beta z}\right], \tag{3.48}$$

$$\frac{\partial}{\partial z}A_{\mathrm{P}} = i\beta(\omega_{\mathrm{P}})A_{\mathrm{P}} + i\gamma\left[\left(|A_{\mathrm{P}}|^2 + 2\sum_{j\neq \mathrm{P}}|A_j|^2\right)A_{\mathrm{P}} + 2A_{\mathrm{Q}} A_{\mathrm{Sr}} A_{\mathrm{T}}^* e^{-i\Delta\beta z}\right], \tag{3.49}$$

$$\frac{\partial}{\partial z}A_{\mathrm{T}} = \underbrace{i\beta(\omega_{\mathrm{T}})A_{\mathrm{T}}}_{\text{Dispersion}} + i\gamma\left[\left(\underbrace{|A_{\mathrm{T}}|^2}_{\text{SPM}} + \underbrace{2\sum_{j\neq \mathrm{T}}|A_j|^2}_{\text{XPM}}\right)A_{\mathrm{T}} + \underbrace{2A_{\mathrm{Q}} A_{\mathrm{Sr}} A_{\mathrm{P}}^* e^{-i\Delta\beta z}}_{\text{FWM}}\right]. \tag{3.50}$$

The first term on the right hand side of each coupled equation relates to the dispersion

acting on the specified field. The second and third terms are the self- and cross-phase modulation terms. Finally, the last term describes the FWM interaction which governs the power transfer between the four fields. The nonlinear coefficient, γ, is introduced in Eq. 3.22 and the dispersive mismatch, $\Delta\beta$, is obtained from Eq. 3.25.

The coupled equations 3.47 to 3.50 are solved in the reference frame of the pump Q. Introducing this frame of reference means that there need only be a single universal time mesh. The dispersive term relating to the group velocity of pump Q, $\beta_1(\omega_{0,\mathrm{Q}})$, is consequentially subtracted from the propagation of all pulses:

$$\beta(\omega_j) = \sum_{n=1}^{4} \frac{\beta_n\left(\omega_{0,j}\right)\left(i\partial_T\right)^n}{n!} - \beta_1\left(\omega_{0,\mathrm{Q}}\right) i\partial_T, \tag{3.51}$$

where $\omega_{0,j}$ is the centre of the frequency mesh for the respective field j, and the retarded time is $T = t - z\beta_1(\omega_{0,\mathrm{Q}})$. Here, ∂_T represents the the partial derivative with respect to T.

Armed with the equations introduced in the preceding pages, we now summarise the method through which the evolution of the four fields are calculated. The pump and source wavelengths are specified according to the BS-FWM regime introduced in Section 3.2, with the centre of all the frequency windows calculated using the energy conservation requirements. Dispersion meshes are then calculated for each frequency window, using Eq. 3.51. The pump envelopes for each of the four fields are created in the time domain., with the absolute value of amplitude given as either a Gaussian (pulsed) or invariant (CW) function of the retarded time mesh T. The time separation between the centre of each pulse, Δt, is set to be zero, though may be adjusted if a temporal offset is required.

As we attempt to solve the coupled equations it is necessary that we treat both frequency and time domains with equal precision, since one is no less critical than the other. We ensure equal treatment by selecting parameters such that an equal number of mesh points represent the Gaussian time- and frequency-distributions. Transform-limited Gaussian pulses have

standard deviations in time and frequency related by $\sigma_f = \sigma_t^{-1}$. Additionally, the separation in frequency mesh points in a defined windows will be $\Delta f = T^{-1}$. If we wish to assign the same number of mesh points contained within one σ_t in time and one σ_f in frequency centre of each respective mesh, it is necessary to use $N = T^2/\sigma_t^2$ points across both windows.

To begin the propagation a nonlinear half-step is first applied to the time-domain amplitudes; here the phase modulation and four-wave mixing terms act. The fields are then ready to advance the first full step, as is described by Eq. 3.44. The time-domain amplitudes are Fourier transformed into frequency space where a dispersive step is applied to each field by a multiplication with the exponential factor of the associated dispersive mesh. An inverse-Fourier transform returns the fields to the the time domain where a full nonlinear step is applied. This evolutionary procedure of systematically applying nonlinear then dispersive steps is maintained until the fields have propagated the entire length of the fibre. To obtain the final fields a final reverse nonlinear half-step is applied.

We use the (fourth-order) Runge-Kutta (RK) method to solve the ordinary differential equations outlined in the numerical recipe above. Details of the Runge-Kutta technique are available in many numerical-method texts [107,108], although for completeness we provide a brief introduction here.

We are required to solve first-order differential equations which have initial boundary conditions. This straitforward integration problem may be expressed as

$$\frac{\mathrm{d}}{\mathrm{d}z}y = f(z, y), \quad y(z_0) = y_0. \tag{3.52}$$

The numerical approach to solving such a problem necessitates that all the variables be discretised along small steps of Δz, such that $y(z) \to y_n(z_n)$. The system may in theory be evolved using the Euler method,

$$y_{n+1} = y_n + \Delta z f(z_n, y_n), \tag{3.53}$$

but in practice this will only be accurate to $\mathcal{O}(\Delta z^2)$. The Runge-Kutta technique is comparatively sophisticated, relying on more than just the derivative value at the beginning of each step to estimate the solution. By predicting the value of y at midpoints between z_n and z_{n+1}, it is possible to evaluate midpoint derivatives to better approximate the full-step solution. This is most clearly understood by considering the mathematical implementation of the second-order RK method, which is

$$k_1 = \Delta z f\left(z_n, y_n\right), \tag{3.54}$$

$$k_2 = \Delta z f\left(z_n + \Delta z/2, y_n + k_1/2\right), \tag{3.55}$$

$$y_{n+1} = y_n + k_2. \tag{3.56}$$

The additional information and extra step used in the second-order RK method return solutions with an improved accuracy of $\mathcal{O}(\Delta z^3)$. As we have already stated, the fourth-order RK method is the technique used to solve the differential equations used in our pulse-evolution study. Mathematically, the implementation is

$$k_1 = \Delta z f\left(z_n, y_n\right), \tag{3.57}$$

$$k_2 = \Delta z f\left(z_n + \Delta z/2, y_n + k_1/2\right), \tag{3.58}$$

$$k_3 = \Delta z f\left(z_n + \Delta z/2, y_n + k_2/2\right), \tag{3.59}$$

$$k_4 = \Delta z f\left(z_n + \Delta z, y_n + k_3\right), \tag{3.60}$$

$$y_{n+1} = y_n + k_1/6 + k_2/3 + k_3/3 + k_4/6, \tag{3.61}$$

which returns solutions shown to be accurate up to $\mathcal{O}(\Delta z^5)$. While more complicated approaches exist, using higher-order RK methods and variable step sizes in z, the implementation as described is sufficient for systems similar to which we investigate [104,109].

Equations 3.57 to Eq. 3.61 describe how to evolve a field in accordance with a single

differential equation. The four fields which we evolve under the coupled equations 3.47 to 3.50 will each correspond to their own 'y' when being evolved, with the other three fields contributing to the change in this field through the $f(z_n, y_n)$ terms. However, each of these fields will also need to be evolved simultaneously in accordance with their own respective coupled equation. In order to evolve all fields concurrently at each step, the creation of a temporary copy each field is necessary, so that this unmodified copy of the field may be applied through the coupled equations to act on the others. In this way Eq. 3.61 will be always be applied to each of the fields simultaneously.

The SSF code is used to assist in the understanding of the BS-FWM interaction, although some of the approximations made, such as the value of the nonlinear coefficient, mean that the absolute quantitive results are of significantly less value than the comparative behaviours observed for different initial conditions. For this reason, normalised values of amplitude are used in the discussion of the numerically obtained results.

Figure 3.13 displays the input (blue) and output (red) squared amplitudes for all four fields from a simulated propagation through 40 cm of PCF 2. Note that this length exceeds the length at which maximum conversion is achieved (see Fig. 3.14), but is chosen to make the effects of phase modulation and pulse walk off to appear more pronounced. The pump fields are both initialised as having 15-ps pulse durations, with pulse energies of 0.4 nJ which are derived from a specified average power of 32 mW and an 80-MHz repetition rate. The power of the Sr input is set to be a factor of 10^{-5} times that of the pumps, and the pulse duration is set to be 15 ps. The shape of the temporal amplitude distribution for pump field Q does not change with propagation, which is to be expected as this field both acts as the temporal-reference frame, and experiences only negligible effects arising from the FWM terms. The pump field P experiences only a slight shift in the temporal offset, which occurs because of the group-velocity mismatch between it and pump P. The two Gaussian-shaped pump pulses are modified in the spectral domain by the the effects of phase modulation in

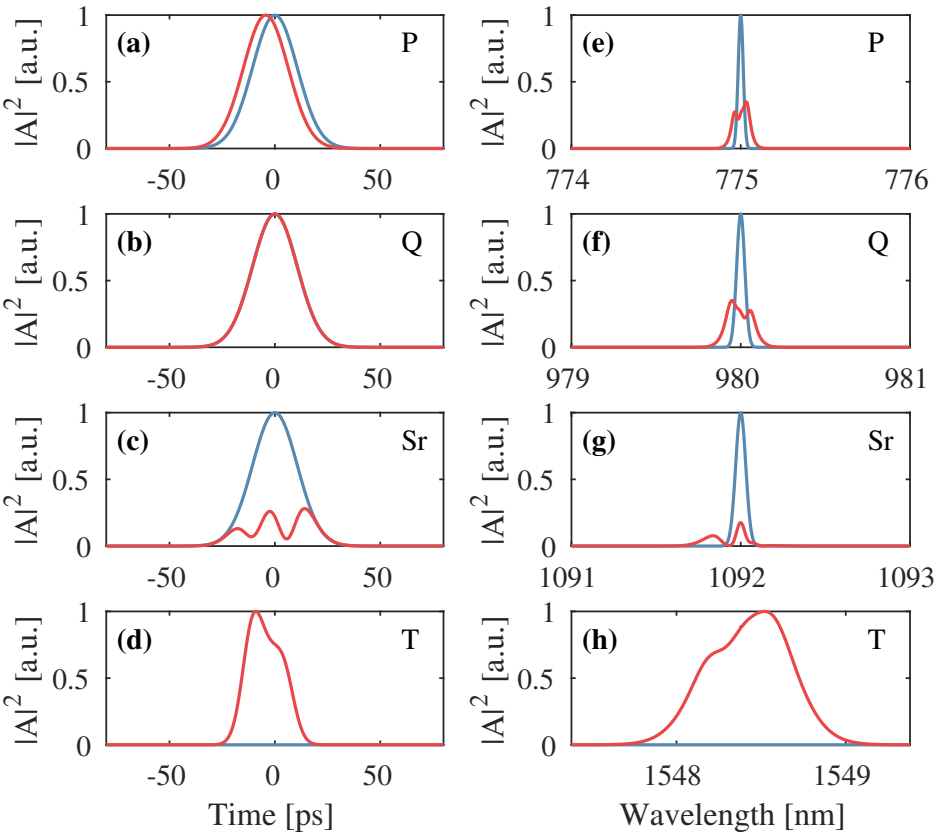

Figure 3.13 (a-d) The input (blue) and output (red) squared-amplitude temporal distributions for all four fields from a simulated propagation through 40 cm of PCF 2. (e-h) Squared-amplitude wavelength distributions. The displayed intensities of the pumps are normalised to the peak power of pump Q. The source intensity is normalised to the input peak power and the the target intensity is normalised to the output peak power.

a more pronounced way, with the difference in group velocities between the pumps inducing a degree of asymmetry in the distortion.

Because of the BS-FWM interaction, both the temporal- and spectral-domain intensity of the input source is depleted, while the target grows from zero amplitude into a Gaussian-like pulse. The power distribution between the source and target fields oscillates as the fields are evolved, although the coupling strength will diminish as the four fields walk off from each other in time and are increasingly distorted by the effects of phase modulation.

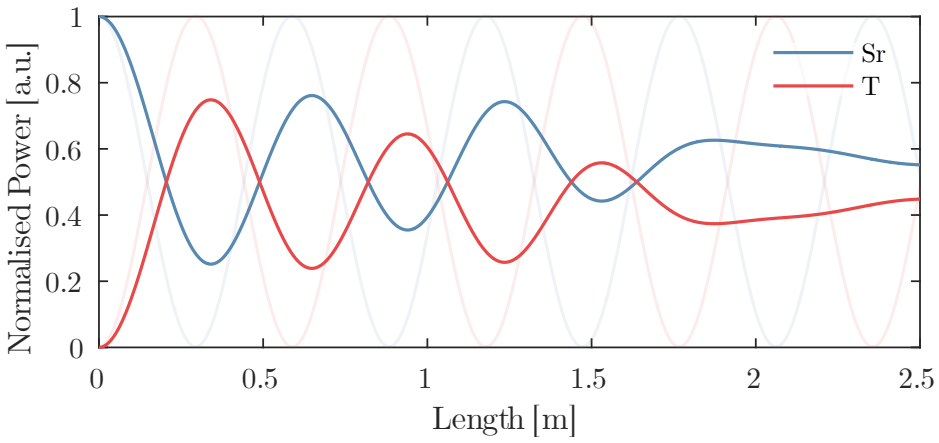

Figure 3.14 The power distribution between the source (blue) and target (red) fields oscillates as a function of propagation length. The coupling between the two fields is diminished as the pulses walk off from each other and are degraded by nonlinear phase modulation. Shown also (faded) is the simulated power distribution between the two fields when CW light is used with pump powers equal to the peak powers of the pulsed configuration.

This is clearly depicted in Fig. 3.14, which shows the total normalised power in both the source and target fields as a function of length for an extended propagation up to 2.5 m. All simulated parameters for this propagation are identical to those used to produce Fig. 3.13, and are overlaid on top of a (faded) equivalent plot which is simulated using CW, not pulsed, fields where the pump powers are equal to the peak powers of the pulsed configuration; this provides a visual reference to indicate how the BS-FWM process would change when pulse walk-off is neglected.

In Fig. 3.15 the values of $\beta_1(\omega) - \beta_1(\omega_{0,Q})$ are plotted for our PCF design under consideration, which serves as a useful reference when discussing the simulated pulse-propagation results that follow. By comparing the values of β_1, we can see that the pulses of pumps P and Q will walk off from each other by more than 10 ps per metre of propagation. For the simulated 15-ps-duration pulses this corresponds to a walk-off length of $L_\mathrm{w} = \tau[\,\beta_1(\omega_{0,P}) - \beta_1(\omega_{0,Q})]^{-1} \lesssim 1.5\,\mathrm{m}$. However, the equivalent walk-off length between the input source pulse and pump Q is much longer at $\simeq 23\,\mathrm{m}$ as their group velocities are closer matched.

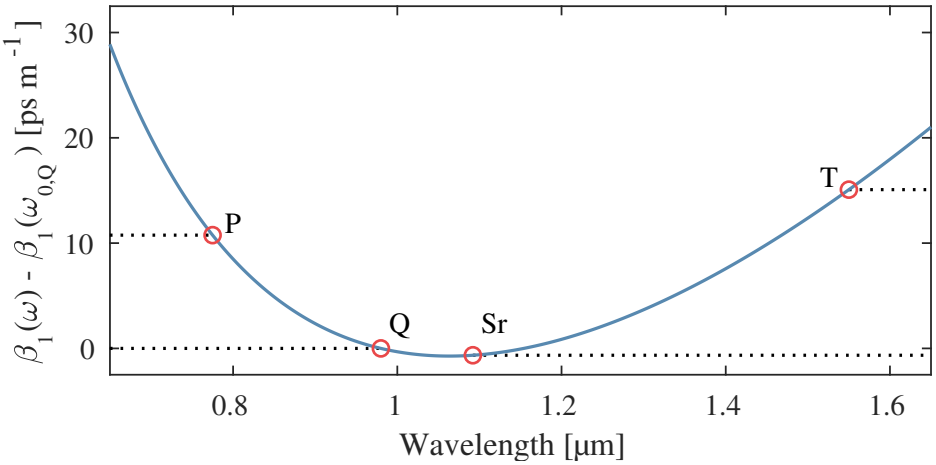

Figure 3.15 The frequency-dependant displacement of β_1 from $\beta_1(\omega_{0,Q})$ in PCF 2. Markers indicate the values of β_1 at the central wavelength of each field.

We investigate the BS-FWM process by performing parametric sweeps of simulation parameters and evaluating the response of the maximum conversion efficiency and the length along the fibre at which this occurs. To begin, the pulse duration of both pumps, as well as the source field, are varied in unison from 1 to 80 ps. The pulse energies are kept constant at 0.4 nJ and accordingly the peak power of each field diminishes with the expanding pulse duration. We see from Fig.3.16 that for constant pulse energies the conversion efficiency will not change, but that the reduction in peak powers leads to an increased nonlinear coupling length. The total efficiency is limited by the pulse energy and the fact that at lengths beyond z=0 the pump pulses do not fully encompass the source pulse in time.

Fixing the pump durations to 15 ps and pulse energies to 0.4 nJ, we vary the source-pulse duration from 0.15 to 150 ps to investigate the dependance of the pulse-duration mismatch between the input Source field and the short-duration pumps. The results which we observe in Fig. 3.17 show that higher conversion efficiency is achieved when the pump pulses have a duration which is longer than, and hence fully encloses, that of the input. However, when the input has a duration that is too short, the conversion efficiency drops as the BS-

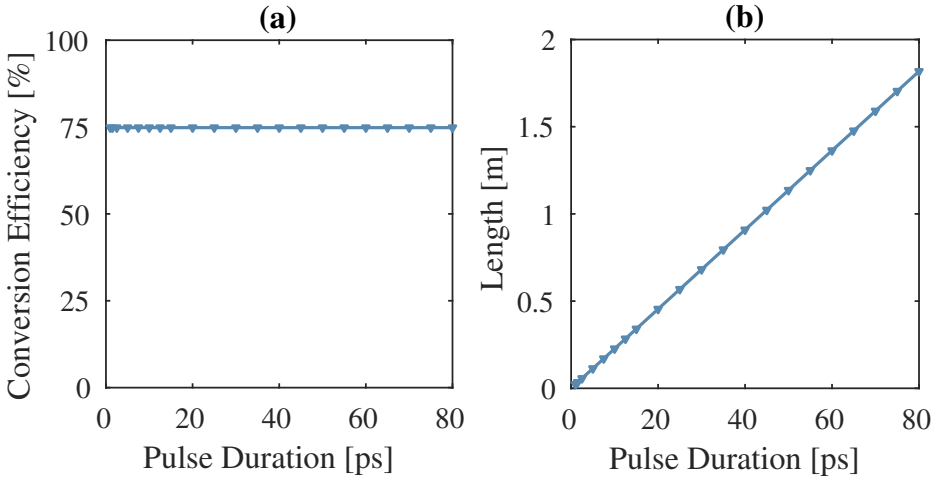

Figure 3.16 Simulated translation-efficiency results for differing initial pulse durations assigned to all fields. Both pump fields have fixed pulse energies of 0.4 nJ. (a) The maximum conversion efficiency. (b) The length at which maximum conversion efficiency is achieved. The markers indicate the simulated cases and the connecting lines serve as a visual reference.

FWM process fails to translate the outer spectral wings as efficiently as frequencies close to $\omega_{0,Sr}$. It is worth noting also that the input pulse walks off in time quicker as pulse duration decreases; the optimal ratio between the input- and pump-pulse durations will be dependant on the on the relative group velocities of the four fields in the fibre, but also on the absolute values of pump-pulse durations.

It might be expected that increasing the average power (pulse energy) of the pump will always yield greater conversion efficiency. However, we see from Fig. 3.18 that for the same short pump-pulse durations (15 ps) increasing the pump-pulse energy fails to meaningfully improve the achievable conversion. Two intrinsic properties of pulsed frequency conversion are responsible. Firstly, when scaling the nonlinearity it is not only the FWM terms that are affected; the detrimental effects of phase-modulation begin to dominate if the power is increased too much. As we have established, selecting a pulse duration ratio of $\tau_{Sr}/\tau_{P,Q} = 1$ means that, even from the first instances of the propagation, the pump-pulse temporal envelopes does not wholly enclose that of the input. To overcome this an almost

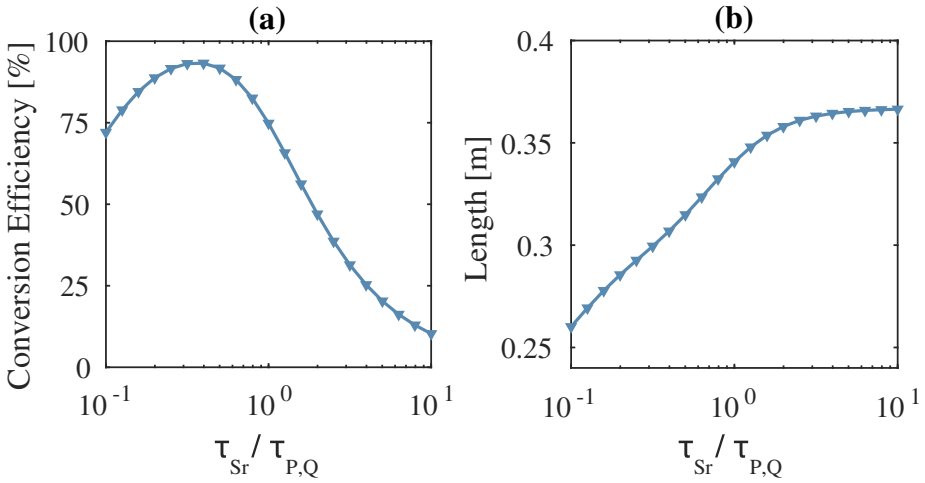

Figure 3.17 Simulated translation-efficiency results for differing durations of the input source. Both pump fields have fixed pulse energies of 0.4 nJ and pulse durations of 15 ps. (a) The maximum conversion efficiency. (b) The length at which maximum conversion efficiency is achieved. The markers indicate the simulated cases and the connecting lines serve as a visual reference.

instantaneous conversion is necessitated to achieve unit efficiency, one which cannot realistically be achieved by scaling the BS-FWM interaction strength with power. Power - after all, cannot be decoupled from the spurious nonlinear effect of SPM and XPM which inhibit conversion. Secondly, by definition the pulsed pumps do not have uniform field amplitudes as a function of time, meaning that induced optical nonlinearity is stronger at the centre of these pulses. When both pumps are temporally overlapped, the BS-FWM interaction is far stronger at t=0 than elsewhere and as such the portion of the input source field overlapped here is converted with the greatest efficiency. Due to the sinusoidal behaviour of BS-FWM it is possible that this portion of the field may be successfully converted and then reconverted back before other temporal regions undergo meaningful conversion at all. Again, this is resolved by making use of longer duration pump pulses, as at some limit the field amplitudes of both pumps will be near uniform across the duration of the input source pulse.

On the other hand, we also see that reducing the pulse energy below 0.3 nJ rapidly reduces the BS-FWM interaction strength and the achievable conversion efficiency. It is

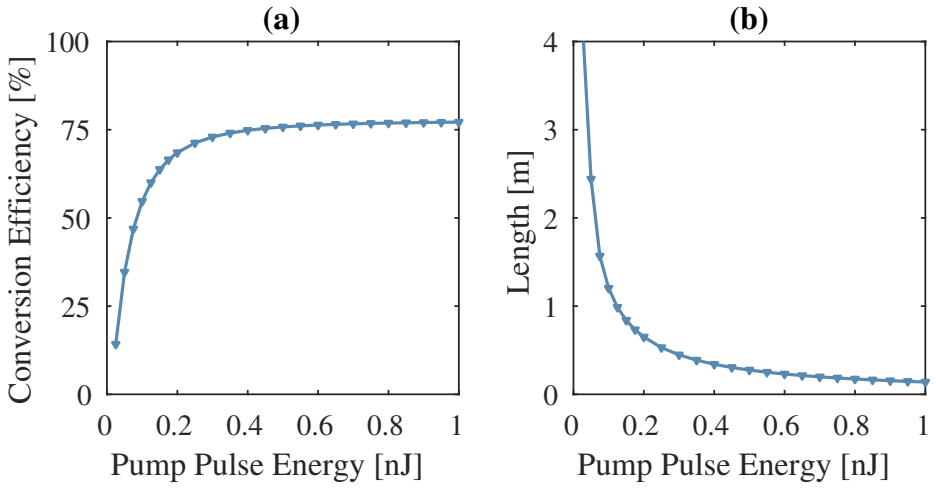

Figure 3.18 Simulated translation-efficiency results for differing pump-pulse energies. Both pump fields have fixed pulse durations of 15 ps. (a) The maximum conversion efficiency. (b) The length at which maximum conversion efficiency is achieved. The markers indicate the simulated cases and the connecting lines serve as a visual reference.

in this regime that the pump power limits the conversion of even the temporal regions of the input pulse which the strongest BS-FWM interaction and those that are the last to walk off from the pumps. Pump power plays an important role in determining the maximum achievable conversion efficiency of BS-FWM, but cannot be used to overcome poorly matched temporal profiles of the initial fields.

It is important to consider which other parameters we may be able to tune to optimise the prospective performance of a BS-FWM converter. It is possible to introducing temporal offsets to individual pulses to better allow the input pulses to walk through each other and extend their interaction. Figure 3.19 depicts the effects of temporally offsetting the pump, P, ($\lambda_P = 775\,\text{nm}$) from the the pump, Q, and input, Sr. In this instance, pump pulses with an energy of 0.1 nJ and duration of 15 ps are used as we have noted for these parameters that the maximum conversion efficiency is power limited (see Fig.3.18). A marginal performance increase is observed by introducing a delay to the pump P, which is maximised at a value of $\Delta t \simeq 6\,\text{ps}$. It is to be expected that some small offset will increase the achievable conversion

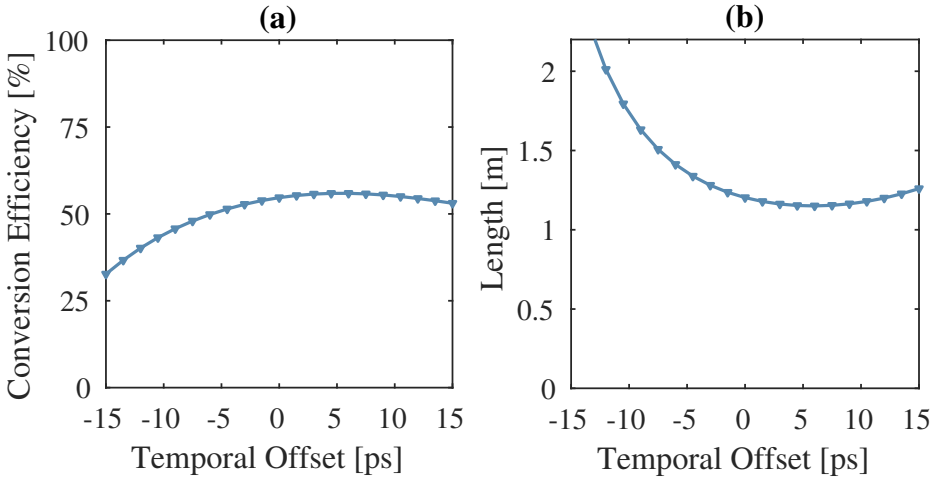

Figure 3.19 Simulated translation-efficiency results for varying temporal offset of the pump pulse P relative to the other to input fields. Both pump fields have fixed pulse energies of 0.4 nJ and pulse durations of 15 ps. (a) The maximum conversion efficiency. (b) The length at which maximum conversion efficiency is achieved. The markers indicate the simulated cases and the connecting lines serve as a visual reference.

and the magnitude evaluated for this offset appears sensible as it equates to just under half of the pump-pulse duration, with the length at which the maximum conversion being achieved being nearly equal to the walk-off length between the pumps.

It is important to also consider how the conversion efficiency is impacted by the use of pump powers that are not balanced. We investigate this by simulating the BS-FWM conversion for pumps with a pulse energy mismatch $\Delta E_{\mathrm{p}} = (E_{\mathrm{p,Q}} - E_{\mathrm{p,P}})/2$, where the total energy remains equal to $E_{\mathrm{p,P}} + E_{\mathrm{p,Q}} = 0.8\,\mathrm{nJ}$. For large values of pulse-energy mismatch the frequency-translation efficiency drops dramatically. This is expected, as we have seen from Eq. 3.24 that the expression for κ_{BS} has a term that is dependant on the subtracted value of pump powers. Furthermore, the expression for κ_{BS} is not symmetric in power and takes on different values if the powers of pumps P and Q are interchanged.

Finally, we consider the impact of scaling all pulse durations whilst keeping the peak powers of the two pumps fixed. For a fixed propagation distance, we vary the pulse duration of all pulses (input and pumps) between 15 fs and 15 ns. We then measure the conversion

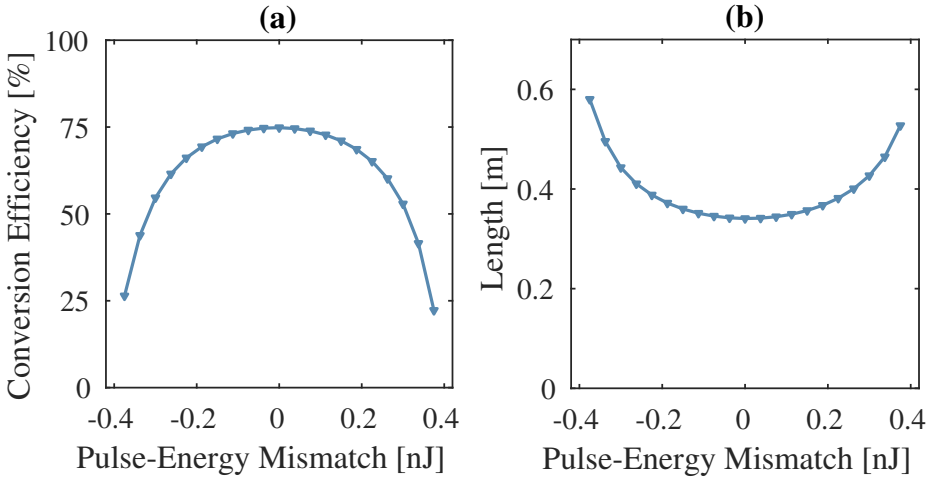

Figure 3.20 Simulated translation-efficiency results showing the role of pump-power mismatch. Both pump fields have fixed pulse durations of 15 ps, but have pulse energies that vary while satisfying the condition $E_{\mathrm{p,P}} + E_{\mathrm{p,Q}} = 0.8\,\mathrm{nJ}$. (a) The maximum conversion efficiency versus pulse-energy mismatch, $\Delta E_{\mathrm{p}} = (E_{\mathrm{p,Q}} - E_{\mathrm{p,P}})/2$. (b) The length at which maximum conversion efficiency is achieved. The markers indicate the simulated cases and the connecting lines serve as a visual reference.

efficiency as achieved at the end of the propagation. In doing so we aim to verify that the physics explored within this chapter, and that which is presented in Chapter 4, scales appropriately to the nanosecond regime in which an interface for converting photons from ion traps will need to operate. The propagation distance is selected to be equal to the length at which maximum conversion is achieved for a pulse duration of 15 ps. Figure 3.21 shows that the maximum conversion efficiency does not vary with an increase in pulse duration from the picosecond to the nanosecond regime, so long as the peak powers of the pump pulses are linearly scaled with the pulse durations. This is a critical point to make when establishing the context of the work set out within this thesis; the results presented herein remain relevant to a frequency conversion interface which operates with nanosecond pulses and is, as such, compatible with photons emitted from a trapped ion. However, going to shorter pulse durations means that the pulses associate with the different fields in the fibre will walk off from each other before meaningful conversion takes place.

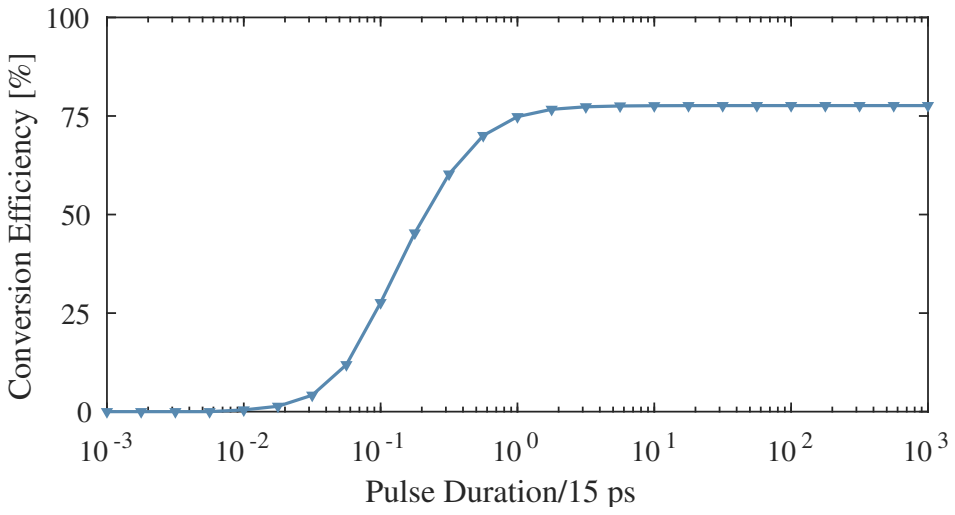

Figure 3.21 Simulated translation-efficiency results for differing pulse durations of all fields, ranging between 15 fs and 15 ns. Both pump fields have fixed peak powers, which are selected to correspond to a pulse energy of 0.4 nJ when the pulse durations are 15 ps; the pulse energies of the 15-fs and 15-ns pump pulses are 0.4 pJ and 0.4 µJ, respectively. We present the conversion efficiency as achieved at a length of 0.35 m, which is approximately the length at which maximum conversion efficiency is achieved for pulse durations of 15 ps. The markers indicate the simulated cases and the connecting lines serve as a visual reference.

A number of conclusions can be drawn about BS-FWM frequency conversion from the results of pulse-propagation study presented within this section. Firstly, when using pulsed pumps, it is important to ensure that the pulse duration of the pumps exceeds the duration of the input photon. The dispersion in a $\chi^{(3)}$ medium will mean that pump pulses which are matched to the duration of the input will walk off both from each other, as well as the input field before 100% conversion is achieved, fundamentally limiting the efficiency. Secondly, where power is a resource which is in some way shared between the two pumps, it is preferable to ensure that the power balance between the two fields is as equal as possible as this will improve the observed BS-FWM conversion efficiency. Thirdly, particularly when the group velocity is not symmetric about the central frequency of the BS-FWM interaction, careful adjustment of the temporal offsets between the input and pump fields may yield higher conversion efficiencies as pulses may be ordered such that they 'walk through' each

other along the waveguide length. Finally, we note that the maximum conversion efficiency achieved for a fixed length of fibre does not vary with pulse duration, so long as the peak powers of the pump pulses are scaled with the pulse durations and the pulses are not so short as to temporally walk off from along this length.

Chapter 4

Third-Order Nonlinear Frequency Conversion: Realisation

This chapter presents the experimental realisation of the resource-efficient four-wave-mixing conversion which was introduced in Chapter 3. Section 4.1 contains a description of the fabrication process which is used to produce the PCFs before detailing how a Mach-Zender interferometer is used to verify the dispersion profiles of the fibre. An experimental characterisation of the seeded FWM source is included in Section 4.2. Sections 4.3.1 and 4.3.2 present the realised BS-FWM conversion experiment and include a characterisation of the up- and down-conversion performance.

4.1 The micro-structured optical fibres

4.1.1 Fabricating photonic crystal fibres

The most common approach to fabricating micro-structured optical fibres is the stack-and-draw technique, an approach that involves assembling the desired structure on a macroscopic scale before drawing it down to size using a specialised fibre-drawing tower. Both of the PCF designs are fabricated using the stack-and-draw technique, which is illustrated in Fig. 4.1.

The majority of optical fibres are made using fused-silica glass. For the PCFs we use synthetically-fused-silica rods and tubes, Heraeus[1] F300, which are produced with high chemical purity and geometric precision. In the first stage of the fabrication process, a fused-silica tube of $\sim$ 25-mm outer diameter (OD) is drawn down using a cane tower to produce an identical set of 1-m length capillaries with an OD of $\sim$ 1.5 mm. Next, the collected set of capillaries are arranged, with the aid of a jig, to form a hexagonal close-packed stack which embodies the macroscopic scale structure of the desired PCF. A solid fused-silica rod is inserted in to the centre of the stack to form a defect, which later becomes the guiding core of the PCF. This rod, also Heraeus F300, is drawn from a commercial precursor formed by chemical vapour deposition, ensuring an OH content below 1 ppm and accordingly a reduced level of optical absorption in the final fibre.

Once assembled, the entire stack is inserted into a cladding tube and drawn into *canes*. At this stage, where the stack is drawn to canes, a vacuum is applied through a slot made in the side of the cladding tube in order to collapse the interstitial vacancies between the capillaries. The cane diameters (3-3.5 mm) are selected to complement the available jacketing tube sizes such that the final fibre, once drawn, has an OD between 120-150 µm. Each cane is inserted inside the chosen jacket tube (OD = 10-15 mm) and drawn down to make the finished PCF using the fibre tower. During the fibre draw, the holes in the structure will shrink or collapse entirely due to surface tension as the glass is heated, although gas pressure can be applied

[1] https://www.heraeus.com/

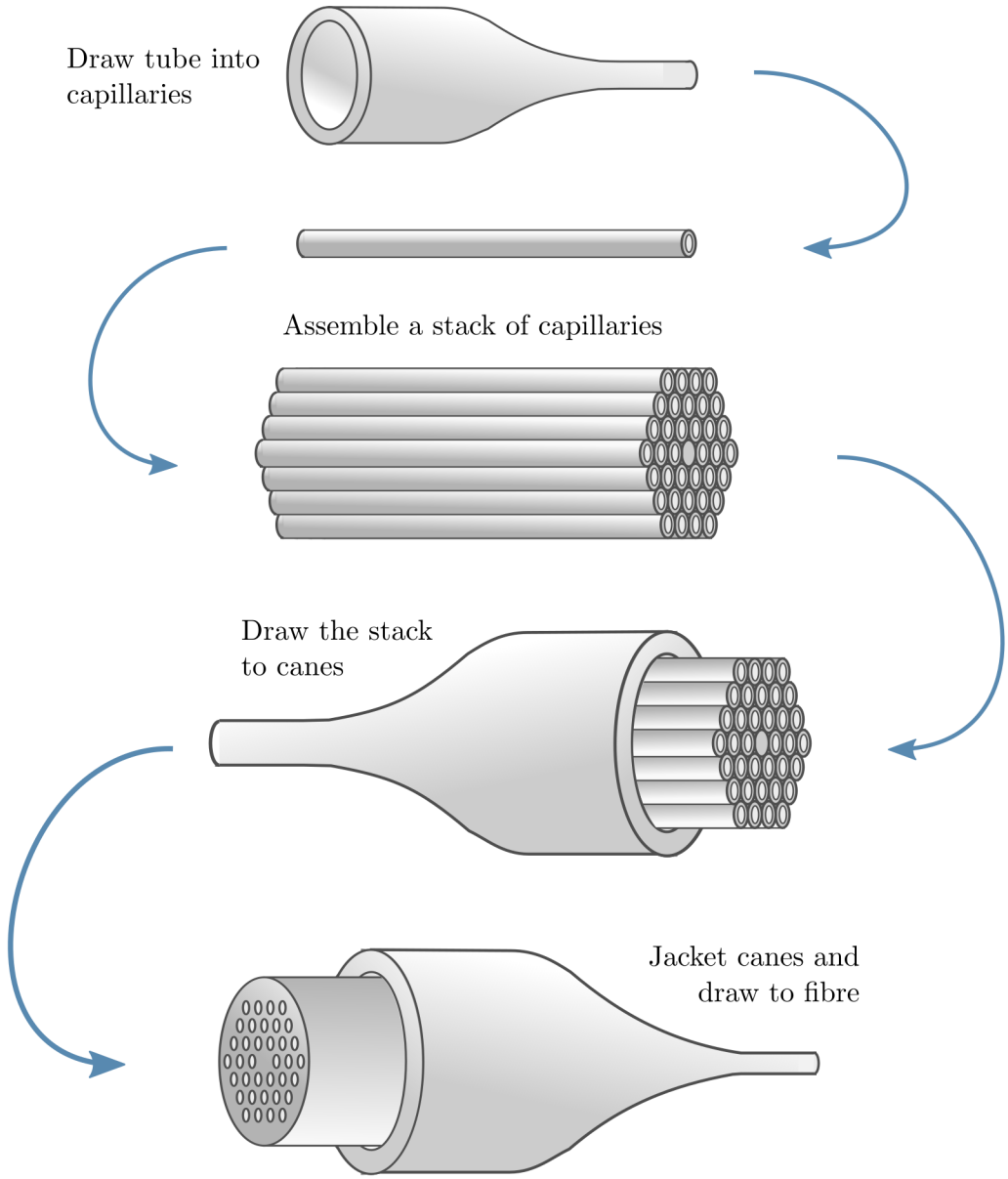

Figure 4.1 The Stack and Draw technique of PCF fabrication.

to resist this collapse. The lattice of holes in the cane are pressurised with nitrogen, which acts against the surface tension of the glass and ensures these air holes remain in the cross section of the final fibre. Likewise, a vacuum is applied to ensure the region between the inner surface of the jacket tube and the outer surface of the cane collapses. Before being

wound on to a collection drum, a UV-curing polymer coating (Desolite) is applied as, despite being remarkably strong, optical fibres are susceptible to breakages caused by contaminants and abrasion.

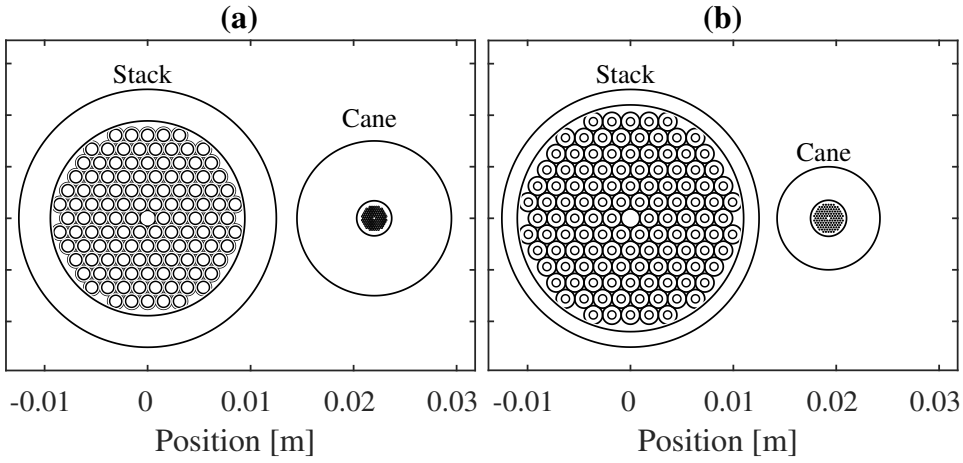

Figure 4.2 Stack and jacketed-cane geometries of (a) PCF 1 and (b) PCF 2. Small fused-silica packing rods are also used to populate the empty spaces between the hexagonal stack of capillaries and the surrounding cladding tube.

The geometries of the precursor stages to PCF 1 and PCF 2 are depicted in Fig. 4.2, with the specific parameters listed in Appendix A. Schematics of the cane and fibre towers are shown in Fig. 4.3. On the upper-most level of the three-story tower, a clamp is used to secure either the glass preform, rod or tube which is being drawn. Here, if required, tubing from the pressure and vacuum control system can be secured to a preform using bespoke brass attachments. The clamp securing the glass is connected to a feed mechanism which slowly lowers the glass into the furnace that is mounted below. Underneath the furnace, a laser micrometer provides diameter and position measurements of the fibre, tube, rod or cane which is being drawn from the glass entering the furnace. Depending on whether larger structures, i.e. tubes, rods and canes, or smaller structures, i.e. optical fibre, are being drawn, either a puller belt mechanism or a capstan may be used to draw the glass out of the furnace. If optical fibre is being drawn then polymer coating is applied to the fibre as

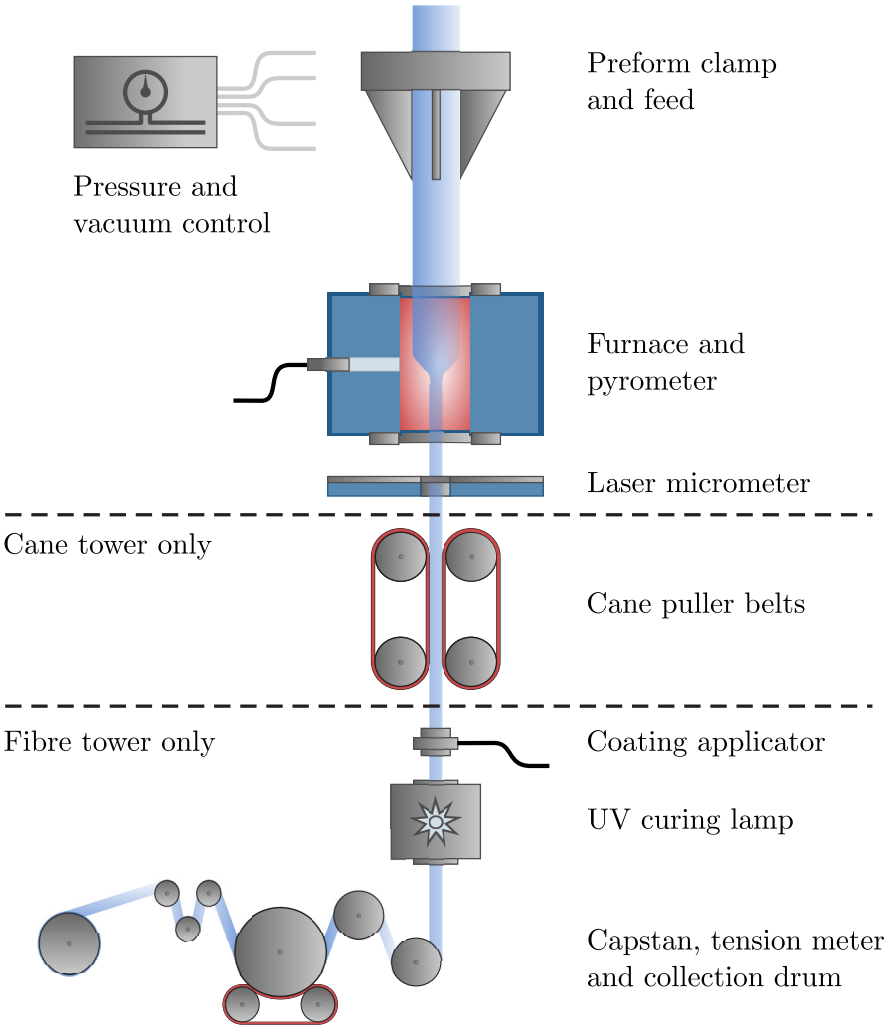

Figure 4.3 Schematic diagram of the fibre/cane drawing tower. The uppermost section which consists of a clamp, preform-feed mechanism, pressure controls, furnace and laser micrometer is inclusive to all applications, with the pulling mechanism dependant on the fabrication stage. When drawing rods, capillaries or canes, the middle section containing a belt system is used. If optical fibre is being drawn then the lower section is used to coat the fibre, monitor tension and wind the fibre onto a drum.

it passes through a die, which is then cured using a UV lamp mounted just below. The fibre tension is monitored before it is eventually wound on to a collection drum. Using the available controls on the drawing tower — preform feed, draw speed, furnace temperature, and pressure and vacuum levels — small changes may be made to adjust the structural parameters of the final PCF. During each draw we collect multiple bands of fibre, each

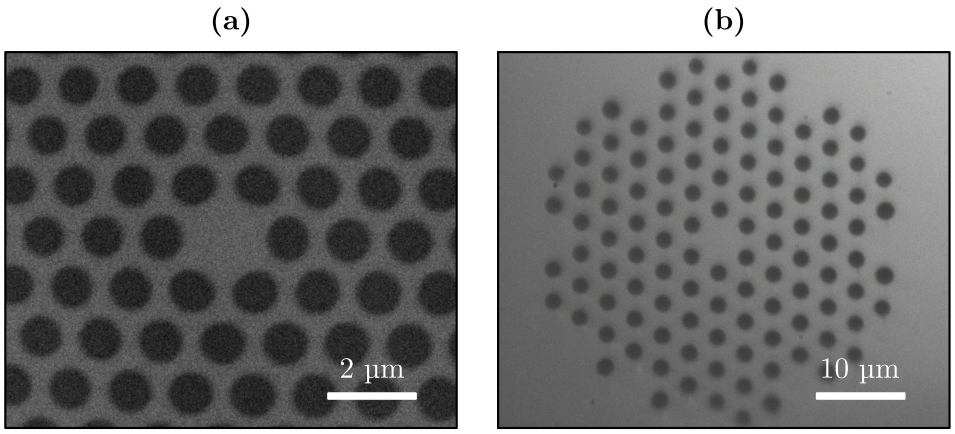

Figure 4.4 (a) Scanning electron micrograph of PCF 1. (b) Optical micrograph of PCF2.

with a slightly different set of draw parameters. Consequently, we obtain multiple sections of PCF, each with different cladding structures. Whilst fabricating, we collect samples at the beginning of each band and inspect the the structure under an optical microscope before readjusting the draw parameters to be used for the following band. This allows us to iterate towards a set of draw parameters that produce a PCF with the closest possible structure to that of the simulated design. However, the optical microscope resolution is insufficient to determine the air-hole sizes accurately, with any small structural changes being imperceptible. Further experimental techniques are therefore necessary to ensure that the fabricated PCFs closely resemble the simulated designs. Cross sectional images of the fabricated PCFs are shown in Fig. 4.4.

4.1.2 Characterising optical fibres

Further characterisation of these fibres is carried out to ensure that the engineered dispersion is appropriate to the desired FWM and BS-FWM processes. The GVD profile of the seeded FWM fibre, PCF 1, is experimentally characterised using a white-light Mach-Zender interferometer. A schematic of the set up is shown in Fig. 4.5. A microchip laser is used to pump a supercontinuum (SC) fibre, providing a source of white light with single-mode

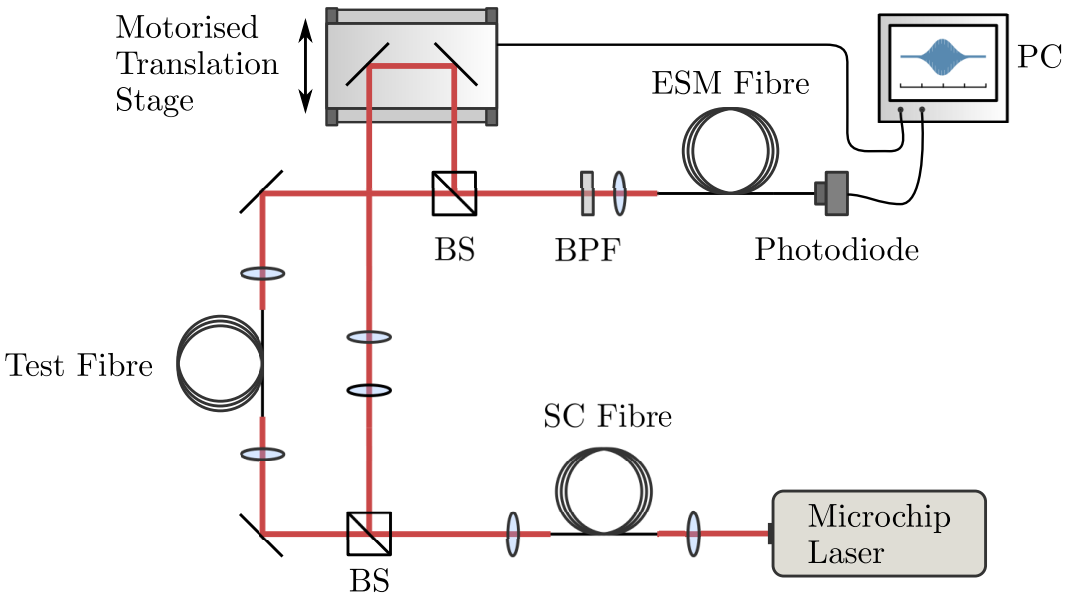

Figure 4.5 Schematic of the experimental setup to characterise the group velocity dispersion of PCF. A supercontinuum light source produces a white-light beam, which is divided at a beam splitter into the two arms of the interferometer. One arm of the interferometer containins the test fibre and the other arm acts as a reference. Interference fringes are observed when the optical path difference (OPD) between the two arms is close to zero at the recombination point. We introduce a variable free-space delay in the reference arm to compensate for the optical delay associated with the test fibre and to find the position where OPD = 0. Furthermore, a telescope in the reference arm is also included to compensate for the dispersion associated with the achromatic coupling lenses. After the beams are recombined at the second beam splitter, they are passed through a band-pass filter and directed towards a fibre-coupled photodiode. The photodiode signal is monitored as a function of the delay stage position.

beam characteristics. The white-light beam is divided at a beam splitter into the two arms of the interferometer, one containing the test fibre and the other serving as a reference. As with any white-light interferometer, high-visibility interference fringes are observed when the optical path difference (OPD) between the two arms is close to zero at the recombination point. A variable free-space delay is therefore introduced in the reference arm to compensate for the optical delay associated with the test fibre. Furthermore, a telescope in the reference arm is also included to compensate for the dispersion associated with the achromatic coupling lenses. After the beams are recombined at the second beam splitter,

they are passed through a band-pass filter and directed towards a photodiode which is fibre coupled using endlessly-single-mode (ESM) fibre. For a given band-pass filter (BPF) the photodiode response as a function of the optical delay in the reference arm is recorded, with measurements repeated using BPFs with central wavelengths between 550 nm and 1200 nm; a typical interference fringe is shown in Fig. 4.6.

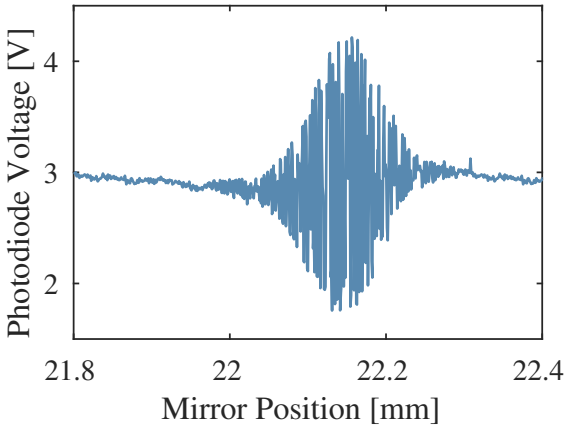

Figure 4.6 An example of an interference fringe obtained using the white-light Mach-Zehnder interferometer. The OPD is equal to zero at a mirror position of ∼22.15 mm.

Using these measurements, it is relatively straightforward to recover the dispersion of the fibre. The optical path lengths (OPLs) in of the reference and fibre arm are given by

$$OPL_{\mathrm{ref}} = L_{x0} + 2x \tag{4.1}$$

and

$$OPL_{\mathrm{fib}} = L_{\mathrm{a}} + n_{\mathrm{g}} L_{\mathrm{fibre}}. \tag{4.2}$$

Here, L_{x0} is the path length of the reference arm when the position of the translation stage, x, is zero. The lengths L_{a} and L_{fibre} denote the free-space optical path length in the fibre arm and the fibre length, respectively. The value of x is given by the displacement position of the motorised stage that is required to compensate the difference in OPL between the

two arms. If the optical path difference is zero then

$$n_{\mathrm{g}} = \frac{2x + L_{x0} + L_{\mathrm{a}}}{L_{\mathrm{fibre}}}. \tag{4.3}$$

We can combine Eq. 3.11 and Eq. 3.12 to obtain an expression that relates the dispersion parameter to the measured group index,

$$D = \frac{\mathrm{d}\beta_1}{\mathrm{d}\lambda} = \frac{1}{c}\frac{\mathrm{d}n_g}{\mathrm{d}\lambda} = \frac{2}{c\,L_{\mathrm{fibre}}}\frac{\mathrm{d}x}{\mathrm{d}\lambda}, \tag{4.4}$$

which allows us to use our measurements of the wavelength-dependant change in interference-fringe position to evaluate a measured value of the dispersion parameter. The results are fitted using a fourth-order polynomial and plotted in Fig. 4.7 alongside the simulated dispersion. The ZDW of the simulated structure of PCF 1 is 780 nm, whereas by comparison

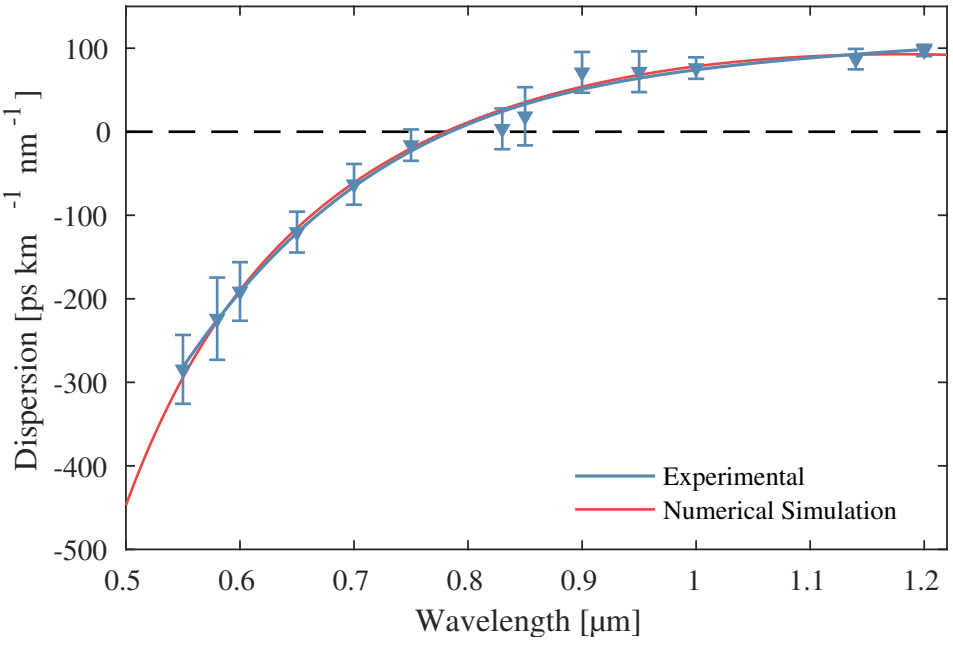

Figure 4.7 The experimental (blue) and simulated (red) GVD curves obtained for PCF 1, which has the structural design parameters Λ=1.508 and d/Λ=0.637. The simulated ZDW is 780 nm, whereas the experimentally measured value is 782.5 nm

we obtain a value of 782.5 nm in the fabricated fibre. The discrepancy may be attributed to a combination of experimental uncertainty and slight deviations in realised geometry from that of the design; in the simulation the air holes are assumed to be circular, but in the fabricated fibre the innermost ring deform around the core (see Fig. 4.4).

4.2 The fibre optical parametric amplifier

The experimental implementation of the BS-FWM conversion scheme, which is outlined in Section 3.2 and schematised in Fig. 4.8, features an 80-MHz repetition rate Ti:sapphire laser (Spectra Physics Tsunami) as the source of the inceptive pump field. The Ti:Sapphire laser is wavelength tuned to ∼775 nm to fulfil the necessary energy-matching requirements associated with the two FWM interactions. The pulse duration is, however, not a parameter which is necessarily restricted by the energy or phase matching terms of these FWM processes, and nor is it subject only by our desire to fulfil the optimal conditions for BS-FWM conversion which are investigated as part of the pulse-evolution study in Section 3.3.2. In addition to acting as a pump field in the BS-FWM conversion, the Ti:Sapphire laser must also adequately pump a seeded FWM process to generate the second BS-FWM pump field using only a portion of the available optical power emanating from its cavity.

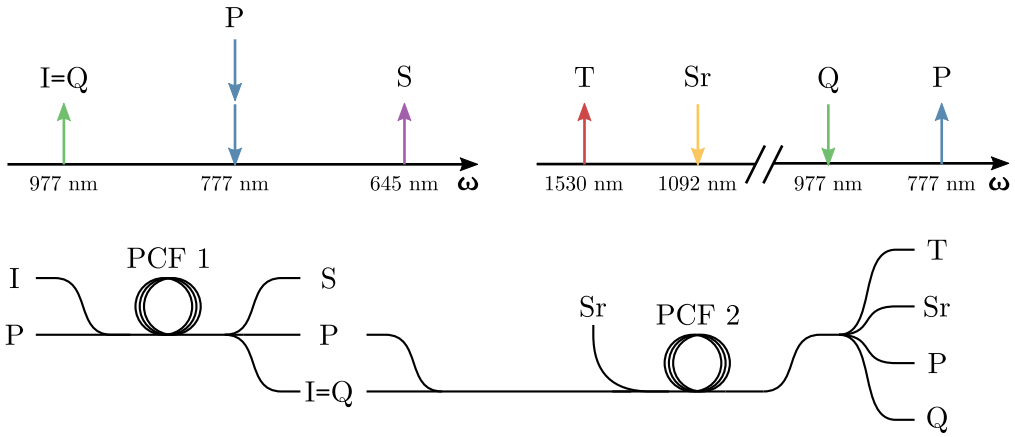

Figure 4.8 The resource-efficient BS-FWM scheme. Wavelength labels are given to the fields for convenience.

Previous demonstrations of FWM light sources have successfully made use of CW lasers to seed FWM sidebands of interactions pumped using ps-duration pump pulses [89,90]. The experimental parameters used in these demonstrations are shown in Table 4.1, with the obtainable parameters in this work included also for comparison. To reproduce similar field

Source	τ_p [ps]	R_p [MHz]	P_{avg} [W]	E_p [nJ]	P_p [kW]	A_{eff} [μm^2]	I_p [GWm^{-2}]
Mosley et al. [89]	40	0.5	0.1	20000	5	$\sim$16	$\sim$320
Lefrancois et al. [90]	7.7	54	1.6	29.63	3.848	$\sim$16	$\sim$220
This thesis	10(20)	80	$\leq$1	12.5	$\leq$1.25(0.625)	$\sim$1.8	$\lesssim$720(350)

Table 4.1 The pump field properties for FWM sources. The intensity values are estimates based on approximated mode field diameters.

intensities within the core of PCF 1, whilst allowing for a practical limit of ≤ 1 W average power to propagate through the first fibre, we are restricted to pulse durations below 20 ps. Of course, the intensity of a field within a fibre is also governed by the effective area of the mode which the light is propagating in. The effective are of the fundamental mode in a PCF, A_{eff}, is described in terms of the pitch, Λ, and air hole size, d, by the empirical relationship

$$A_{\text{eff}} \simeq \frac{1}{2}\left[(\Lambda/d) \times \Lambda^2 + \mathcal{O}(\lambda/d)\right], \tag{4.5}$$

as presented in a numerical study by Mortensen [110]. The peak powers which are obtainable within our experiment setup are lower than those listed for the experiments in the literature, however the pitch of the PCFs used in those experiments are on the order of twice the size of the pitch of PCF 1, and as such the field intensities achieved are likely to be comparable. We also know from Section 3.3.2 that, for the BS-FWM interaction, when pulse energy, i.e. average power, is sufficient, it is generally preferable to make use of pump pulses with longer durations. We therefore make a selection of a 15 to 20-ps pulse duration to best utilise the available resources of the Ti:Sapphire laser within this pump-power economy. It is notable that making use of a laser with a lower repetition rate, but also with longer duration pulses, may allow for the fulfilment of conditions which are preferable in both stages

of the experiment, so long as the average power remains sufficient. However, Ti:Sapphire lasers are workhorse pieces of equipment across many optics labs, including our own, with another alternative being presently out of hand.

The experimental arrangement for assessing the OPA performance is depicted in Fig. 4.9. The pump field from the Ti:Sapphire laser is first transmitted through an optical isolator

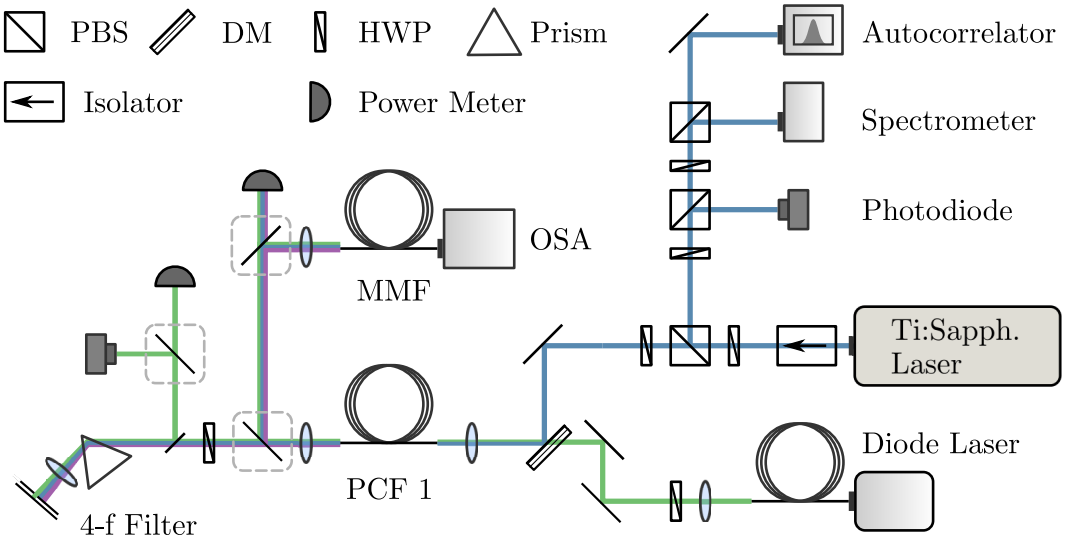

Figure 4.9 Schematic showing the experimental setup for characterising the seeded FWM in PCF 1. The 777-nm pump light (shown in blue) from the Ti:Sapphire laser is combined with 977-nm seed light (shown in green) using a dichroic mirror. The combined beam is then coupled into PCF 1. At the output of PCF 1, the light is directed towards a 4-f prism filter, which separates out the different frequencies into different spatial positions and uses a D-shaped mirror to reflect only the idler field towards either a power meter or a photodiode. Alternatively, a flipper mirror positioned before the 4-f filter directs the three spectral fields towards a power meter or a fibre-coupled OSA. The pump laser pulses are monitored with an autocorrelator and a photodiode.

in order to mitigate the susceptibility of the laser stability to back reflections from the input face of PCF 1, as well as other optical elements. The pump beam's polarisation and intensity is set using HWPs and a PBS. The beam from the reflected arm of the PBS is used as a pick-off line to monitor the pump pulses with an autocorrelator, spectrometer and Si photodiode. A fibre-coupled 5-MHz-linewidth diode laser (Thorlabs DBR976P) is used as the seed laser. Distributed Bragg reflector (DBR) lasers such as this are widely

available but frequently have a slight deviation in the central wavelength from the quoted design wavelength. Furthermore, the temperature-dependant wavelength response is smaller than for other laser diodes as the reflection band of the grating is spectrally shifted by less than the gain maximum. The diode in this experiment has a central wavelength of 977.2 nm (2.8 nm shorter than in the experimental design), which has a small but perceptible impact on the final wavelengths. After the seed-laser polarisation is set to match that of the pump, it is combined with the pump beam at a dichroic mirror and directed towards PCF 1. The light from both beams is coupled into the fibre using an aspheric lens, which is selected to maximise the coupling efficiency of the pump field. The out-coupling lens which appears after the polarisation-maintaining fibre connected to the 977.2-nm diode laser is selected to maximise the coupling of the seed light in to PCF 1, selected to work in conjunction with the coupling lens for the PCF. The pump and daughter fields launching out of the end of PCF 1 are re-collimated using another aspheric lens before being sent for analysis using one of a number of methods. The beam may be directed towards a 4-f prism filter, which separates out the different frequencies into different spatial positions and uses a D-shaped mirror to reflect only the idler field towards either a power meter or a photodiode. Alternatively, a flipper mirror positioned before the 4-f filter directs the three spectral fields towards a power meter or a multi-mode fibre (MMF)-coupled optical-spectrum analyser (OSA).

In PCF 1, the walk-off length between 15-ps pulses which are centred at the pump and signal (idler) wavelengths is 1.92 (1.71) m. The measurements reported here are obtained using a 45-cm length of PCF 1, which we select for optimum FWM sideband generation. Using shorter lengths of fibre results in the FWM being less efficient, whereas the use of longer fibres results in significant nonlinear broadening of the pump and sideband spectra.

The spontaneous- and seeded-FWM spectra from the OSA (Yokogawa AQ6374) are presented in Fig. 4.10. The average pump powers for the spectra vary between 200 and 750 mW, while seed power, when used is 30 mW. The seed power, as with values for the

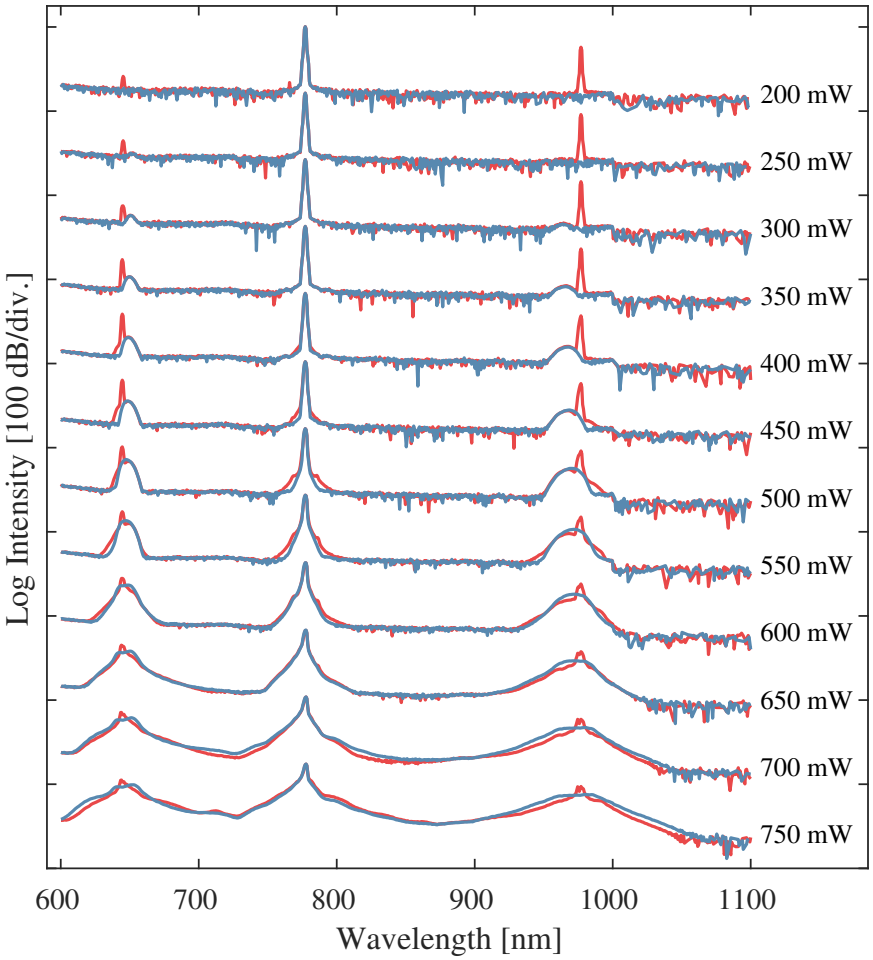

Figure 4.10 Seeded (red) and spontaneous (blue) FWM spectra for increasing pump power. The spectra are offset in increments of 80 dB for visibility and easier comparison. The spectral resolution is 1 nm.

pump, is expressed as the average power propagating through the PCF and is measured at the output of the fibre. The spectral resolution is 1 nm.

The remarkable effects of seeding at the idler wavelength are most clearly viewed by regarding the power-dependant amplitudes of the signal sideband, which is not spectrally impinged upon by the presence of the CW seeding field. For example, with a pump power of 450 mW there is a 25 dB difference in the peak signal amplitude between the spontaneous and seeded interactions. At increasing powers we see that the spontaneous sidebands increase in amplitude, but also become increasingly broad. At the 650 mW pump level the spontaneous

signal has a FWHM bandwidth of 13 nm, which is reduced to approximately 3 nm by seeding — at this pump-power level a 7 dB difference exists between the peak amplitude of the spontaneous and seeded signal. We note here also that the spontaneous sidebands are spectrally shifted further from the pump wavelength as the power increases, which comes as a consequence of the power-dependant SPM contribution to the phase matching. A consequence of this is that we are required to tune the pump wavelength such that the FWM sidebands spectrally overlap the seed laser best when operating at the power levels which are deemed most suitable for generating the second BS-FWM pump field.

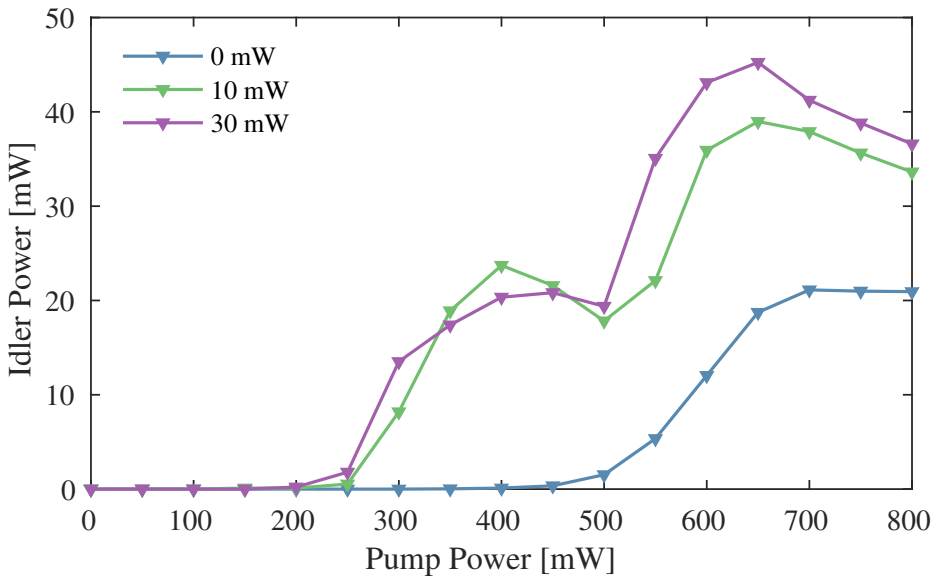

Figure 4.11 Idler output power as a function of pump power, as observed with seed powers of 0, 10 and 30 mW.

The pump-power-dependant idler levels are plotted in Fig. 4.11, for seed powers of 0, 10 and 30 mW. The sideband powers depicted are measured after the 4-f prism filter, which is set to have a 10-nm pass band centred at 977 nm, and the post-filter power level of the CW seed field is subtracted from each recorded value to ensure that only the generated pulsed light is accounted for (this practice is adopted for the remainder of this thesis). The pump and seed powers are measured directly after the PCF. We see that for measurements

above the threshold of $\sim 250\,\mathrm{mW}$, the pump-power dependance of the seeded sidebands is initially quadratic but quickly rolls off. Below pump powers of 500 mW the spontaneous FWM sidebands are spectrally located closer to the pump wavelength and are therefore not transmitted through the 4-f filter, which artificially shifts the observable pump-power threshold to appear at 500 mW. We can see from Fig. 4.10 that the spontaneous FWM sidebands appear distinguishable from the noise floor at pump powers as low as 300 mW, although they do have much lower amplitudes than their seeded counterparts. In Fig. 4.11 this manifests in the seeded sideband power-dependance as a reduction in the sideband generation between the pump powers of 350 mW and 500 mW, as the seeded sidebands compete with the growth of the spontaneous sidebands which exist outside the spectral pass band of the filter. Above 500 mW the spontaneous and seeded sidebands are both spectrally overlapped with the pass band and we observe a rapid increase in sideband power, which peaks around 650 mW. For pump powers exceeding 650 mW, the efficiency of both the spontaneous and seeded FWM rolls off due to the nonlinear pump broadening. Furthermore, we are able to determine that the intensity of the seed field is still of significance to the efficiency of the FWM process, at least up until the highest transmitted power of 30 mW.

Statistical analysis is also carried out in which we make use of three Si photodiodes, each with a rise time of 1 ns. Two of these photodiodes are depicted in Fig. 4.9: one measures the intensity of the pulse train emitted by the Ti:Sapphire pump laser, and the other measures the idler field transmitted through the 4-f prism filter. Simultaneously, we use an additional photodiode to monitor the the pump pulses after the PCF from a pick-off beam which is extracted by a temporary flipper mirror inserted within the 4-f filter line.

The photodiodes are connected to a digital oscilloscope and the traces exported to a PC for analysis. The maximum voltage registered by each photodiode for each of $\geq$2000 peaks is then extracted; as the response time of each photodiode is proportionately slow relative to the optical pulse duration, the recorded peak voltages are proportional to the pulse energy.

In Fig. 4.12(a), we show the normalised pulse-energy histogram for the idler field with a fixed pump power of 600 mW. Furthermore, in Fig. 4.12(b) and Fig. 4.12(c) we show the equivalent plots for pump powers of 650 and 700 mW, respectively. We select these values as they encompass a range across the upper limits of pump power at which it it is possible to operate the FWM source. At lower pump powers the spontaneous sidebands are significantly diminished in intensity and as such are harder to measure with the available photodiodes.

It is readily apparent that the spontaneous FWM sidebands suffer from significant amplitude noise, with the fractional standard deviations in pulse energy recorded as 38 %, 24 % and 20 % for the pump powers of 600, 650 and 700 mW, respectively. The large pulse-to-pulse fluctuations which exist in the sideband energies is due to these fields being initiated by quantum vacuum fluctuations, which are intrinsically noisy.

On the other hand, the seeded FWM sidebands exhibit a significantly reduced level of amplitude noise relative to the spontaneous sidebands. We observe that the fractional standard deviation in pulse energy is always below 10 %, although this value may be reduced further with additional seed power. The full complement of calculated standard deviations (SDs) for the normalised pulse-energy distributions of the idler are shown in Fig. 4.13. Here we see, by direct comparison, that for an increase in pump power, additional seeding power is also required in order to maintain low-noise sideband generation. We have seen already in Fig. 4.11, that seed power has an impact on the strength of the generated sideband and here we observe its importance in relation to the noise. We identify that, for the length of fibre used, the lowest noise is achieved with a pump power of 650 mW combined with the maximum available seed power of 30 mW. The measured standard deviation is 3.5 %, which is corresponds to an addition of 2.1 % to the amplitude noise level measured for the pump pulses before the fibre (1.4 %). This combination is seen also to exhibit the highest intensity of sideband power. It is possible that a shorter length of fibre may have enabled the generation of a similarly intense idler field, with comparable noise although this would

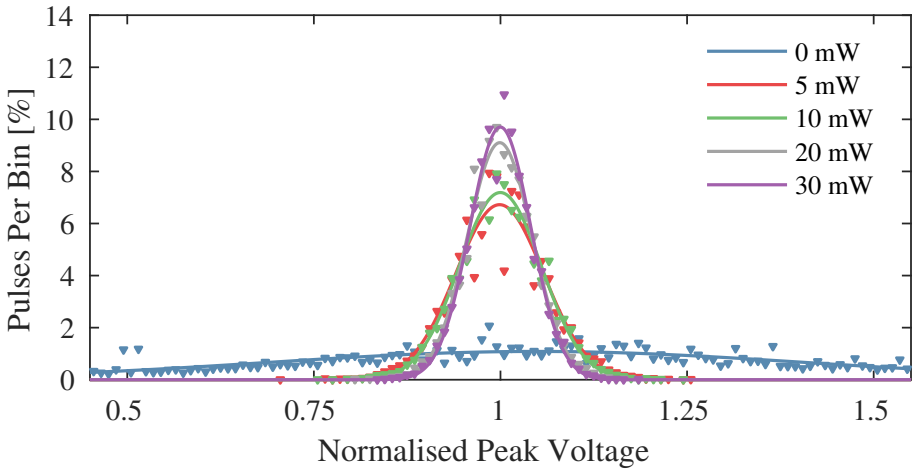

(a) Pump power of 600 mW.

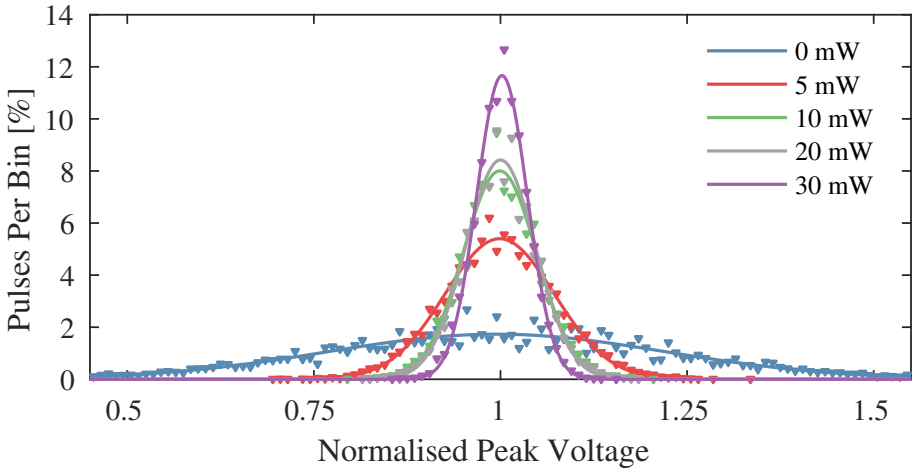

(b) Pump power of 650 mW.

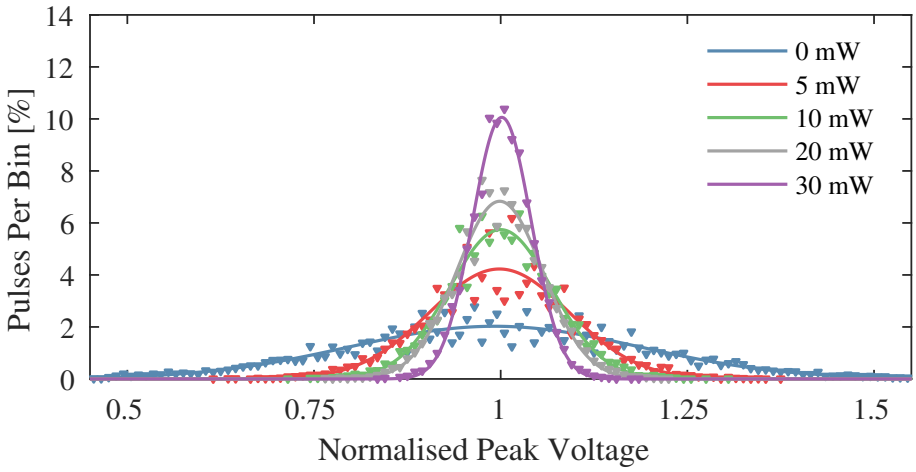

(c) Pump power of 700 mW.

Figure 4.12 Distributions of pulse energy in FWM idler pulses. Lines show the least-square Gaussian fits.

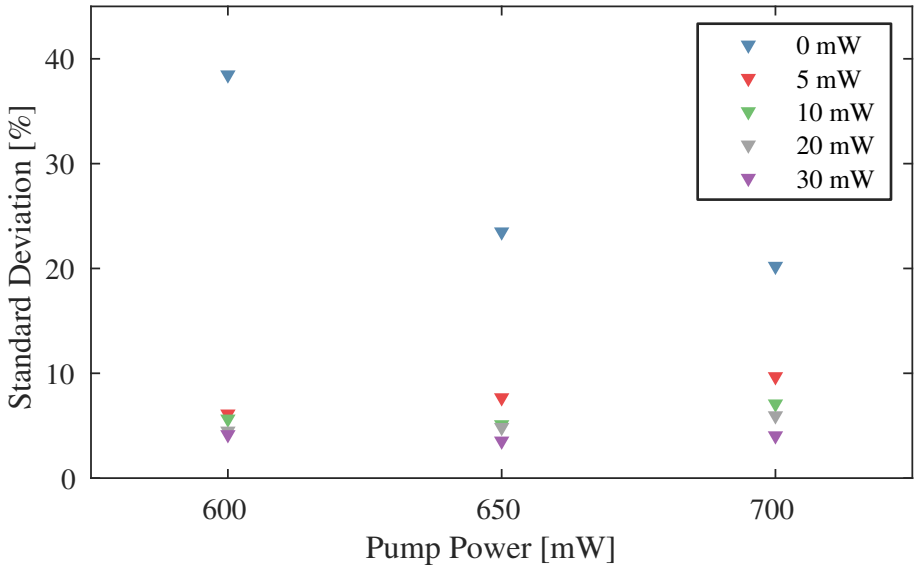

Figure 4.13 The standard deviations of Gaussian fits to the normalised pulse-energy distributions of the idler.

probably require a higher power seed laser than is available, as well as the use of a higher fraction of the available pump power.

The noise measurements presented above demonstrate that the sidebands generated using seeded FWM can be remarkably stable, with no significant increase in pulse-to-pulse amplitude noise over that of the pulse train emitted by the original pump laser. It is typically the case however, that the residual field at the original pump wavelength will be degraded by the nonlinear interaction. Figure 4.14 shows the degradation of the noise in the pump, i.e. the ratio between the standard deviations in normalised pulse energy measured before and after the PCF. We see that in the spontaneous FWM, the largest degradation occurs at the highest pump power, which is to be expected as the nonlinear effects begin to dominate. Introducing a small amount of seed power makes the FWM interaction more deterministic and we observe that the degradation is lessened. However, as the seed strength increases the FWM efficiency increases also and the proportion of the total power which is transferred to the sidebands is far more significant. While the noise in the FWM process is lower, the

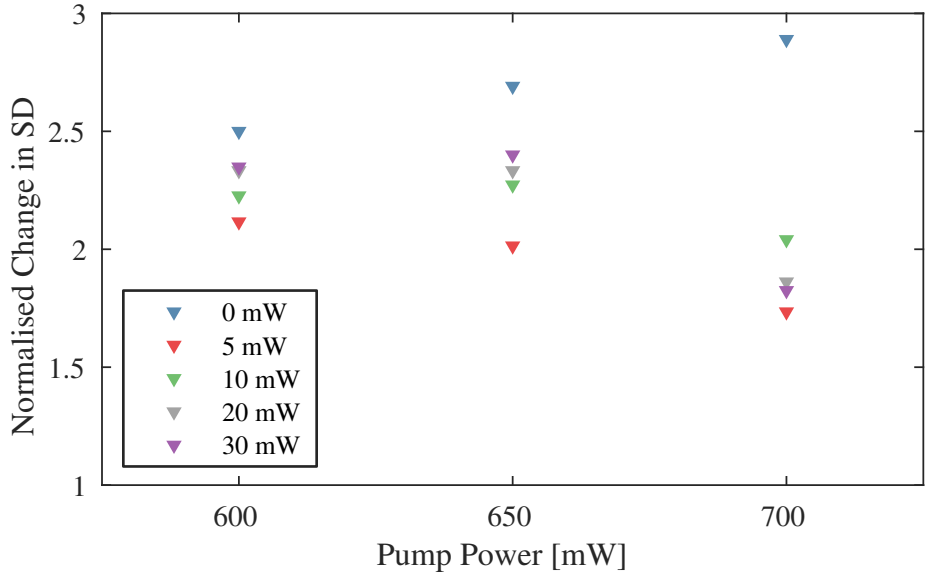

Figure 4.14 Degradation of the noise in the pump field. Values show the difference in standard deviations of Gaussian fits to the normalised pulse-energy distributions of the pump, as measured before and after FWM.

proportionate effect on the pump is larger and we observe higher standard deviations at the upper bounds of seed power, albeit still lower than in the spontaneous regime. At the highest pump power of 700 mW the dynamic interplay between nonlinear effects make the seed-power-dependant degradation of the pump-pulse statistics less clear.

The degradation of the pump field occurs not only in the degree of noise which is introduced, but also in terms of the nonlinear broadening caused by SPM and the dispersive walk off from the idler pulse. It is more convenient therefore to allow only the idler field to carry forward to to the BS-FWM conversion and obtain the necessary light at the original pump wavelength from a discarded portion of the beam ahead of the first fibre. This ensures that these pulses will have the most idealised spectral shape as well as the minimal pulse-to-pulse amplitude noise.

4.3 The frequency converter

4.3.1 Up-conversion: 1530 nm to 1092 nm

Since BS-FWM is unitary and in general may operate in either frequency direction, it is equally valid to consider either the up- or down-conversion process. The availability of wavelength-tuneable laser diodes at telecommunication wavelengths make it convenient to first examine the up-conversion process. As was stated in Section 4.2 however, the experimentally-examined wavelengths differ from the design presented in Chapter 3. For the measurements presented within this chapter, the pump wavelengths which are used each vary by <1 nm and are centred at ∼777 nm and ∼977 nm — the targeted conversion therefore exists between 1092 nm and $\gtrsim$1530 nm. Nonetheless, this conversion still embodies the successful translation of light between the strontium $D_{3/2} \rightarrow P_{1/2}$ emission wavelength and the telecommunication C band.

We characterise the BS-FWM using the experimental setup depicted in Fig. 4.15; the beam emanating from the Ti:Sapphire laser is separated in to two arms ahead of the seeded FWM source, with the subtracted light at 777 nm being recombined with the generated 977-nm sideband at a dichroic mirror following the 4-f spectral filter. A motorised translation stage is used to adjust the OPD between the two arms to temporally overlap the pulses and a Keplerian telescope adjusts the beam diameter of the 777-nm pump. The combined pump beams are then mixed at a DM with a light from a fibre-coupled sub-100-KHz-linewidth laser (ID Photonics CoBrite DX1), which is wavelength tuneable around the telecommunication C band. The three input fields are then directed towards PCF 2. The aspheric coupling lens is selected to maximise the coupling efficiency of the 977-nm-pump light, although this is chosen in combination with the collimating lenses for the fibre-coupled C-band laser and PCF 1, and the lenses of the Keplerian telescope, to maximise the overall coupling efficiency for all of the fields. The output end of PCF 2 is inserted in to a bare-fibre adaptor (BFA)

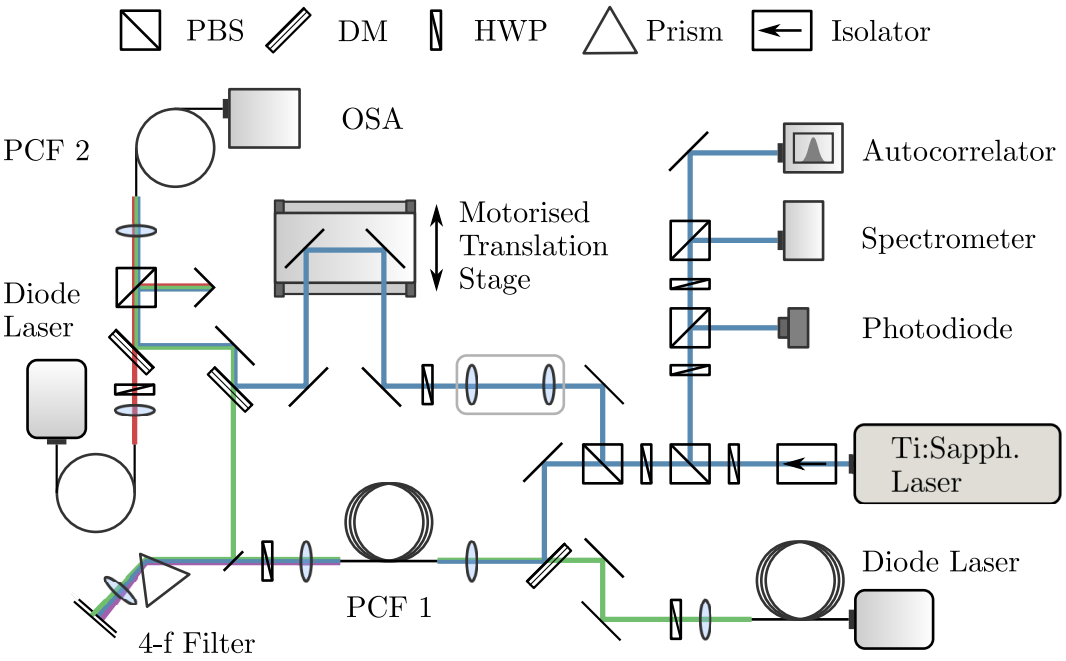

Figure 4.15 Schematic showing the experimental setup for characterising the BS-FWM up-conversion in PCF 2. The 777-nm pump light (shown in blue) from the Ti:Sapphire laser is divided in to two arms using a HWP and PBS. The transmitted PBS output is combined with 977-nm seed light (shown in green) using a dichroic mirror, then coupled into PCF 1. A 4-f prism filter at the output of PCF 1 reflects the generated idler field towards PCF 2. The reflected PBS output is sent through a variable free-space delay arm and then combined with the 977-nm idler pulses. These beams are combined with telecommunication-wavelength laser light (shown in red) and then coupled in to PCF 2. The BS-FWM output of PCF 2 is measured with and OSA. The pump laser pulses are monitored with an autocorrelator and a photodiode. Polarisation of all the fields are set using HWPs.

and connected to either an OSA (Yokogawa AQ6374) or a power meter. In principle the Ti:Sapphire laser retains the flexibility to operate across a small range of pulse durations, although for the reason of mode stability our measurements are made with the laser operating at approximately 11-13 ps throughout the remainder of this thesis.

An example of the spectra we obtain is shown in Fig. 4.16, in which the blue trace shows the two pumps and associated noise at the output of the fibre when the input 1530-nm beam is blocked. The red trace, which is overlaid, depicts also the input light at telecom wavelength and the converted portion of this light centred at 1092 nm. In the experiment there is only a small percentage of the CW input field that is overlapped by the pulsed

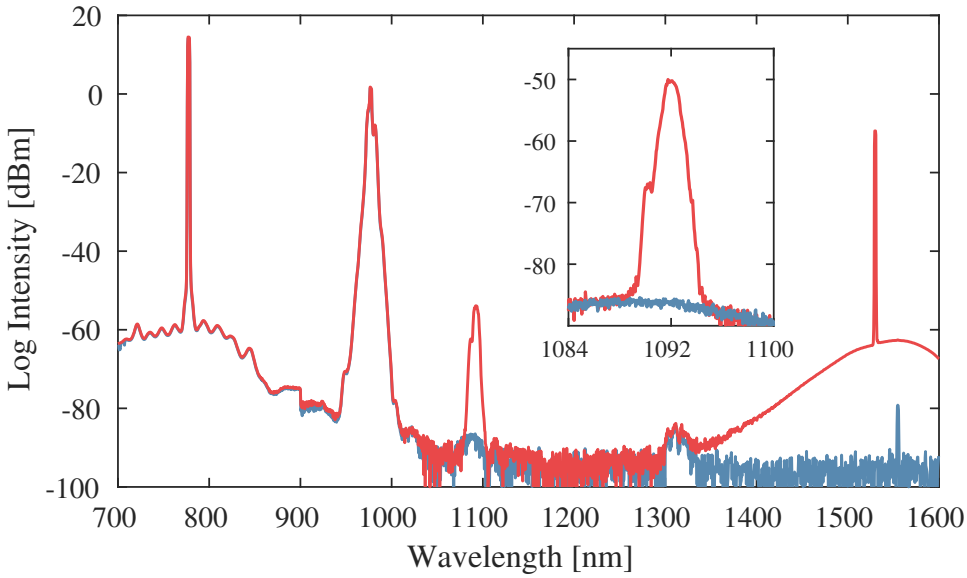

Figure 4.16 Spectra from a 1-m length of PCF 2 with pump powers of 125 mW 12.5 mW at 777 nm and 977 nm, respectively. The spectral resolution is 2 nm. Inset: the converted light around 1092 nm measured with a resolution of 1 nm.

pumps such that, even with relatively high conversion efficiency, the converted light appears at a far reduced amplitude by comparison with the OSA spectra. In considering Fig 4.16, we observe also a number of spurious noise processes, most notably the phase modulation of the pumps, but also a diminished peak around 1316 nm which arises due to non-phase-matched FWM which is seeded by the light at 777 nm and pumped by the strong field at 977 nm.

We collect spectra on the OSA and integrate recorded powers at the Source and Target wavelengths to measure the BS-FWM conversion efficiency, which we record as a function of various input parameters. We calculate the conversion efficiency, η, according to

$$\eta = \frac{(P_{\mathrm{Sr}} - N_{\mathrm{Sr}})\,\omega_{\mathrm{T}}}{P_{\mathrm{T}}\,D\,\omega_{\mathrm{Sr}}}, \tag{4.6}$$

where P_{T} is the integrated power at the input Target wavelength, and the values of P_{Sr} and N_{Sr} are the integrated powers at the Source wavelength with and without the Target input field blocked. The duty cycle, D, is determined by the repetition rate and pulse duration of

the pumps fields and is given by $D = \tau_p R_P$.

We characterise the BS-FWM phase matching in a 1.2-m length of PCF 2 by tuning the

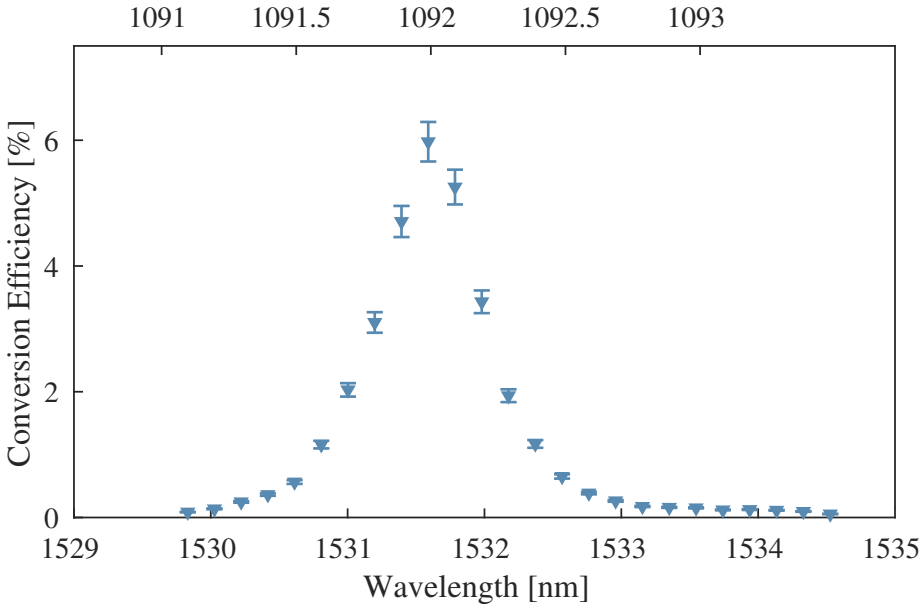

Figure 4.17 The input-wavelength-dependant conversion efficiency of BS-FWM in PCF 2. The lower x axis shows the wavelength of the Target field which was used as the input. The upper x axis indicates the central wavelength of the converted light.

wavelength of the Target input field and recording the resultant conversion efficiency for fixed pump powers of 14 mW at 977.2 nm and 30 mW at 777.5 nm. The results are displayed in Fig. 4.17, in which we observe a phase-matching peak centred at 1531.6 nm which has a FWHM bandwidth of 0.9 nm.

The response of conversion efficiency to a temporal offset between the pump pulses is mapped by measuring the output Source power as a function of optical delay in the 777-nm arm of the experiment. The results are displayed in Fig. 4.18, where values of delay are given in reference to the point of maximum conversion. We observe an asymmetric drop off in the conversion efficiency, which is in accordance with the simulated results in Section 3.3.2. This result also highlights one experimental complexity in building the initial setup — that an OPD between the two pump fields greater than ∼3 mm will eliminate the possibility

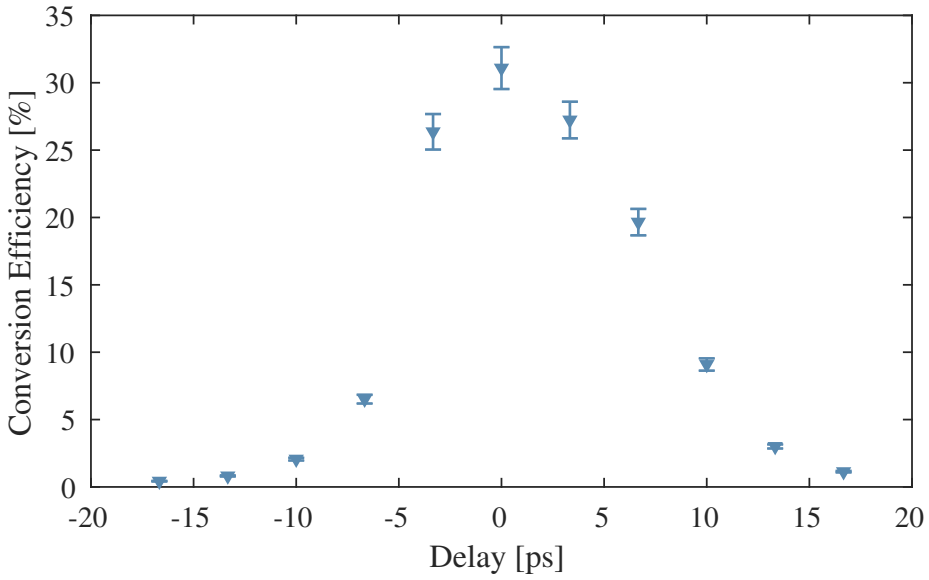

Figure 4.18 The effect of optical delay between pump pulses on the BS-FWM conversion efficiency. The point of highest conversion is denoted as being the point of zero delay, with other values plotted in reference to this position.

to observe any BS-FWM. We note that higher conversion efficiencies displayed in Fig. 4.18 are observed due to the use of higher pump powers: 18 mW at 977.2 nm and 150 mW at 777.5 nm.

The conversion efficiency achieved by BS-FWM is dependant on the length of the medium. If pump-power-induced coupling between the two frequency modes is sufficiently strong a sinusoidal relationship will exist between the length of the fibre and the power at the output wavelength and the nonlinear coupling length will be anti-correlated with pump power. This sinusoidal frequency coupling of light will continue until a length of fibre is reached at which the walk off between pulses in the fibre is sufficiently large and the nonlinear interaction is diminished. However, if the the BS-FWM interaction is of a lower strength then the pulses will likely walk off from each other before the conversion process is completed. In either scenario an asymptotically small portion of the pulses will remain overlapped in time and the BS-FWM interaction will continue to achieve conversion at lengths beyond the defined

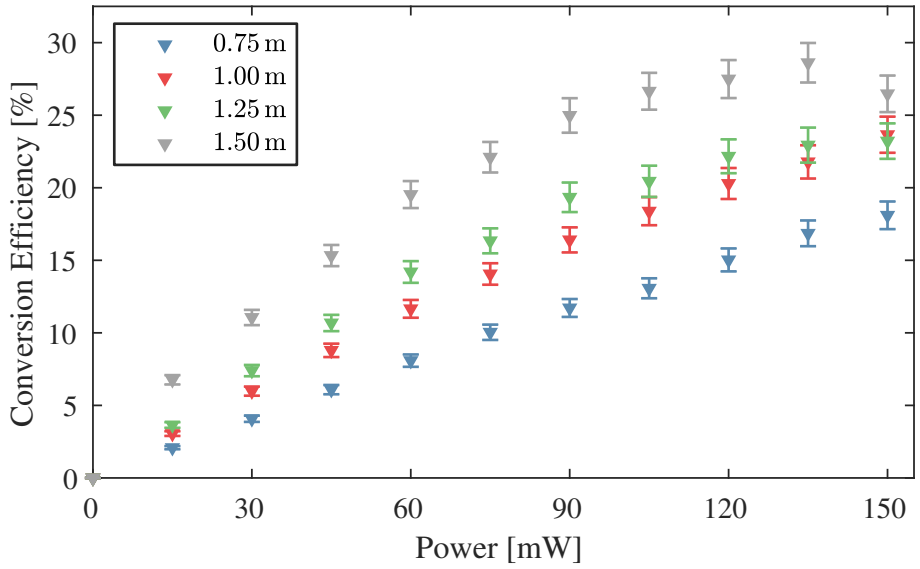

Figure 4.19 The 777-nm-pump-power-dependant conversion efficiency of BS-FWM in four lengths of PCF 2. The efficiencies of the 1.50-m length of fibre are obtained with a a higher average pump power at 977 nm.

walk off length, albeit with vanishingly small impact. In Section 3.3 we evaluated the walk-off length between two 15-ps pump pulses to be approximately 1.4 m, which for the ∼12-ps pump pulses in the experiment reduces to ∼1.1 m. It is important, therefore, to determine an appropriate length of fibre in which the optimal conversion efficiency will be achieved.

We measure the power dependance of the BS-FWM conversion efficiency on the 777-nm-pump for four lengths of PCF 2, the results of which are displayed in Fig. 4.19. The results displayed are obtained for equal average powers of the 977-nm pump (14 mW), with the exception of the data associated with the 1.50-m length of fibre, where a higher power (16 mW) is present. For the fibre lengths of 0.74 m and 1.00 m the conversion is limited by the pump power at 777 nm, but for the two longer lengths of 1.25 m and 1.50 m the conversion efficiency begins to roll off at pump powers in excess of 100 mW. Effectual BS-FWM conversion appears to be occurring up to a length of at least 1.25 m, although the difference in pump powers between measurements make it difficult to determine the effects of the interaction beyond this length.

We repeat the measurement with fibre lengths ranging from 1.25 m to 2.00 m, with the average power of the 977-nm pump coupled in to the fibre maintained at 15±0.5 mW. The

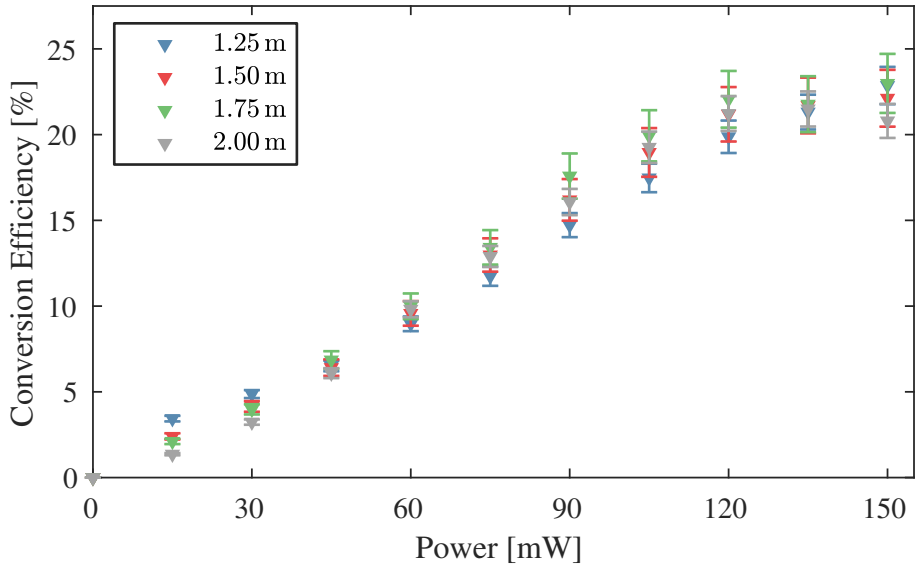

Figure 4.20 The 777-nm-pump-power-dependant conversion efficiency of BS-FWM in four lengths of PCF 2 which exceed the walk-off length for the ∼12-ps pump pulses.

results are displayed in Fig. 4.20, in which we observe little substantial increase in conversion efficiency with length. Using a fibre which exceeds the length for which maximum conversion may be achieved will serve only to introduce additional noise from other nonlinear processes such as cascaded-Raman scattering, which are not dependant on the temporal overlap of the pump fields. By performing a cut-back measurement we determine that a PCF length of 1.2 m is the shortest at which optimal conversion may be achieved.

The maximum conversion efficiency we observe is 37±2%, which is achieved in a 1.2-m length of fibre using average pump powers of 18 mW and 180 mW at 977 nm and 777 nm, respectively. As is apparent from the pump-power-dependant conversion efficiency shown in Fig. 4.21, this efficiency is limited by the power of the pumps. It is likely that, with an improved selection of lenses and with careful alignment, the amount of the available pump power which is coupled in to PCF 2 may be increased; in the conversion reported here,

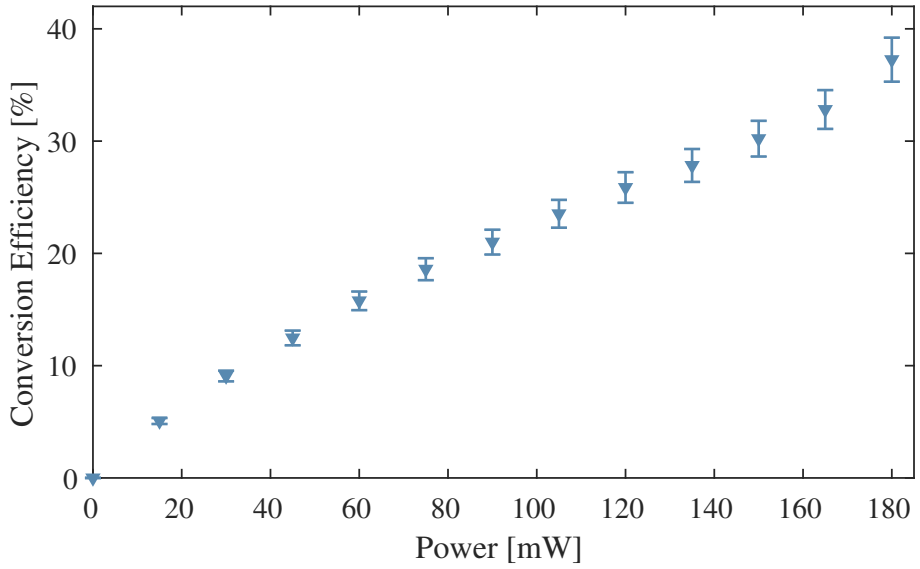

Figure 4.21 The 777-nm-pump-power-dependant conversion efficiency of BS-FWM in a 1.2-m length of PCF 2. The average power of the 977-nm pump is 18 mW.

only ∼40% of the light produced by the seeded FWM in PCF 1 is successfully coupled in to the BS-FWM fibre. With an increase in the power available at 977 nm in particular, a greater conversion efficiency in PCF 2 may be within reach without substantial changes in the experimental configuration being necessitated.

4.3.2 Down-conversion: 1092 nm to 1530 nm

Few commercial laser diodes are wavelength tuneable to 1092 nm, which introduces further complexity when characterising the BS-FWM down conversion. It is necessary for us to construct an external-cavity diode laser (ECDL) to serve as an input field at the Source wavelength. Figure 4.22(a) shows a schematic of the constructed 1092-nm ECDL. Optical gain is provided by a gallium arsenide gain chip with a tuning range from 960 to 1100 nm (Eagleyard Photonics); the gain chip is positioned in a mount with an integrated controller and thermoelectric cooler (TEC). An aspheric lens collimates the optical output of the gain chip and an echelette diffraction grating is positioned in the Littrow configuration so that

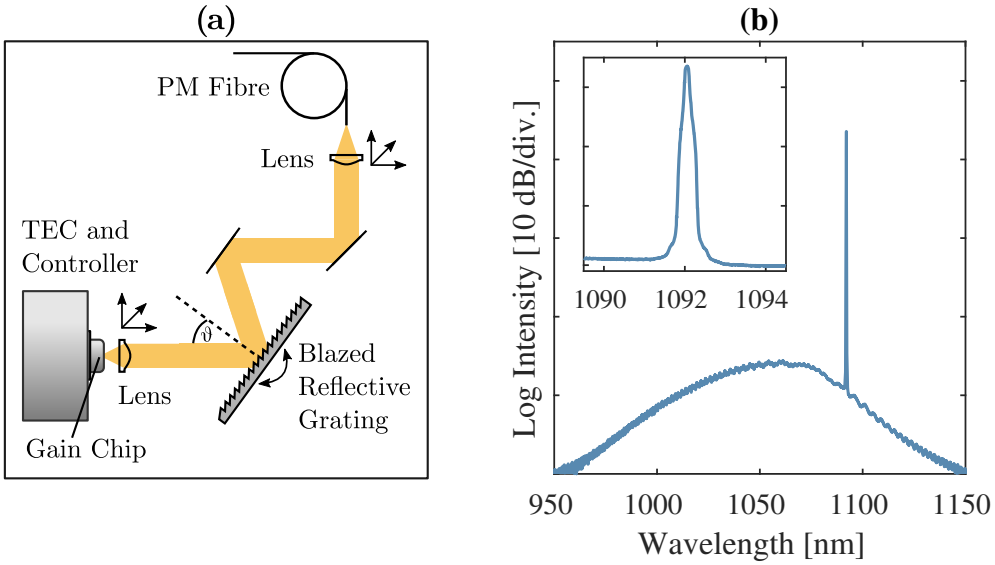

Figure 4.22 The 1092-nm ECDL source for characterising the BS-FWM down-conversion. (a) Littrow-configuration ECDL setup. (b) Optical-power spectra of the ECDL recorded with a resolution of 0.1 nm. Inset: 1092-nm peak measured with a resolution of 0.05 nm.

the first-order diffraction is retroreflected back in to the gain chip to establish a cavity and the zeroth-order diffraction is directed towards a polarisation-maintaning (PM) fibre output. Such a configuration allows for generation of a single-frequency emission which is tuneable with the orientation of the grating, although in adjusting the grating the angle at which the zeroth-order output is directed also changes, compromising the optical alignment after the grating. We obtain an average power variable up to $\geq$25 mW at the fibre output, with a narrow spectral linewidth as shown in Fig. 4.22(b), which is measured on an OSA at a resolution of 0.05 nm.

The experimental setup for the down-conversion measurement is almost identical to that for the up-conversion discussed in Section 4.3.1, with the exception of ECDL being used in place of the telecommunication-wavelength laser; the modified setup is shown in Fig. 4.23.

If BS-FWM is achieved using only CW fields then the process may be considered to have near identical behaviour in either up- or down-conversion, with the exception that the sign of the phase-matching equation, Eq. 3.24 will change. However, the difference in

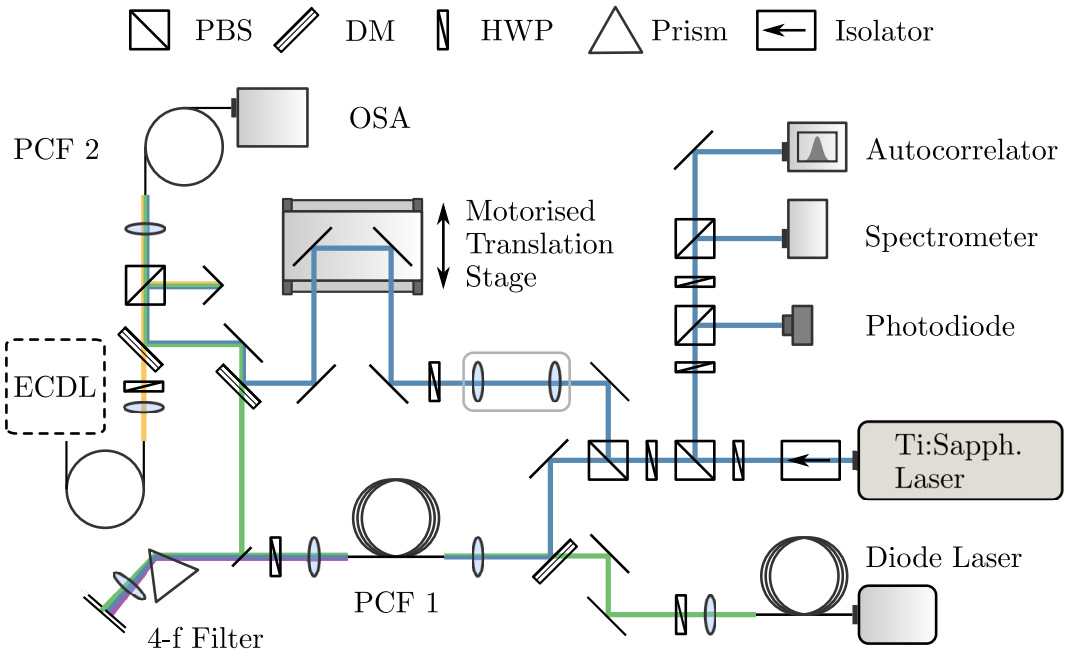

Figure 4.23 Experimental setup for characterising the BS-FWM down-conversion in PCF 2. The 777-nm pump light (shown in blue) from the Ti:Sapphire laser is divided in to two arms using a HWP and PBS. The transmitted PBS output is combined with 977-nm seed light (shown in green) using a dichroic mirror, then coupled into PCF 1. A 4-f prism filter at the output of PCF 1 reflects the generated idler field towards PCF 2. The reflected PBS output is sent through a variable free-space delay arm and then combined with the 977-nm idler pulses. These beams are combined with 1092-nm light from the ECDL (shown in yellow) and then coupled in to PCF 2. The BS-FWM output of PCF 2 is measured with and OSA. The pump laser pulses are monitored with an autocorrelator and a photodiode. Polarisation of all the fields are set using HWPs.

the relative group velocities of optical pulses at different wavelengths mean this assumption is not necessarily true for the experiment presented here. Nonetheless, we expect similar conversion efficiency to be obtainable using the input parameters employed in Section 4.3.1 for the up-conversion process.

We collect spectra on the OSA and integrate recorded powers at the Source and Target wavelengths to measure the BS-FWM conversion efficiency, which is calculated as

$$\eta = \frac{(P_{\mathrm{T}} - N_{\mathrm{T}})\,\omega_{\mathrm{Sr}}}{P_{\mathrm{Sr}}\,D\,\omega_{\mathrm{T}}}. \tag{4.7}$$

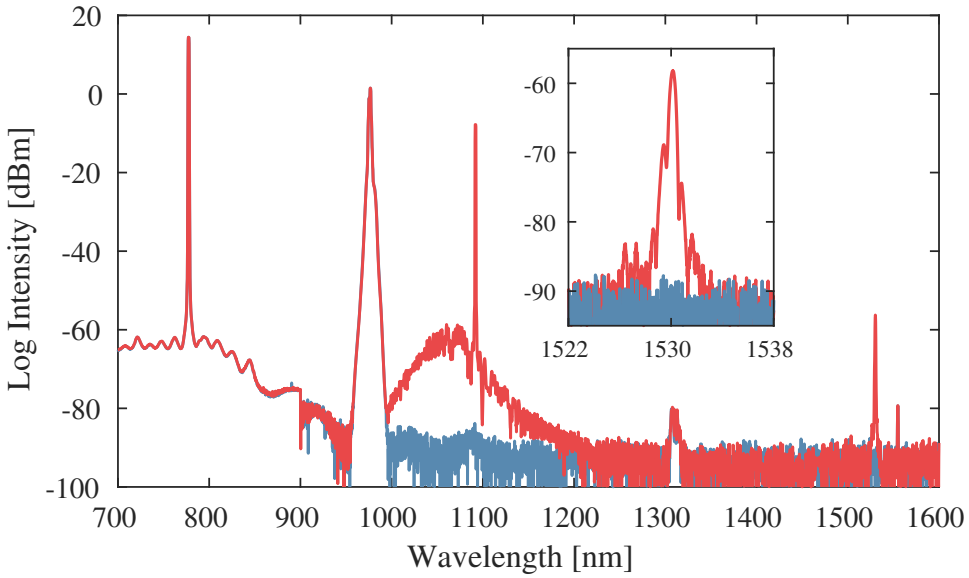

Figure 4.24 Spectra from a 1.2-m length of PCF 2 with pump powers of 180 mW and 14.5 mW at 777 nm and 977 nm, respectively. The spectral resolution is 2 nm. Inset: the converted light around 1530 nm measured with a resolution of 1 nm.

Figure 4.24 shows spectra which are obtained on the OSA when the pump powers are 145 mW and 14.5 mW at 777 nm and 977 nm, respectively. The blue trace shows the two pumps and associated noise at the output of the fibre when the input beam is blocked. The red trace, which is overlaid, records also the input light at 1092 nm and the converted portion of this light centred at 1530 nm.

The measurements which are obtained for BS-FWM down-conversion indicate a lower conversion efficiency than is seen for the reciprocal up-conversion process. The 777-nm-pump-power-dependant conversion efficiency is shown in Fig. 4.25, in which we observe a maximum conversion efficiency of 4.2±0.3%. The 777-nm-pump power at which this conversion is observed is higher than that used in the up-conversion experiment, whilst the power in the 977-nm pump is reasonably consistent at 17.5 mW. Similar to the power-dependant up-conversion shown in Fig. 4.21, no roll off in the efficiency at higher power occurs, indicating the availability of more pump power would likely increase the performance of the

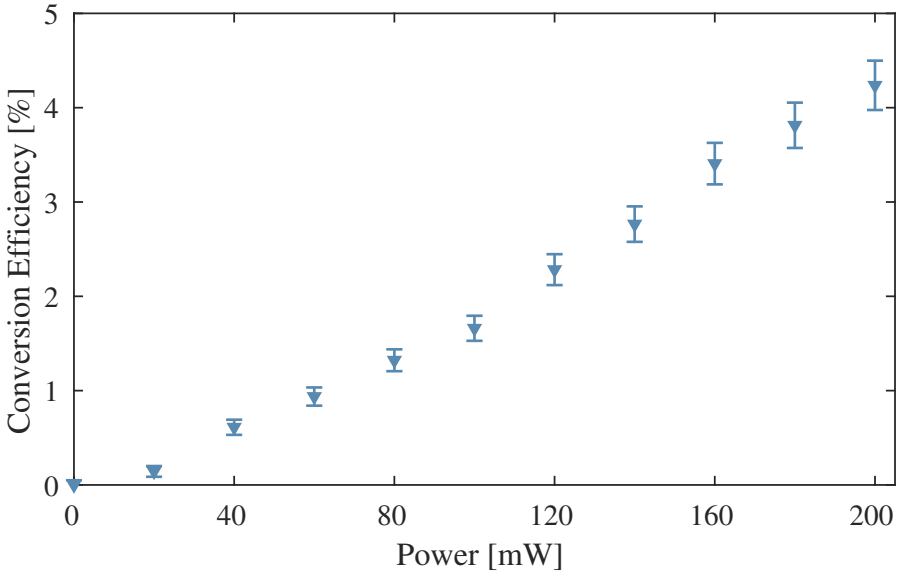

Figure 4.25 The 777-nm-pump-power-dependant conversion efficiency of BS-FWM down-conversion in a 1.2-m length of PCF 2. The average power of the 977-nm pump is 17 mW.

conversion. However, the pump powers coupled in to the fibre are similar enough that we must surmise that the BS-FWM is limited in some other way.

To obtain the results plotted in Fig. 4.25 we first adjust the optical delay between the pumps whilst monitoring the power level at the target wavelength. Furthermore, we adjust the temperature of the DBR-diode laser used to seed the FWM in PCF 1 to shift the wavelength of 977-nm pump, thereby minimising the phase-mismatch of the BS-FWM process. In this way we have ensured that the temporal offset between the pumps and the phase-matching are not unduly limiting conversion. A number of possibilities remain. Firstly, that the greater presence of noise photons at the Source wavelength around 1092 nm is sufficient to stimulate the BS-FWM from 1550 nm in the up-conversion and boost the efficiency of conversion in that direction. The absence of such noise at the Target wavelength indicates that this effect, if at all significant, would be diminished in the down-conversion interaction. The linewidth of the telecommunication laser used to assess the up-conversion is <100 KHz, whereas the linewidth of the ECDL we use to investigate down-conversion is unknown, al-

though is anticipated to be $\mathcal{O}(1\,\mathrm{MHz})$. It is possible that the difference in the linewidth of the input fields has some effect on the conversion, although we have no evidence to support this. Finally, it may be the case that in switching to the down conversion operation the annihilation of pump photons is applied to the weaker of the two pumps, and that this also reduces the rate at which Source photons are translated to the Target wavelength. If this is a contributing factor then carrying forward the short wavelength sideband from PCF 1 to use as BS-FWM pump would be an appropriate strategy to increase the efficiency of the conversion, although an alternate fibre would be needed to use in place of PCF 2.

4.3.3 Projected noise

The absence of a suitable source of photons and appropriate optical filters limits our capability to enact single-photon level frequency conversion of either quantum or coherent states. However, we are able to use the measured conversion efficiencies together with a simplified noise-characterisation setup to indicate the expected performance of the BS-FWM device;

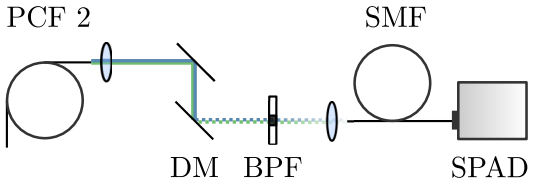

Figure 4.26 Schematic showing the experimental setup which is used to investigate the expected noise levels for BS-FWM conversion of single-photon-level light. A dichroic mirror and band-pass filter are positioned after PCF 2 and noise photons generated by the BS-FWM are counted using a fibre-coupled SPAD.

the setup is depicted in Fig. 4.26. We couple 0.5 mW of CW light at 1530 nm in to PCF 2, as well as 180 mW of pump light at 777-nm and 18 mW at 977 nm, thus reproducing the conditions at which maximum up-conversion was achieved. At the output of PCF 2 we collimate the three fields and direct them towards a fibre-coupled SPAD (ID Quantique, ID210), but also apply filtering through the use of a 1064-nm-edge long-pass DM and a 10-nm-bandwidth

BPF centred at 1550 nm. Prior to connecting the SMF to the SPAD we optimise coupling of the light at 1530 nm to 55 % and then, with optimal coupling achieved, block the 1530-nm light. The fibre is connected to the SPAD and we record detector counts resulting from the noise associated with the two BS-FWM pumps.

We calculate two values of μ_1, the lowest photon numbers per pulse which would achieve SNR = 1, using the recorded conversion efficiencies, η_{BS}, of 37% and 4.2%. While this experimental setup is appropriate only for assessing noise associated with BS-FWM down conversion, the achievable efficiencies of both up- and down-conversion should, in principal, be the same. Calculating a value for μ_1 based on the value of η_{BS} which is obtained in the up-conversion experiment should, therefore, provide some lower bound on the value of μ_1 which might yet be achieved with experiment is the presented form. In calculating μ_1, we use dead-time corrected count rates, N, and account for losses associated with the fibre-coupling efficiency, η_{Coupling}, (55%) and detector efficiency, η_{Det}, (10%):

$$\mu_1 = \frac{N}{R_{\mathrm{P}}\,\eta_{\mathrm{BS}}\,\eta_{\mathrm{Coupling}}\eta_{\mathrm{Det}}}. \tag{4.8}$$

We obtain values of 0.0827 and 0.7323, which indicates that, if the higher rate of conversion can be replicated in both directions, then the process will be of sufficiently low noise to remain applicable to quantum networks. The filtering we employ is also not extensive and could easily be supplemented for use in real-world operation.

4.4 Summary and outlook

In addition to implementing large-scale frequency remapping between blue and IR wavelengths, it is possible hybrid-light matter networks will require smaller scale frequency shifts to facilitate low-loss connections between nodes operating within the NIR region. In such circumstances $\chi^{(3)}$ based frequency conversion schemes are far more practical to employ due

to relaxed energy requirements of the pump fields (this being that the frequency shift enacted by the conversion must be matched by the difference in frequencies of the pumps). However, $\chi^{(3)}$ nonlinear processes require two pump fields, a role which has almost exclusively been played by a pair of repetition-rate-locked high-power pulsed lasers in previous experiments. Using only a single pulsed laser system, we have implemented a resource-efficient frequency conversion scheme capable of up- and down-conversion of light between a NIR Sr^+ emission wavelength and the telecommunication C band. Bespoke micro-structured optical fibres were fabricated to phase match a degenerate FWM process from which we obtain a second pump field, as well as a BS-FWM process in which we demonstrated up- and down-conversion between 1092 nm and 1530 nm. Presently, our device operates with conversion efficiencies of 4.2% and 37% in up- and down-conversion, respectively. We have identified that the conversion efficiency in both directions is limited by power, especially at the pump wavelength which is generated through seeded FWM.

To emphasise the significance of the reported conversions it is useful to present these numbers in conjunction with values of attenuation in fibre which we are seeking to minimise. In Fig. 4.27, we show the expected impact on photon transmission across a large-scale quantum network resulting from BS-FWM conversion from 1092 nm to 1530 nm at 4.2% efficiency, but also at the 37% efficiency that we expect may yet be achieved. The losses of single mode fibres at 1092 nm (HI1060) and 1530 nm (SMF28) are $\leq 2\,\mathrm{dB\,km^{-1}}$ and $\leq 0.18\,\mathrm{dB\,km^{-1}}$, respectively. The difference in the attenuation are such that if 37% efficient down-conversion were to be achieved, a transmission enhancement could be expected at separations greater than 2.4 km. At 4.2% efficient conversion the enhancement would be observed at separations in excess of 7.6 km.

In the presented work, picosecond-duration pulses are used to characterise the experiment, but for operation which is compatible with a trapped ion system, the use of nanosecond pulses is necessary. In the previous chapter, in Section 3.3.2, we presented the results of nu-

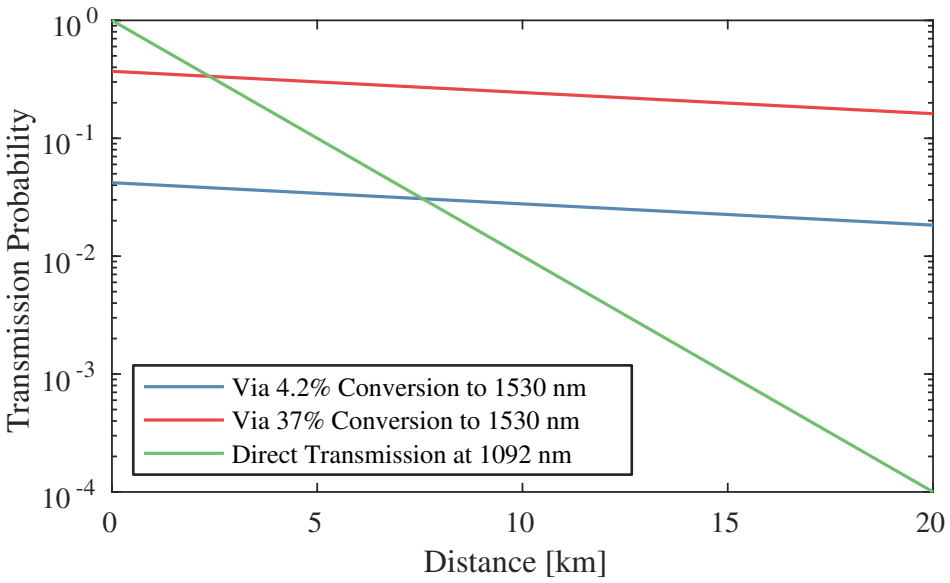

Figure 4.27 Impact on transmission probability of 1092-nm photons through optical fibre if first converted to 1530 nm.

merical simulations which showed that the scaling of the BS-FWM experiment between the picosecond and nanosecond regime would have no detrimental effect on the conversion, so long as the peak power of the pump pulses remains constant. If the peak powers were equal to those used in the presented work, a slightly longer length of PCF 2 could be used to enable the peak conversion to be reached, as in this regime walk-off length between pulses in the fibre would be orders of magnitude shorter than the BS-FWM coupling length. If higher peak powers were available, peak conversion could easily be achieved in lengths of PCF 2 equal or to or less than those used here. In addition to this, it is likely that an implementation of the presented FWM scheme using longer pulse durations would result in enhanced parametric sideband production in the first fibre; the use of longer pulses with narrower bandwidths would permit the use of longer lengths of PCF 1 and accordingly sidebands which are closer to being transform limited. The use of narrow-bandwidth transform-limited pump pulses for the BS-FWM, which would better match the properties of the input field, is certain to improve the conversion efficiency of the interaction.

There are also potential improvements to this setup which may come from additional consideration of the PCF designs. The first fibre, in which we implement the seeded FWM, possesses a uniform cladding structure. A result of this structure is that the fibre is not polarisation maintaining – while linearly polarised fields are coupled into the PCF, the output is in a partially mixed state. As a result of this mixed state, the amount of 977-nm light which is coupled into PCF 2 is ∼20% less (after polarisation filtering) than what might otherwise be achievable. In regards to PCF 2, it is likely that the design of a fibre which implements BS-FWM using pumps from the two shorter-wavelength fields of ∼640 nm and 777 nm will result in a reduction of noise photons being present at the Source and Target wavelengths. Furthermore in developing such a PCF additional care could be introduced to minimise the $\beta_1(\omega)$ mismatch between the four fields so to mitigate the effects temporal walk-off between pulses, and therefore potentially extend the BS-FWM interaction. In exploring these avenues it is likely that the reasons for discrepancy in the up- and down-conversion efficiencies will be revealed.

Beyond these considerations it is also critical that conversion be examined using single-photon-level coherent and quantum states of light to ensure that the scheme is quantum-network ready, both in terms of spurious noise, but also in the conservation of quantum states, for which polarisation stability might also become important.

Chapter 5

Conclusion

5.1 Summary

In Chapter 1, the motivation for developing quantum networks was presented. We discussed the necessity of photonic hardware within these networks and the important role that frequency conversion has to play. In particular one proposed quantum network, the Q20:20 machine, was highlighted and the specific requirements of frequency conversion for this network detailed. Chapter 2 presented the first of two bodies of work we have undertaken in addressing these requirements: a two-way photonic interface for linking the Sr^+ transition at 422 nm to the telecommunication C band was presented. The frequency-conversion interface was based on second-order nonlinear optical effects and so Chapter 2 also included an introduction to the theory of $\chi^{(2)}$ processes and the specific challenges associated with achieving such a large frequency shift – presently the shortest wavelength translated directly to the telecommunication C band. The custom MgO:PPLN device operated with conversion efficiencies of 9.4% and 1.1%, respectively, and identified potential routes through which to improve this performance. While these numbers may appear small, the impact is not. A discussion is presented in which the potential enhancement to a quantum networks was

imagined: when considering the transmission loss of a single-mode fibre at the Sr^+ emission wavelength of 422 nm relative to that at 1550 nm, our interface would increase the probability of establishing entanglement between remote ion traps by 47 orders of magnitude over a distance of 10 km.

In Chapter 3 we moved the discussion forward to third-order nonlinear phenomena, which serve as far more flexible processes through which to achieved frequency conversion over smaller spectral windows. The theoretical discussion continued to examine frequency conversion via four-wave mixing and presented the results of numerical simulations used to reveal the dynamic behaviour of pulsed light conversion in this regime. Principally, a resource-efficient frequency conversion scheme between the Sr^+ transition at 1092 nm and the telecommunication C band was presented, addressing another potential requirement of the Q20:20 engine. Chapter 4 details the experimental realisation of the four-wave-mixing conversion proposed in Chapter 3. The fabrication and characterisation of bespoke microstructured optical fibres in which we engineered the generation of pump light and conversion processes was documented in the first half of this chapter. In the second half of the chapter, the construction and analysis of the bright-light seeded-FWM source was discussed and its position within the larger BS-FWM frequency-conversion experiment realised. We presented a thorough analysis of the $\chi^{(3)}$ conversion scheme and showed operation in both up- and down-conversion, with peak conversion efficiencies of $4.2\pm0.3\%$ and $37\pm2\%$, respectively. A discussion entailed on realistic changes to the experimental implementation which might lead to performance enhancements.

5.2 Outlook and future work

Section 2.3 detailed strategies which may be applied to enhancing the $\chi^{(2)}$ conversion between 422 nm and the telecommunication C band. The foremost amongst these would be to make use of a $LiNbO_3$ waveguide to enhance the conversion process. Recent advances in

manufacturing techniques are allowing for shorter and shorter poling lengths in $LiNbO_3$, unlocking the full phase-matching potential of the medium: applying these poling capabilities in conjunction with the capability to produce high-quality waveguides is an unmistakeable way forward.

In Section 4.4 we outline strait forward ways in which resource-efficient $\chi^{(3)}$ conversion between 1092 nm and the telecommunication C band might be improved. Presently the experiment is hindered by a non-optimal pulse duration of the Ti:Sapphire laser, although to be relevant to a realised quantum network it would be necessary to consider using a different principal laser system all-together, not least to ensure compatibility with the temporal properties of photons emitted from the trapped-ion nodes. To this end, it is essential that future work pushes forward in the transition towards using laser systems with longer pulse durations, with the stipulation that this does not necessarily have to preclude the possibility of bright-light pulse generation useful for the generation of an ancillary pump field.

To expand on how the resource-efficient $\chi^{(3)}$ frequency conversion may be further developed to work with a trapped ion system, let us consider the following. To achieve high-visibility Hong-Ou-Mandel interference between photons emitted from trapped ions, there are temporal, spectral and polarisation-stability requirements which need to be met by a frequency conversion interface. By adapting the BS-FWM experiment to operate in the nanosecond regime, the first two of these requirements would be possible to fulfil, but is such a transition realistically achievable? In order to maintain the BS-FWM conversion efficiency when shifting from the picosecond to nanosecond regime, it is preferable that the available peak powers of the pump pulses remain the same. If this is the case, then the strength of the nonlinear coupling of the input field from one frequency mode to another will be unaffected and occur over the same length scales, permitting similar lengths of fibre to be used. While it would be possible to use longer lengths of fibre, as the walk-off lengths for the pulses would be three orders of magnitude larger, optical losses along the fibre length

make it preferable to use as little as possible. It would be ideal, therefore, to employ a laser system with pulse durations which are three orders of magnitude longer, but also with pulse energies that are three orders of magnitude higher, than the pulses generated by the Ti:Sapphire laser we employ. One such laser system which meets this criteria is the Sirah Credo Ti:Sapphire laser; Table 5.1 shows a comparison of the specifications of this laser and the Spectra Tsunami system which was used in the FWM experiments presented within this thesis. In the BS-FWM experiment, approximately 0.54 kW of the Tsunami's total 2.4 kW

Laser System	Tuning Range	Avg. Power	Pulse Duration	Rep. Rate	Peak Power
Spectra Tsunami	700 - 1000 nm	>2.9 W	10 - 20 ps	80 MHz	∼2.4 kW
Sirah Credo	690 - 950 nm	<6.8 W	28 - 50 ns	10 KHz	∼23 kW

Table 5.1 Specifications for two Ti:Sapphire pulsed laser systems. The values shown for the Spectra Tsunami are representative of the Tsunami's configuration as used in the resource-efficient BS-FWM experiment. The values for maximum output peak power are calculated using pulse durations of 15 ps and 30 ns for the Tsunami and Credo, respectively.

of available peak power is coupled in to PCF 1 to pump the seeded FWM process. Furthermore, a maximum of 0.17 kW is required for the BS-FWM interaction in PCF 2. If we assume that losses from optical components and coupling efficiencies to be ∼50 %, then the total peak power requirement is ∼1.4 kW, which is less than 10 % of what could be provided by a Sirah Credo laser operating with a pulse duration of 30 ns. Permitting the use of longer lengths of fibre, this power requirement could be reduced further. However, the repetition rate of the Sirah Credo is only 10 kHz, which would limit the frequency convertor to a far lower clock speed. Recently a research group within NQIT has demonstrated high-rate, high-fidelity entanglement of two $^{88}Sr^{+}$ ions across an elementary quantum network [74]. In this experiment a photon-photon entanglement rate of $182\,s^{-1}$ was achieved, although as the total success probability was only 2.18×10^{-4}, the attempt rate was 833 kHz. The main factor limiting the entanglement success probability was that the individual probability of detecting a photon emitted from either ion trap was about 2 %, resulting from the use of avalanche photodiodes with low detection efficiencies. It is not unreasonable to imagine

future experiments, that use higher-efficiency detectors, could be operated using ion traps clock rates limited to about 10 kHz. For higher clock rates it is possible that, because of the excess availability of pump power from a system such as the Sirah Credo, the output of the pulsed laser could be divided and passed through the optical delay arm of a static asymmetric Mach-Zehnder interferometer, each time doubling the repetition rate. Such an approach could be similar in setup to an experiment which was used to suppress amplitude noise from a fibre laser [111].

The requirement for quantum frequency conversion interfaces to ensure good polarisation stability could be met by using birefringent PCFs. In fact, further exploring the use of micro-structured optical fibres presents a wealth of opportunity when it comes to engineering $\chi^{(3)}$ processes for frequency conversion. Hybrid fibres, for example, provide an opportunity to simultaneously phase match a nonlinear process whilst suppressing noise [112]. However, the dispersion control offered by PCFs, even in designs similar to the designs presented in this thesis, may yet offer further advances in frequency-conversion capabilities. It is maybe possible to design the dispersion of a PCF to allow for a phase-matched BS-FWM, but with a specific intent to mitigate temporal walk-off. Furthermore, an additional opportunity exists resulting from the careful control over group-velocity in PCF: a PCF in which $\beta_1(\omega)$ is symmetric in frequency about the zero-dispersion wavelength will allow for broad-band phase matching, i.e. any BS-FWM process which is centred around this central frequency will automatically be phase matched. Implementing the design of such a fibre will allow for dynamic tuning of BS-FWM conversion in the lab.

Appendix A

PCF Fabrication Recipe

Presented here are the recipes used to fabricate the PCFs used for both the seeded FWM and the BS-FWM conversion discussed in Chapter 4. The details of this fabrication process are given in detail in Section 4.1, the values listed here correspond to the methods and parameters described within that section. Furthermore, the geometric parameters given are generalised to describe nominal sizes, although are still representative of the specific glass used in the work presented within this thesis.

Table A.1 lists the sizes of the commercially-available tubes used. Note that a fused-silica rod is also required from which to draw both the core defect and packing rods needed when assembling the stack, although the initial diameter of this rod is not critical.

	OD_{PCF1} [mm]	ID_{PCF1} [mm]	OD_{PCF2} [mm]	ID_{PCF2} [mm]
Tube for Capillaries	25.0	19.0	25.0	11.0
Cladding Tube	25.0	19.0	25.0	22.0
Jacket Tube	15.0	03.5	10.0	03.5

Table A.1 Sizes of fused-silica tubes used in the fabrication of the PCFs.

Table A.2 specifies the draw down ratios applied to structures during fabrication. These draw-down ratios are defined as the ratio between the initial and final outer-diameter and are given as approximate values, with need for adjustment to allow for the particular geometric

tolerances associated with a specific fused-silica tube. The specific size of the structure at each stage may be easily realised by considering that the assembled Stack is required to fit within the ID of the Cladding Tube and that the Cane is required to fit within the ID of the Jacket Tube.

	PCF 1	PCF 2
Tube to Capillary	16.15	13.85
Stack to Cane	07.35	07.14
Jacketed Cane to Fibre	139.5	72.60

Table A.2 Draw-down ratios used in fabrication of PCF 1 and PCF 2.

Table A.3 contains the parameters used on the fibre drawing tower to obtain the correct PCF structure from the jacketed canes. The parameters used during earlier stages of the fabrication process are less critical, assuming that sufficient tension is maintained to prevent deformation of glass geometry; control over the tension principally achieved by selection of the furnace temperature, although draw and feed rates may be exploited to control the amount of time glass is located in the hot zone of the furnace.

Fibre	Feed [mm/min]	Draw [m/min]	Tension [g]	Temperature [°C]	Pressure [kPa]	Vacuum [kPa]	OD [µm]
PCF1	2.0	25.5	214	1920	8.30	4.00	133.0
PCF2	3.5	17.1	128	1950	11.05	4.00	140.5

Table A.3 Parameters used on the fibre drawing tower to obtain the correct PCF structure from the jacketed canes.

The final pitch and hole size in the PCF cladding structures are given in Table A.4.

Fibre	Pitch [µm]	Hole Size [µm]
PCF1	1.51±0.01	0.96±0.01
PCF2	3.45±0.01	1.57±0.01

Table A.4 Final PCF cladding geometry.

References

[1] A. Einstein, *Concerning an heuristic point of view toward the emission and transformation of light*, Annalen der Physik, **322**, p. 132 (1905).

[2] M. Planck, *On the law of the energy distribution in the normal spectrum*, Annalen der Physik, **309**, p. 553 (1901).

[3] P. A. M. Dirac, *The quantum theory of the emission and absorption of radiation*, Proceedings of the Royal Society of London. Series A, Containing Papers of a Mathematical and Physical Character, **114**, pp. 243–265 (1927).

[4] R. J. Glauber, *The Quantum Theory of Optical Coherence*, Physical Review, **130**, p. 2529 (1963).

[5] J. F. Clauser, *Experimental distinction between the quantum and classical field-theoretic predictions for the photoelectric effect*, Physical Review D, **9**, pp. 853–860 (1974).

[6] H. J. Kimble, M. Dagenais, and L. Mandel, *Photon Antibunching in Resonance Fluorescence*, Physical Review Letters, **39**, p. 691 (1977).

[7] D. F. Walls, *Evidence for the quantum nature of light*, Nature, **280**, pp. 451–454 (1979).

[8] T. H. Maiman, *Stimulated Optical Radiation in Ruby*, Nature, **187**, pp. 493–494 (1960).

[9] D. C. Burnham and D. L. Weinberg, *Observation of Simultaneity in Parametric Production of Optical Photon Pairs*, Physical Review Letters, **25**, p. 84 (1970).

[10] C. K. Hong and L. Mandel, *Experimental realization of a localized one-photon state*, Physical Review Letters, **56**, p. 58 (1986).

[11] A. Einstein, B. Podolsky, and N. Rosen, *Can quantum mechanical description of physical reality be considered complete?*, Physical Review, **47**, pp. 777–780 (1935).

[12] A. Aspect, P. Grangier, and G. Roger, *Experimental Realization of Einstein-Podolsky-Rosen-Bohm Gedankenexperiment: A New Violation of Bell's Inequalities*, Physical Review Letters, **49**, p. 91 (1982).

[13] Z. Y. Ou and L. Mandel, *Violation of Bell's Inequality and Classical Probability in a Two-Photon Correlation Experiment*, Physical Review Letters, **61**, p. 50 (1988).

[14] P. R. Tapster, J. G. Rarity, and P. C. M. Owens, *Violation of Bell's Inequality over 4 km of Optical Fiber*, Physical Review Letters, **73**, p. 1923 (1994).

[15] R. Loudon, *The Quantum Theory of Light*, Clarendon Press, Oxford (1973).

[16] M. Fox, *Quantum optics : an introduction*, Oxford master series in physics. Atomic, optical and laser physics ; 15, Oxford University Press, Oxford (2006).

[17] C. K. Hong, Z. Y. Ou, and L. Mandel, *Measurement of subpicosecond time intervals between two photons by interference*, Physical Review Letters, **59**, pp. 2044–2046 (1987).

[18] M. A. Nielsen and I. L. Chuang, *Quantum Computation and Quantum Information: 10th Anniversary Edition*, Cambridge University Press, New York, NY, USA, 10th edition (2011).

[19] I. Buluta and F. Nori, *Quantum Simulators*, Science, **326**, pp. 108–111 (2009).

[20] J. I. Cirac and P. Zoller, *Goals and opportunities in quantum simulation*, Nature Physics, **8**, pp. 264–266 (2012).

[21] I. M. Georgescu, S. Ashhab, and F. Nori, *Quantum simulation*, Reviews of Modern Physics, **86**, p. 153 (2014).

[22] S. Till and J. Pritchard, *UK quantum technology landscape 2016*, Technical report, London (2016).

[23] H. J. Kimble, *The quantum internet*, Nature, **453**, pp. 1023–1030 (2008).

[24] Q.-C. Sun, Y.-F. Jiang, Y.-L. Mao, L.-X. You, W. Zhang, W.-J. Zhang, X. Jiang, T.-Y. Chen, H. Li, Y.-D. Huang, X.-F. Chen, Z. Wang, J. Fan, Q. Zhang, and J.-W. Pan, *Entanglement swapping over 100km optical fiber with independent entangled photon-pair sources*, Optica, **4**, pp. 1214–5 (2017).

[25] J. Yin, Y. Cao, Y.-H. Li, J.-G. Ren, S.-K. Liao, L. Zhang, W.-Q. Cai, W.-Y. Liu, B. Li, H. Dai, M. Li, Y.-M. Huang, L. Deng, L. Li, Q. Zhang, N.-L. Liu, Y.-A. Chen, C.-Y. Lu, R. Shu, C.-Z. Peng, J.-Y. Wang, and J.-W. Pan, *Satellite-to-Ground Entanglement-Based Quantum Key Distribution*, Physical Review Letters, **119**, pp. 200501–5 (2017).

[26] C. J. Ballance, T. P. Harty, N. M. Linke, M. A. Sepiol, and D. M. Lucas, *High-Fidelity Quantum Logic Gates Using Trapped-Ion Hyperfine Qubits*, Physical Review Letters, **117**, pp. 060504–6 (2016).

[27] I. A. Walmsley and J. Nunn, *Editorial: Building Quantum Networks*, Physical Review Applied, **6**, p. 040001 (2016).

[28] R. Nigmatullin, C. J. Ballance, N. d. Beaudrap, and S. C. Benjamin, *Minimally complex ion traps as modules for quantum communication and computing*, New Journal of Physics, **18**, pp. 103028–21 (2016).

[29] P. Kumar, *Quantum frequency conversion*, Optics Letters, **15**, p. 1476 (1990).

[30] T. Li, *Structures, parameters, and transmission properties of optical fibers*, Proceedings of the IEEE, **68**, pp. 1175–1180.

[31] J. A. Buck, *Fundamentals of Optical Fibers*, Wiley Series in Pure and Applied Optics, Wiley (2004).

[32] J. Huang and P. Kumar, *Observation of quantum frequency conversion*, Physical Review Letters, **68**, pp. 2153–2156 (1992).

[33] M. A. Albota and F. N. C. Wong, *Efficient single-photon counting at 1.55 μm by means of frequency upconversion*, Optics Letters, **29**, pp. 1449–1451 (2004).

[34] A. P. Vandevender and P. G. Kwiat, *High efficiency single photon detection via frequency up-conversion*, Journal of Modern Optics, **51**, pp. 1433–1445 (2004).

[35] S. Tanzilli, W. Tittel, M. Halder, O. Alibart, P. Baldi, N. Gisin, and H. Zbinden, *A photonic quantum information interface*, Nature, **437**, pp. 116 EP —-120 (2005).

[36] M. T. Rakher, L. Ma, O. Slattery, X. Tang, and K. Srinivasan, *Quantum transduction of telecommunications-band single photons from a quantum dot by frequency upconversion*, Nature Photonics, **4**, pp. 786 EP —-791 (2010).

[37] H. Takesue, *Single-photon frequency down-conversion experiment*, Physical Review A, **82**, p. 013833 (2010).

[38] A. Samblowski, C. E. Vollmer, C. Baune, J. Fiurášek, and R. Schnabel, *Weak-signal conversion from 1550 to 532 nm with 84% efficiency*, Optics Letters, **39**, pp. 2979–2981 (2014).

[39] C. Langrock, E. Diamanti, R. V. Roussev, Y. Yamamoto, M. M. Fejer, and H. Takesue, *Highly efficient single-photon detection at communication wavelengths by use of upconversion in reverse-proton-exchanged periodically poled $LiNbO_3$ waveguides*, Optics Letters, **30**, pp. 1725–1727 (2005).

[40] Q. Li, M. Davanco, and K. Srinivasan, *Efficient and low-noise single-photon-level frequency conversion interfaces using silicon nanophotonics*, Nature Photonics, **10**, pp. 406–414 (2016).

[41] X. Guo, C.-L. Zou, H. Jung, and H. X. Tang, *On-Chip Strong Coupling and Efficient Frequency Conversion between Telecom and Visible Optical Modes*, Physical Review Letters, **117**, p. 123902 (2016).

[42] H. J. McGuinness, M. G. Raymer, C. J. McKinstrie, and S. Radic, *Quantum Frequency Translation of Single-Photon States in a Photonic Crystal Fiber*, Physical Review Letters, **105**, p. 093604 (2010).

[43] A. S. Clark, B. J. Eggleton, C. Xiong, M. J. Collins, and S. Shahnia, *High-efficiency frequency conversion in the single-photon regime*, Optics Letters, **38**, pp. 947–949 (2013).

[44] A. G. Radnaev, Y. O. Dudin, R. Zhao, H. H. Jen, S. D. Jenkins, A. Kuzmich, and T. A. B. Kennedy, *A quantum memory with telecom-wavelength conversion*, Nature Physics, **6**, pp. 894–899 (2010).

[45] P. J. Bustard, D. G. England, K. Heshami, C. Kupchak, and B. J. Sussman, *Quantum frequency conversion with ultra-broadband tuning in a Raman memory*, Physical Review A, **95**, p. 053816 (2017).

[46] C. E. Vollmer, C. Baune, A. Samblowski, T. Eberle, V. Händchen, J. Fiurášek, and R. Schnabel, *Quantum Up-Conversion of Squeezed Vacuum States from 1550 to 532 nm*, Physical Review Letters, **112**, p. 073602 (2014).

[47] D. Kong, Z. Li, S. Wang, X. Wang, and Y. Li, *Quantum frequency down-conversion of bright amplitude-squeezed states*, Optics Express, **22**, pp. 24192–10 (2014).

[48] R. Ikuta, Y. Kusaka, T. Kitano, H. Kato, T. Yamamoto, M. Koashi, and N. Imoto, *Wide-band quantum interface for visible-to-telecommunication wavelength conversion*, Nature Communications, **2**, p. 537 (2011).

[49] A. P. Vandevender and P. G. Kwiat, *Quantum transduction via frequency upconversion (Invited)*, Journal of the Optical Society of America B, **24**, pp. 295–299 (2007).

[50] T. Honjo, H. Takesue, H. Kamada, Y. Nishida, O. Tadanaga, M. Asobe, and K. Inoue, *Long-distance distribution of time-bin entangled photon pairs over 100 km using frequency up-conversion detectors*, Optics Express, **15**, pp. 13957–13964 (2007).

[51] M. T. Rakher, L. Ma, M. Davanco, O. Slattery, X. Tang, and K. Srinivasan, *Simultaneous Wavelength Translation and Amplitude Modulation of Single Photons from a Quantum Dot*, Physical Review Letters, **107**, p. 083602 (2011).

[52] N. Maring, K. Kutluer, J. Cohen, M. Cristiani, M. Mazzera, P. M. Ledingham, and H. d. Riedmatten, *Storage of up-converted telecom photons in a doped crystal*, New Journal of Physics, **16**, pp. 113021–16 (2014).

[53] C. Baune, J. Gniesmer, S. Kocsis, C. E. Vollmer, P. Zell, J. Fiurášek, and R. Schnabel, *Unconditional entanglement interface for quantum networks*, Physical Review A, **93**, p. 010302 (2016).

[54] M. Allgaier, V. Ansari, L. Sansoni, C. Eigner, V. Quiring, R. Ricken, G. Harder, B. Brecht, and C. Silberhorn, *Highly efficient frequency conversion with bandwidth compression of quantum light*, Nature Communications, **8** (2017).

[55] S. Zaske, A. Lenhard, C. A. Kessler, J. Kettler, C. Hepp, C. Arend, R. Albrecht, W.-M. Schulz, M. Jetter, P. Michler, and C. Becher, *Visible-to-Telecom Quantum Frequency Conversion of Light from a Single Quantum Emitter*, Physical Review Letters, **109**, pp. 147405–5 (2012).

[56] K. De Greve, L. Yu, P. L. McMahon, J. S. Pelc, C. M. Natarajan, N. Y. Kim, E. Abe, S. Maier, C. Schneider, M. Kamp, S. Höfling, R. H. Hadfield, A. Forchel, M. M. Fejer, and Y. Yamamoto, *Quantum-dot spin–photon entanglement via frequency downconversion to telecom wavelength*, Nature, **491**, pp. 421 EP —-425 (2012).

[57] J. S. Pelc, L. Yu, K. De Greve, P. L. McMahon, C. M. Natarajan, V. Esfandyarpour, S. Maier, C. Schneider, M. Kamp, S. Höfling, R. H. Hadfield, A. Forchel, Y. Yamamoto, and M. M. Fejer, *Downconversion quantum interface for a single quantum dot spin and 1550-nm single-photon channel*, Optics Express, **20**, pp. 27510–27519 (2012).

[58] B. Albrecht, P. Farrera, X. Fernandez-Gonzalvo, M. Cristiani, and H. de Riedmatten, *A waveguide frequency converter connecting rubidium-based quantum memories to the telecom C-band*, Nature Communications, **5**, p. 3376 (2014).

[59] P. Farrera, N. Maring, B. Albrecht, G. Heinze, and H. de Riedmatten, *Nonclassical correlations between a C-band telecom photon and a stored spin-wave*, Optica, **3**, pp. 1019–1024 (2016).

[60] V. Krutyanskiy, M. Meraner, J. Schupp, and B. P. Lanyon, *Polarisation-preserving photon frequency conversion from a trapped-ion-compatible wavelength to the telecom C-band*, Applied Physics B, **123** (2017).

[61] M. Bock, P. Eich, S. Kucera, M. Kreis, A. Lenhard, C. Becher, and J. Eschner, *High-fidelity entanglement between a trapped ion and a telecom photon via quantum frequency conversion*, Nature Communications, pp. 1–7 (2018).

[62] T. Walker, K. Miyanishi, R. Ikuta, H. Takahashi, S. V. Kashanian, Y. Tsujimoto, K. Hayasaka, T. Yamamoto, N. Imoto, and M. Keller, *Long-Distance Single Photon Transmission from a Trapped Ion via Quantum Frequency Conversion*, Physical Review Letters, **120**, p. 203601 (2018).

[63] A. Dréau, A. Tchebotareva, A. El Mahdaoui, C. Bonato, and R. Hanson, *Quantum Frequency Conversion of Single Photons from a Nitrogen-Vacancy Center in Diamond to Telecommunication Wavelengths*, Physical Review Applied, **9**, p. 064031 (2018).

[64] N. Maring, P. Farrera, K. Kutluer, M. Mazzera, G. Heinze, and H. de Riedmatten, *Photonic quantum state transfer between a cold atomic gas and a crystal*, Nature, **551**, pp. 485–488 (2017).

[65] R. Clark, T. Kim, and J. Kim, *Double-stage frequency down-conversion system for distribution of ion-photon entanglement over long distances*, in *2011 IEEE Photonics Society Summer Topical Meeting Series*, pp. 45–46, IEEE (2011).

[66] D. B. Oh, *Diode-laser-based sum-frequency generation of tunable wavelength-modulated UV light for OH radical detection*, Optics Letters, **20**, pp. 100–102 (1995).

[67] S. Wang, V. Pasiskevicius, F. Laurell, and H. Karlsson, *Ultraviolet generation by first-order frequency doubling in periodically poled $KTiOPO_4$*, Optics Letters, **23**, pp. 1883–1885 (1998).

[68] H. Rütz, K.-H. Luo, H. Suche, and C. Silberhorn, *Towards a quantum interface between telecommunication and UV wavelengths: design and classical performance*, Applied Physics B, **122**, p. 13 (2016).

[69] H. Rütz, K.-H. Luo, H. Suche, and C. Silberhorn, *Quantum Frequency Conversion between Infrared and Ultraviolet*, Physical Review Applied, **7**, p. 024021 (2017).

[70] Y. O. Dudin, A. G. Radnaev, R. Zhao, J. Z. Blumoff, T. A. B. Kennedy, and A. Kuzmich, *Entanglement of Light-Shift Compensated Atomic Spin Waves with Telecom Light*, Physical Review Letters, **105**, pp. 260502–4 (2010).

[71] Y.-C. Chen, P. S. Salter, S. Knauer, L. Weng, A. C. Frangeskou, C. J. Stephen, S. N. Ishmael, P. R. Dolan, S. Johnson, B. L. Green, G. W. Morley, M. E. Newton, J. G. Rarity, M. J. Booth, and J. M. Smith, *Laser writing of coherent colour centres in diamond*, Nature Photonics, **11**, pp. 77 EP —-80 (2017).

[72] J. L. Allen, R. Kosut, J. Joo, P. Leek, and E. Ginossar, *Optimal control of two qubits via a single cavity drive in circuit quantum electrodynamics*, Physical Review A, **95**, p. 042325 (2017).

[73] V. M. Schäfer, C. J. Ballance, K. Thirumalai, L. J. Stephenson, T. G. Ballance, A. M. Steane, and D. M. Lucas, *Fast quantum logic gates with trapped-ion qubits*, Nature, **555**, pp. 75–78 (2018).

[74] L. J. Stephenson, D. P. Nadlinger, B. C. Nichol, S. An, P. Drmota, T. G. Ballance, K. Thirumalai, J. F. Goodwin, D. M. Lucas, and C. J. Ballance, *High-rate, high-fidelity entanglement of qubits across an elementary quantum network*, arXiv.org (2019).

[75] P. L. Mennea, W. R. Clements, D. H. Smith, J. C. Gates, B. J. Metcalf, R. H. S. Bannerman, R. Burgwal, J. J. Renema, W. S. Kolthammer, I. A. Walmsley, and P. G. R. Smith, *Modular linear optical circuits*, Optica, **5**, pp. 1087–4 (2018).

[76] M. J. Weisen, M. T. Posner, J. C. Gates, C. B. E. Gawith, P. G. R. Smith, and P. Horak, *Low-loss wavelength-selective integrated waveguide coupler based on tilted Bragg gratings*, Journal of the Optical Society of America B, **36**, pp. 1783–9 (2019).

[77] T. A. Wright, R. J. A. Francis-Jones, C. B. E. Gawith, J. N. Becker, P. M. Ledingham, P. G. R. Smith, J. Nunn, P. J. Mosley, B. Brecht, and I. A. Walmsley, *Two-Way Photonic Interface for Linking the Sr^+ Transition at 422 nm to the Telecommunication C Band*, Physical Review Applied, **10**, p. 044012 (2018).

[78] R. W. Boyd, *Nonlinear Optics, Third Edition*, Academic Press, 3rd edition (2008).

[79] J. A. Armstrong, N. Bloembergen, J. Ducuing, and P. S. Pershan, *Interactions between Light Waves in a Nonlinear Dielectric*, Physical Review, **127**, p. 1918 (1962).

[80] F. Kienle, D. Lin, S.-u. Alam, H. S. S. Hung, C. B. E. Gawith, H. E. Major, D. J. Richardson, and D. P. Shepherd, *Green-pumped, picosecond MgO:PPLN optical parametric oscillator*, Journal of the Optical Society of America B, **29**, pp. 144–152 (2012).

[81] A. M. Brańczyk, A. Fedrizzi, A. G. White, T. M. Stace, and T. C. Ralph, *Engineered optical nonlinearity for quantum light sources*, Optics Express, **19**, pp. 55–65 (2011).

[82] O. A. Louchev, N. E. Yu, S. Kurimura, and K. Kitamura, *Thermal inhibition of high-power second-harmonic generation in periodically poled $LiNbO_3$ and $LiTaO_3$ crystals*, Applied Physics Letters, **87** (2005).

[83] M. Gündoğan, P. M. Ledingham, K. Kutluer, M. Mazzera, and H. de Riedmatten, *Solid State Spin-Wave Quantum Memory for Time-Bin Qubits*, Physical Review Letters, **114**, p. 230501 (2015).

[84] P. S. Kuo, J. S. Pelc, C. Langrock, and M. M. Fejer, *Using temperature to reduce noise in quantum frequency conversion*, Optics Letters, **43**, pp. 2034–2037 (2018).

[85] J. S. Pelc, L. Ma, C. R. Phillips, Q. Zhang, C. Langrock, O. Slattery, X. Tang, and M. M. Fejer, *Long-wavelength-pumped upconversion single-photon detector at 1550 nm: performance and noise analysis*, Optics Express, **19**, pp. 21445–21456 (2011).

[86] P. C. Strassmann, A. Martin, N. Gisin, and M. Afzelius, *Spectral noise in frequency conversion from the visible to the telecommunication C-band*, Optics Express, **27**, pp. 14298–14307 (2019).

[87] G. Agrawal, *Nonlinear fiber optics*, Academic Press, London, England, 6th edition (2019).

[88] Y. Deng, Q. Lin, F. Lu, G. P. Agrawal, and W. H. Knox, *Broadly tunable femtosecond parametric oscillator using a photonic crystal fiber*, Optics Letters, **30**, pp. 1234–1236 (2005).

[89] P. J. Mosley, S. A. Bateman, L. Lavoute, and W. J. Wadsworth, *Low-noise, high-brightness, tunable source of picosecond pulsed light in the near-infrared and visible*, Optics Express, **19**, pp. 25337–25345 (2011).

[90] S. Lefrancois, D. Fu, G. R. Holtom, L. Kong, W. J. Wadsworth, P. Schneider, R. Herda, A. Zach, X. S. Xie, and F. W. Wise, *Fiber four-wave mixing source for coherent anti-Stokes Raman scattering microscopy*, Optics Letters, **37**, pp. 1652–1654 (2012).

[91] M. Fiorentino, P. L. Voss, J. E. Sharping, and P. Kumar, *All-fiber photon-pair source for quantum communications*, IEEE Photonics Technology Letters, **14**, pp. 983–985.

[92] J. Fulconis, J. G. Rarity, O. Alibart, P. S. J. Russell, and W. J. Wadsworth, *High brightness single mode source of correlated photon pairs using a photonic crystal fiber*, Optics Express, **13**, pp. 7572–7582 (2005).

[93] R. J. A. Francis-Jones, R. A. Hoggarth, and P. J. Mosley, *All-fiber multiplexed source of high-purity single photons*, Optica, **3**, pp. 1270–1273 (2016).

[94] R. Paiella and K. J. Vahala, *Four-wave mixing and generation of terahertz radiation in an alternating-strain coupled quantum-well structure*, IEEE Journal of Quantum Electronics, **32**, pp. 721–728 (1996).

[95] D. Hollenbeck and C. D. Cantrell, *Multiple-vibrational-mode model for fiber-optic Raman gain spectrum and response function*, Journal of the Optical Society of America B, **19**, pp. 2886–2892 (2002).

[96] Q. Lin, F. Yaman, and G. P. Agrawal, *Photon-pair generation in optical fibers through four-wave mixing: Role of Raman scattering and pump polarization*, Physical Review A, **75**, p. 023803 (2007).

[97] C. J. McKinstrie, J. D. Harvey, M. G. Raymer, and S. Radic, *Translation of quantum states by four-wave mixing in fibers*, Optics Express, **13**, pp. 9131–9142 (2005).

[98] C. J. McKinstrie, S. Radic, and A. R. Chraplyvy, *Parametric amplifiers driven by two pump waves*, IEEE Journal of Selected Topics in Quantum Electronics, **8**, pp. 538–547 (2002).

[99] K. Saitoh and M. Koshiba, *Empirical relations for simple design of photonic crystal fibers*, Optics Express, **13**, pp. 267–274 (2005).

[100] T. A. Birks, J. C. Knight, and P. S. J. Russell, *Endlessly single-mode photonic crystal fiber*, Optics Letters, **22**, pp. 961–963 (1997).

[101] K. Garay-Palmett, H. J. McGuinness, O. Cohen, J. S. Lundeen, R. Rangel-Rojo, A. B. U'Ren, M. G. Raymer, C. J. McKinstrie, S. Radic, and I. A. Walmsley, *Photon pair-state preparation with tailored spectral properties by spontaneous four-wave mixing in photonic-crystal fiber*, Optics Express, **15**, pp. 14870–14886 (2007).

[102] K. Garay-Palmett, A. B. U'Ren, R. Rangel-Rojo, R. Evans, and S. Camacho-López, *Ultrabroadband photon pair preparation by spontaneous four-wave mixing in a dispersion-engineered optical fiber*, Physical Review A, **78**, pp. 146–13 (2008).

[103] M. G. Raymer, S. J. van Enk, C. J. McKinstrie, and H. J. McGuinness, *Interference of two photons of different color*, Optics Communications, **283**, pp. 747–752 (2010).

[104] H. J. McGuinness, M. G. Raymer, and C. J. McKinstrie, *Theory of quantum frequency translation of light in optical fiber: application to interference of two photons of different color*, Optics Express, **19**, pp. 17876–17907 (2011).

[105] R. A. Fisher and W. Bischel, *The role of linear dispersion in plane-wave self-phase modulation*, Applied Physics Letters, **23**, pp. 661–663 (1973).

[106] J. A. Fleck, J. R. Morris, and M. D. Feit, *Time-dependent propagation of high energy laser beams through the atmosphere*, Applied Physics, **10**, pp. 129–160.

[107] J. C. J. C. Butcher, *Numerical methods for ordinary differential equations*, J. Wiley, Chichester, West Sussex, England ; Hoboken, NJ (2003).

[108] M. L. Boas, *Mathematical methods in the physical sciences*, Wiley, Hoboken, N.J., 3rd ed. edition (2006).

[109] J. Hult, *A Fourth-Order Runge–Kutta in the Interaction Picture Method for Simulating Supercontinuum Generation in Optical Fibers*, Journal of Lightwave Technology, **25**, pp. 3770–3775 (2007).

[110] N. A. Mortensen, *Effective area of photonic crystal fibers*, Optics Express, **10**, pp. 341–348 (2002).

[111] E. J. Allen, G. Ferranti, K. R. Rusimova, R. J. A. Francis-Jones, M. Azini, D. H. Mahler, T. C. Ralph, P. J. Mosley, and J. C. F. Matthews, *Passive, Broadband, and Low-Frequency Suppression of Laser Amplitude Noise to the Shot-Noise Limit Using a Hollow-Core Fiber*, Physical Review Applied, **12**, p. 044073 (2019).

[112] O. R. Gibson and P. J. Mosley, *Optimising photon-pair generation with hybrid optical fibre*, in *Frontiers in Optics + Laser Science APS/DLS*, p. LTu1D.2, Optical Society of America (2019).